Author: Elmalk, Abdalmohsen

Title: Exposing biomolecular properties one molecule at a time

Date: 2012-12-13

Exposing biomolecular properties one molecule at a time

Proefschrift

ter verkrijging van
de graad van Doctor aan de Universiteit Leiden,
op gezag van Rector Magnificus prof.mr. P. F. van der Heijden,
volgens besluit van het College voor Promoties
te verdedigen op donderdag 13 december 2012
klokke 10.00 uur

door

Abdalmohsen Elmalk

geboren te El Damazin, Sudan
in 1972

Promotiecommisie:

Promotores:	Prof. Dr. T.J. Aartsma	Universiteit Leiden
	Prof. Dr. G.W. Canters	Universiteit Leiden
Overige Leden:	Prof. Dr. E.R. Eliel	Universiteit Leiden
	Prof. Dr. V. Subramaniam	Universiteit Twente
	Prof. Dr. M.A.G.J. Orrit	Universiteit Leiden
	Prof. Dr. T. Schmidt	Universiteit Leiden

Dit onderzoek is mede gefinancierd door de Stichting Steunfonds Soedanese Studenten.

ISBN/EAN: 978-90-8593-140-9
Casimir PhD Series, Delft-Leiden, 2012-34

Printed by: Uitgeverij BOXPress (Proefschriftmaken.nl)

This thesis is dedicated to the memory of Marten Durieux, whose spirit touched all who knew him.

Table of Contents

Chapter 4 65

Chapter 5 91

List of abbreviations

AFM	atomic force microscopy
APC	allophycocyanin
APD	avalanche photodiode
APTS	aminopropyltrimethoxysilane
AuNP	gold nanoparticle
Az	azurin
Az-AuNPs	azurin-gold nanoparticle constructs
bNiR	blue nitrite reductase
CCD	charge-coupled device
Chl	chlorophyll
CuNiR	copper-containing nitrite reductase
FCV	fluorescence-detected cyclovoltammetry
FLIM	fluorescence lifetime imaging microscopy
FRET	Förster resonance energy transfer
GA	glutaraldehyde
GFP	green fluorescent protein
gNiR	green nitrite reductase
IRF	instrument response function
MPTS	mercaptopropyl trimethoxysilane
NiR	nitrite reductase
NP	Nanoparticle
NPQ	non-photochemical quenching
OCP	orange carotenoid protein
PBS	phycobiliproteins
PBsomes	phycobilisomes
PC	phycocyanins
PE	phycoerythrins
PVA	polyvinyl alcohol
RCs	reaction centers
SAM	self-assembled monolayer
SCM	scanning confocal microscopy
SMD	Single molecule detection
SPR	surface plasmon resonance
T3R	Time-Tagged Time-Resolved
TCSPC	Time-Correlated Single-Photon Counting
TES	triethoxysilane
WFM	wide-field microscopy

Chapter 1:

Introduction

1.1 Single molecule detection

In recent years, advances in optical spectroscopy and microscopy have made it possible not only to detect and identify single, freely diffusing or immobilized fluorescent molecules, but also to realize spectroscopic measurements and monitor dynamic molecular processes(1–10). These advances in single-molecule detection at room temperature offer new tools for the study of individual macromolecules and biomolecules in complex condensed matter environments. The investigation of individual molecules one at a time can provide information on the distribution of molecular properties at nanoscale(11–14).

Single molecule detection (SMD) allows real-time observations without the ensemble and time averaging that is present in ensemble methods. In particular, the power of single-molecule measurements lies in the ability to resolve and analyze the properties of sub-populations. Moreover, SMD allows the study of asynchronous or nonsynchronizable reactions, the discovery of short-lived (nanosecond to millisecond lifetimes) transient intermediates, and the observation of process kinetics in full time trajectories. The information content of single molecule fluorescence data can be further increased by monitoring different fluorescence characteristics (e.g. fluorescence intensity, lifetime, emission spectrum). Such measurements allow the probing of reaction kinetics, redox properties, fluorescence enhancement and fluorescence resonant energy transfer for individual macromolecules and biomolecules. Of course, the price to pay for this is that one has to repeat the experiment on large numbers of single molecules to get a statistically significant distribution of results. An exciting aspect of SMD lies in its novelty, which makes it highly likely that many new physical and chemical phenomena are yet to be discovered using this technique.

Few biomolecules, however, are intrinsically fluorescent. To observe them by fluorescence imaging techniques they have to be suitably labeled with fluorescent tags. These labels can either consist of organic dye molecules(15–19), or of natively fluorescent proteins like the green fluorescent protein (GFP) and variants thereof(20–23). A variety of techniques has been developed to achieve specific labeling of the proteins of interest, and to incorporate them in living cells. Constructs using a natively fluorescent protein-tag can be genetically engineered and expressed in live cells.

The development of these single-molecule techniques has opened up new vistas for the study of the functional properties of biological systems. On one hand, it is focused on isolated biomolecules *in vitro*, such as proteins, enzymes, DNA or RNA. On the other hand there is increasing interest in applying these advanced imaging techniques to observe these and other biomolecules in action in their native environment, *i.e.*, the living cell(3,6,8,22–24).

In this thesis we have applied single-molecule techniques to study the photophysics of selected biomolecular systems. The experiments range from a spectroscopic study of a single, supramolecular photosynthetic pigment-protein complex to the detection of enzymatic turn-over of individual redox proteins. The latter case involved the development of novel techniques to monitor redox activity of metalloproteins by means of fluorescence. A brief introduction to the background of this work is given in section 1.4.

1.2 Single molecule fluorescence microscopy

Single molecule fluorescence detection offers high specificity and outstanding sensitivity. Because of its sensitivity, fluorescence microscopy has developed into one of the prime methods for single-molecule measurements and fundamental, biomolecular studies(6,7,19,20,25). This development is in large part due to improvements of optical detection schemes based on semiconductor technology which is characterized by a high quantum yield of photon detection (up to 80-90%), an essential prerequisite for observing emission from single molecules(26). On one hand there are the charge-coupled diode-array devices (CCDs)(26–28) in which this ultimate level of sensitivity is achieved through suppression of read-out noise and by cooling the detector to reduce thermal shot-noise. They consist of two-dimensional diode arrays that are particularly suitable for full-image acquisition in real time. On the other hand, avalanche photodiodes (APDs)(26,27,29–31) have acquired single-photon detectivity by taking advantage of the gain that is associated with the electron-multiplier effect of the near-avalanche mode of operation of a photodiode under reverse bias. An APD is typically a single-point detector, although recently this method of gain by electron multiplication has also been implemented in diode array detectors(32–34).

By incorporating these detectors in suitably designed optical microscopes (Fig. 1A) it becomes possible to spatially resolve and visualize individual, fluorescent molecules. The preferred design of the microscope for single-molecule imaging is the epi-fluorescent mode of operation in which the sample is excited with an appropriate laser source, and the back-scattered fluorescence is detected along the same optical path as the excitation light. Fluorescence, being red-shifted with respect to the absorption spectrum, is separated from the excitation light by a dichroic filter. The spatial resolution is determined by the diffraction-limit, i.e. the numerical aperture (NA) of the objective, and is roughly equal to half the wavelength of fluorescence if NA = 1(35).

The two different types of detectors, CCDs and APDs, lead to distinctly different types of epi-fluorescence microscopy. A CCD detector allows the real-time visualization of a wide field of view, the size of which is limited by the magnification factor and other geometric parameters of the imaging optics. Such a detector basically operates as an ultra-sensitive camera. An APD, on the other hand, is the detector of choice for a confocal epi-fluorescent microscope. Here the laser-excited fluorescence that is emitted by the sample in the focus of the objective is refocused onto a pin hole which acts as a spatial filter, after which it is directed to the APD. An image can be reconstructed by monitoring the fluorescence while either scanning the laser focus across the sample using, e.g., a set of movable mirrors, or by spatial translation of the sample using a scanning stage. For the work described in this thesis we have used a wide-field imaging as well as a sample-scanning confocal configuration(35). Both modes of operation were incorporated in one setup, with a sliding mirror assembly to switch from one to the other (figure 1A).

Wide-field excitation combined with epi-fluorescent image detection with a high-sensitive CCD camera has the advantage that large numbers of molecules can be monitored at the same time. The other advantage is the speed of imaging which allows, e.g., the tracking of molecules in space with a time resolution as short as a few milliseconds. It is to be noted that out-of-focus fluorescence from the sample contributes a diffuse background to the image which may reduce the contrast. In the experiments described in Chapter 2 we combined wide-field microscopy (WFM) with wavelength dispersion of the fluorescence to study spectroscopic features of individual pigment-protein complexes. This method is described in more detail in the next section.

In contrast to WFM, scanning confocal microscopy (SCM)(35) offers a small detection volume because the pin hole in the detection path only transmits the fluorescence that originates from the laser focus. The size of the pin hole is usually matched to the size of the Airy-disk that is formed by the refocused fluorescence. In that case the transmission of the pin hole and the spatial resolution are optimal. Because the pin hole acts as a spatial filter, a SCM can often provide a much better signal-to-noise ratio than a WFM. A very distinct feature of a SCM is that it can generate a three-dimensional image due to spatially selective fluorescence detection in the lateral as well as the longitudinal direction with respect to the optical axis of the microscope. Because of the intensity profile of the laser excitation beam in the focal region and the confocal optical geometry, the spatial resolution in the lateral scanning directions is higher than in the longitudinal direction(35).

In the work described in this thesis we use the SCM to analyse the photophysical properties of single, fluorescently labeled biomolecules which are immobilized on a chemically modified surface of glass or gold. The purpose of chemical surface modification is to achieve stable adsorption or covalent bonding of the biomolecule to the surface. The experiment typically involves the acquisition of a confocal image after which the coordinates of each fluorescent molecule in the image can be identified and marked. These molecules are successively targeted by the laser beam to measure the parameters of interest of each molecule, such as the fluorescence spectrum, the fluorescence lifetime, the fluorescence anisotropy and/or the fluorescence time trace (i.e. the photon arrival statistics). The time-resolved experiments require the use of pulsed lasers, but these are readily available with a choice of operating wavelengths to match the absorption spectra of common dye labels and fluorescent proteins. They facilitate the monitoring of temporal processes down to the level of tens of picoseconds. More sophisticated and complex strategies of single-molecule spectroscopy involve multi-color experiments, using more than one excitation laser and/or multiple dye-labels(36,37).

Fluorescence lifetime parameters provide the basis for a quantitative assessment of molecular properties and dynamics. Typical examples are the probing of the local environmental parameters of a fluorophore via lifetime changes, sensing distances on the nanometer scale by Förster resonance energy transfer (FRET), and monitoring functional properties of proteins and enzymes(2).

In the next section we will describe briefly the technical details of the setup that was developed to perform the experiments described in this thesis. It is designed to detect individual fluorescent photons and record their temporal and spectral signature.

1.3 Experimental setup

For the work described in this thesis we have constructed an experimental setup which combined both the wide-field and confocal imaging techniques, see Figure 1A. It incorporates a picosecond red laser (PicoQuant GmbH, LDH-P-639 with PDL 800-B driver) to deliver a continuous train of light pulses at 639 nm for excitation of the sample, with a repetition rate of 40 MHz, and a pulse duration of 90 to 400 ps depending on the setting of the output power. Alternatively, a frequency-doubled, diode-pumped Nd:YAG laser can be used for CW excitation at 532 nm. A polarization-maintaining single-mode fiber guides the laser light to the microscope, with the benefit of a well-defined beam profile from the output end of the fiber. The dichroic mirror (Z 532/633 M, Omega Optical) reflects the light into a high aperture oil immersion objective (Zeiss 100× oil, NA 1.4) which focuses the beam to a diffraction-limited spot (~300 nm diameter) on the sample surface.

In the confocal mode of operation the sample fluorescence is collected through the same objective, transmitted by the dichroic mirror and then filtered by a band pass filter (Omega Optical, D 675/50 M). The fluorescence light is focused by the microscope tube lens into a

50 µm pinhole. An achromatic lens with a focal length of +45 mm refocuses the light onto the active area (175 µm diameter) of a single-photon avalanche diode (APD, Perkin-Elmer SPCM-AQR-14). The data acquisition was done by the TimeHarp 200 TCSPC PC-board working in the special Time-Tagged Time-Resolved Mode, which stores precise timing information of every detected photon for further data analysis. Samples were mounted onto

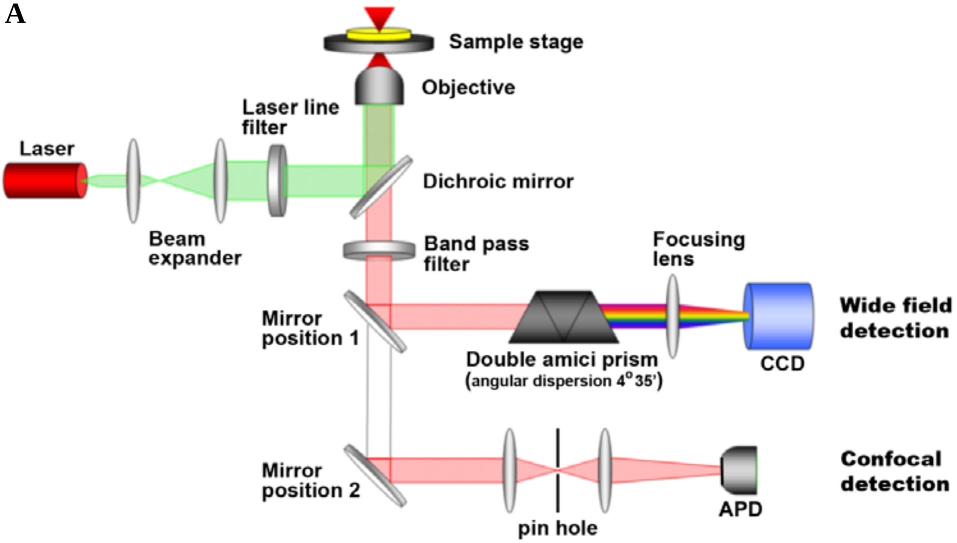

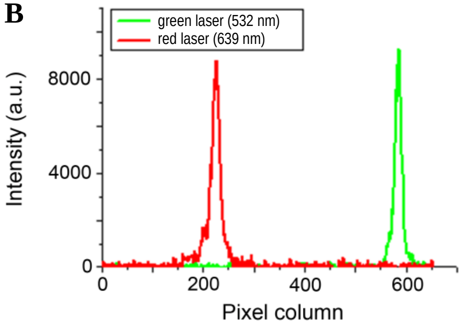

Figure 1: The optical setup, based on an Axiovert S100TV inverted microscope, combines a confocal and a wide-field fluorescence microscope. A solid state laser excites fluorescent species of interests. In the confocal detection path, a pinhole rejects the out of focus photons and the fluorescence signal is detected by the avalance photodiode (APD). A band pass filter suppresses scattered laser light and selectively transmits the fluorescence. By inserting a mirror in position 1 the setup operates in the wide-field detection mode. In the wide-field path, emitted light is collimated and chromatically dispersed by a double Amici-prism and focused onto a CCD camera. The insert on the right (B) shows the normalized spectral intensity distribution of a green (532 nm) and a red laser (639 nm), emanating from the same optical fiber, dispersed by the double Amici-prism on the CCD detector in wide-field mode. The dispersion is about 0.3 nm /pixel, and the spectral resolution is 1.5 nm.

a P-517 nanopositioner which was equipped with the E710 controller, both from Physik Instrumente GmbH (Germany). Scanning, accurate sample positioning, data collection and analysis were performed by the SymPhoTime software package (PicoQuant GmbH).

The set up can be switched to a wide-field detection scheme by inserting a mirror in the detection path to deflect the (collimated) fluorescence light towards the CCD camera (Cascade 650, Photometrics Inc.). This mode of operation, for example, can be used to locate individual molecules and record their position as a function of time in order to determine diffusion parameters. The experiments described in Chapter 2 of this thesis were designed to determine fluorescence spectra from individual pigment-protein complexes. For this purpose we inserted a double Amici prism (CVI Melles Griot, Inc.) in the optical detection path to spectrally disperse the fluorescence across the CCD array. A schematic diagram of the prism-based wide-field setup is shown in Figure 1 together with the confocal setup.

As mentioned above, a solid state laser (532 nm) or red diode laser (639 nm) was used for the excitation of the sample. An extra lens (not shown) is inserted in the excitation path to achieve wide-field illumination. The fluorescence emission from the sample is collected by the objective and separated from backscattered excitation light with a dichroic mirror (Z532/633M, Omega Optical). An achromatic lens (f = 50 mm) collimates the emission light, which then passes an Amici-prism (PRF-16.4-30-C, CVI Melles Griot, GmbH) dispersing the fluorescence light. Behind the prism, an achromatic focusing lens (f = 45 mm) brings the dispersed fluorescence light into focus for detection with the CCD camera (Cascade 650, Photometrics Inc.).

The system was calibrated by imaging the two laser lines at 532 and 639 nm (Figure 1B), and was found to have an average dispersion of 0.3 nm/pixel and a spectral resolution of about 1.5 nm. The dispersion as a function of wavelength is non-linear, but the wavelength range of interest is in our case (Chapter 2) small enough to assume that the dispersion is more or less constant.

1.4 Scope of this thesis

The work described in this thesis was aimed at the study of the functional properties of (isolated and purified) biomolecular systems at the single-molecule level. Two prerequisites are essential for successfully achieving this goal. First of all, single biomolecules should be observable, which means that they should be natively fluorescent or they should be rendered fluorescent by suitable biochemical or biomolecular engineering. The other challenge is to engineer the system in such a way that the fluorescence intensity reports the actual, functional state of the biomolecule.

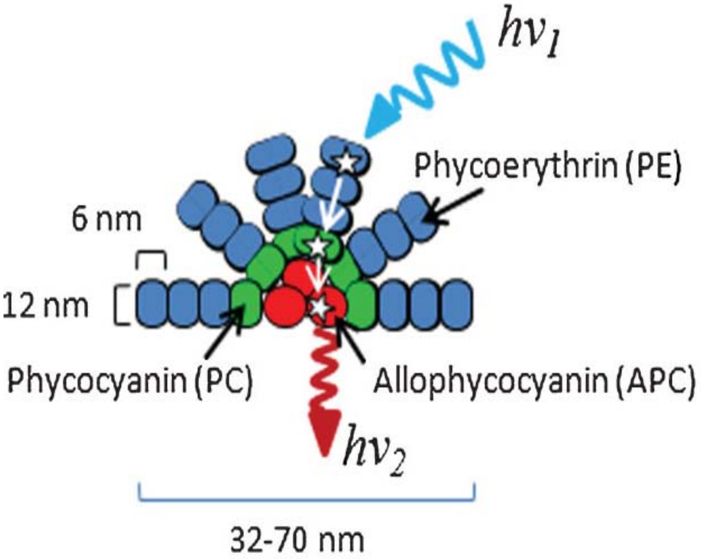

Figure 2: Schematic representation of the three main phycobiliprotein groups in the phycobilisome, the light-harvesting antenna complex in cyanobacteria and red algae(38–41). The phycobilisome docks to the membrane-embedded photosynthetic reaction center of the microorganism. The phycobiliproteins, which serve as scaffolding for covalently bound, linear tetrapyrrole chromophores are classified into three types based on their absorption spectra: phycoerythrin (PE), phycocyanin (PC), and allophycocyanin (APC). Hemispherically organized rods of PC and/or PE biliproteins join a core of APC biliproteins. The bulk of the absorption takes place in the rods, while the unique nanostructure facilitates efficient energy transfer towards the core, and from there to the photosynthetic reaction centers.

Phycobiliproteins have strong emission bands that extend well into the red region of the visible spectrum where there is minimal interference from biological materials (e.g. blood, sera and cell culture components). Because of these properties, phycobiliproteins have become promising fluorescent probes for use as a fluorescent marker in immunoassay, flow cytometry, and fluorescence microscopy.

1.4.1 Phycobilisomes

Intrinsic fluorescence of amino acid residues like tyrosin and tryptophan in common proteins is not sufficiently bright for achieving single-molecule sensitivity. Other chromophores with sufficiently high fluorescence quantum yields must be present, like in the fluorescing co-factors in GFP and other natively fluorescent proteins. In chapter 2 of this thesis we describe the study of individual phycobilisomes, brightly fluorescent supramolecular pigment-protein complexes, which have a light-harvesting role in photosynthetic organisms(38–41). The chromophores in these complexes consist of various types of phycobilins. Here we use the fluorescence spectrum, rather than just the intensity, to assess energy transfer and dissipation processes in this system as a function of illumination conditions. Real-time spectral detection at the single-complex level allows us to characterize the dynamic fluorescence behavior of individual phycobilisomes (PBsomes) in response to intense light,

In this work we explored a novel approach to monitor single-molecule fluorescence spectra using a double Amici prism as a dispersion element. It provides the possibility for investigating real-time fluorescent emission dynamics of PBsomes as well as the energy transfer between various PBsome components. It is revealed that green-light-induced photobleaching of a single PBsome consists of an energetic decoupling of phycobilin co-factors within the PBsome rod, serving as a novel pathway of energy dissipation. The results provide insights into the photo-protective roles of PBsomes in red algae in response to excess light energy and the energetic association of pigment-protein complexes.

1.4.2 The FluRedox principle

In the subsequent chapters we focus on the redox activity of metalloproteins, where we take advantage of a new method, the FluRedox principle(42–49), to not only visualize these proteins, but at the same time monitor their redox state in real time at the single-molecule level. Redox reactions drive a plethora of biological and chemical processes ranging from photosynthesis and respiration to industrial catalysis and the operation of fuel cells. The FluRedox methodology opens an entirely new platform for a more detailed study of the dynamics and mechanisms of redox protein activity because of its unsurpassed sensitivity and specificity. The work in this thesis is aimed at the implementation of this novel fluorescence method for single-molecule observation of redox events.

The FluRedox technique makes use of a feature that is characteristic of nearly all redox enzymes and electron transfer proteins, *i.e.*, they possess a redox-active centre with optical characteristics that change markedly when the redox state of the centre changes, that is when the redox center exercises its natural role. The emission intensity of a covalently attached fluorescent label will reflect these absorption changes provided the emission spectrum overlaps with the fluctuating absorption band. The physical mechanism responsible for this phenomenon is known as Förster resonant energy transfer (FRET) and the efficiency depends on the sixth power of the distance between prosthetic group and label. The only condition for the mechanism to work, therefore, is that the distance between label and prosthetic groups is properly chosen. The change in absorbance modulates the FRET efficiency, hence also the fluorescence intensity of the dye label. Note that usually the redox centers are non-fluorescent, thus FRET then results in quenching of fluorescence.

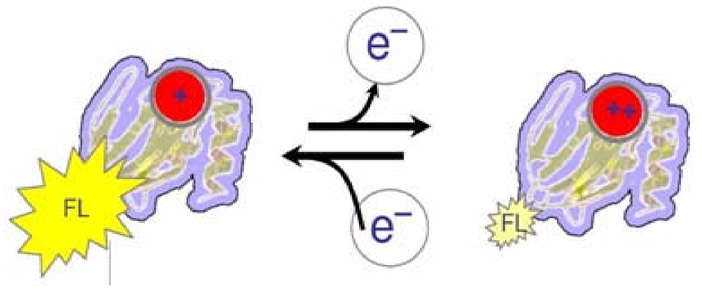

Figure 3: FluRedox principle(42–49)**.** The redox protein is linked to a fluorescent dye (FL) which can be excited at a specified wavelength. Subsequently, fluorescence can be measured using a photodiode. The redox state of the protein changes when the active center exchanges electrons either with an electrode or with a reactant in solution. Thus, the change can be translated into the fluorescent intensity of the label covalently attached to the protein surface on the basis of FRET.

Redox proteins and enzymes that contain a so-called Type-1 Cu-atom in their active center are ideal targets for application of the FluRedox technique, as was demonstrated in references (42–49). These blue (Type-1) copper sites are characterised by a strong absorption band at 600 nm when the copper is in the oxidized state(50). This band is absent when the Cu-center is reduced. In this thesis we applied the FluRedox method to azurin and nitrite reductase, both containing a Type-1 Cu center(51). The proteins were labeled with suitable dyes, like Atto-647N or Atto-655, either at the N-terminus or at the –SH group of specifically engineered, surface-exposed cysteins. Turn-over of the redox center of a single molecule through electron exchange with reactants in solution is then observed in real time as step-wise changes of the fluorescence intensity and the fluorescence life time.

1.4.3 Fluorescently labeled azurin on a gold surface

Previous work(46) has shown that optical tracking of electrochemical events by fluorescence-detected cyclovoltammetry (FCV) already made it possible to determine the electrochemical parameters and redox activity of ensembles of as few as 100 protein molecules. For the combination of fluorescent redox state detection and electronic control the protein together with its fluorescent label needs to be placed close to an electrode, usually a metal surface. This raises questions about the fluorophore-metal interaction, a subject that has raised considerable interest in recent years from a fundamental as well as an application-oriented perspective. The effect of a metal surface on a nearby fluorophore can lead to both enhancement and quenching of the fluorescence(52–57). Which of these effects dominates is strongly dependent on distance between fluorophore and metal surface. In the work described in this thesis we have elucidated in more detail how the dye-label, when attached to a redox protein, is affected by the interaction with a nearby gold surface. This is important information to further develop the FluRedox method for sensitive electrochemical detection, and to improve our understanding of the recently developed FCV methodology.

We have studied (Chapter 3) the fluorescence of labeled azurin immobilized either on coated glass or on gold films (bare, or coated with a self-assembling monolayer (SAM)) as a function of the thickness of the gold film and the thickness of the SAM. Intensity and lifetime measurements allowed for the separation of enhancement and quenching effects on the fluorescence. In addition, the effect of the redox state on the fluorescence of the labeled protein was investigated. Fluorescence quenching, competing with enhancement, is shown to be a short range effect, and is absent when the SAM is more than 10 carbon atoms high. Significant enhancement is observed with increased roughness of the gold layer.

In chapter 4 we focus on the interaction of fluorescently labeled Az with a gold nanoparticle (AuNP). Fluorescence enhancement by NPs and their application in biotechnology is a relatively new subject. A gold NP can function as an optical antenna and through near-field interactions enhance the excitation and fluorescence rate of attached fluorophores. On the other hand, the fluorescence may be *quenched* by energy transfer from the excited fluorophore to the conduction electrons in the NP. Depending on which term is dominant the fluorescence may be enhanced or diminished(58–63). It confronted us with the question how the FluRedox effect would be influenced by a nearby gold NP, and if it could even be enhanced.

To answer this question we have investigated the emission of the fluorescently labeled 14 kDa large copper protein azurin (Az) from *Pseudomonas aeruginosa* immobilized on gold nanoparticles (NPs) as a function of the NP size (1.4-80 nm). Two forms of the Az were studied by single-molecule fluorescence detection: the native form and a form wherein the Cu had been replaced by Zn (ZnAz). Experiments on ZnAz showed that the excitation and radiative rates of the fluorophore were enhanced upon immobilization on AuNPs, but quenching by energy transfer to the NP was observed as well. The results were analyzed quantitatively in terms of a theoretical model which takes into account the influence of the Au NP on the fluorophore excitation rate and quantum yield. Whereas ZnAz is colourless, the native (Cu containing) Az is colourless only in the reduced (Cu^+) form. It is shown that attachment of the fluorescently labeled CuAz to a AuNP may lead to a tenfold enhancement of the sensitivity for detecting a redox change of the protein based on the FluRedox principle.

The results illustrate how the redox states of a single protein molecule can be investigated by fluorescence lifetime analysis both for Az on gold and for Az on glass. Thus, the combination of fluorescence lifetime imaging with our FRET-based redox detection method provides a new approach for studying the kinetics of biological electron transfer at the single molecule level. Furthermore, the ability to tune the emission properties of labeled redox proteins immobilized on metal surfaces opens a way to design improved biosensing devices.

Figure 4: A schematic representation of Atto647N-labeled azurin adsorbed to AuNPs on a glass slide modified with APTS. The protein framework is depicted in green, the Cu atom in blue and the dye label in red.

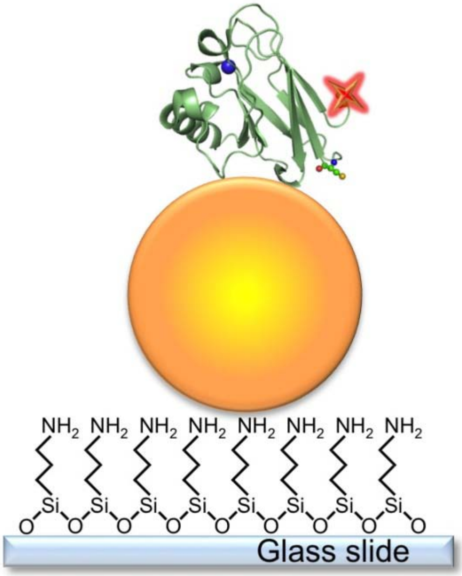

1.4.4 Nitrite reductase, one by one.

Single molecule measurements often reveal aspects of protein behavior that are hidden in ensemble measurements. However, applications in enzymology have been limited to enzymes with fluorescent cofactors, substrates or products. One of the main advantages of the FluRedox principle is that it is a platform technology, i.e., it can be applied to any enzyme as long as the prerequisites for FRET with the redox active center can be satisfied. This provides access to a large variety of interesting enzyme systems not only from a scientific point of view, but also for innovative (*e.g.*, biosensor) applications.

In Chapter 5 we successfully demonstrate the potential of the FluRedox principle by the results of single-molecule measurements of the enzymatic activity of nitrite reductase from *Alcaligenes xylosoxidans* (AxNiR). This enzyme converts nitrite into nitric oxide(64). It is a homotrimer, with a binuclear Cu center (T1 and T2). The T1-Cu accepts electrons from a donor and transfers them to the T2-Cu where nitrite is reduced. Oxidized T1-Cu has two broad absorption bands that disappear upon reduction. The FRET efficiency between a fluorescent label and the T1-Cu can be used to follow the catalytic cycle on the basis of fluorescence fluctuations.

For these studies our collaborators at the University of Newcastle (Prof. C. Dennison, D. Kostrz) prepared a mutant of AxNiR with an exposed cysteine (Cys) residue. As AxNiR is a trimer, the Cys in one monomer was used for dye labeling while the Cys in another monomer was used to anchor the enzyme via a molecular linker on a suitably functionalized surface of a microscope cover slip. Fluorescence time-traces of immobilized, single AxNiR in buffer and in the absence of substrates showed typically a steady signal of 2-5 photon counts/ms. The intensity of the signal dramatically increased to

Azurin is a Type 1 blue copper protein with a molecular mass of 14.6 kDa, where the redox-active copper center is either in the 1+ or the 2+ state. Its physiological function has been under debate. Initially it was thought that azurin fulfils a role as electron transporter in the nitrite/nitrate respiratory chain of the microorganism. More recently it was made plausible that the protein has a role in the oxidative stress response(65). A characteristic feature of the Type 1 Cu center is the strong ligand to a cystein, two imidazoles and two weaker axial ligands, in a distorted trigonal planar geometry.

Copper-containing nitrite reductase (CuNiR) also harbours a Type 1 Cu site bound by two histidines, one cysteine and one methionine(50). In addition, one so-called Type 2 (colourless) copper ion is bound by three histidines. There exists a fourth coordination site for the Cu II centre, which is occupied by water in the resting enzyme and by nitrite in the presence of a substrate. CuNiR enzymes are homotrimers and they can be further classified into blue and green species depending on the details of the ligand geometry of the type 1 Cu sites. They are one of the enzymes that operate in the nitrogen cycle, converting nitrite into nitric oxide.

Azurin and CuNiR are both optically characterized by their intense absorption band in the visible region around 600 nm (azurin) and 430-600 nm (NiR) when the Type 1 copper is oxidized. This band is absent in the reduced state. A state-change can be translated onto the fluorescence intensity of a dye label conjugated to the protein surface using the FluRedox method.

a steady fluorescence rate of 10-30 photon counts/ms by the addition of a reductant (ascorbate/PES), as expected from the reduction of the Type 1 Cu centers. Upon subsequent addition of nitrite the fluorescence time-traces were clearly different. The trace was dominated by a more or less less steady 2-5 counts/ms signal with sporadic bursts of 20-30 counts/ms. This behavior can be explained by the T1-Cu fluctuating between the oxidized and reduced state as the enzyme is turning over.

The FRET between dye label and the redox center process not only affects the fluorescence intensity, but also the fluorescence lifetime. This was used to advantage by studying the activity of AxNiR by single-molecule fluorescence lifetime imaging, providing high contrast between the oxidized and reduced form of the enzyme. Immobilized Atto-647N-labeled AxNiR has a lifetime of 3.7 ns in the reduced state, and of 1.1 ns in the oxidized state. By adding a suitable electron donor together with nitrite to the sample, it was possible to observe the catalytic cycling of a single enzyme between the oxidized and reduced forms. Unexpectedly, our studies showed that in turn-over conditions single AxNiR molecules can be sorted in two different populations that follow two different kinetic regimes. Two models have been proposed in the literature for NiR catalysis, a random and a sequential mechanism. Our experiments show that each individual enzyme follows just one of the two possible routes.

References

1. Schuler B (2007) Application of single molecule Förster resonance energy transfer to protein folding. *Methods in molecular biology* 350:115–38.
2. Joo C, Balci H, Ishitsuka Y, Buranachai C, and Ha T (2008) Advances in single-molecule fluorescence methods for molecular biology. *Annual review of biochemistry* 77:51–76.
3. Xie XS, Choi PJ, Li G-W, Lee NK, and Lia G (2008) Single-molecule approach to molecular biology in living bacterial cells. *Annual review of biophysics* 37:417–44.
4. Kapanidis AN and Strick T (2009) Biology, one molecule at a time. *Trends in biochemical sciences* 34:234–43.
5. Hohlbein J, Gryte K, Heilemann M, and Kapanidis AN (2010) Surfing on a new wave of single-molecule fluorescence methods. *Physical Biology* 7:031001.
6. Lord SJ, Lee HD, and Moerner WE (2010) Single-molecule spectroscopy and imaging of biomolecules in living cells. *Analytical chemistry* 82:2192–203.
7. Toomre D and Bewersdorf J (2010) A new wave of cellular imaging. *Annual review of cell and developmental biology* 26:285–314.

8. Yang H (2010) Progress in single-molecule spectroscopy in cells. *Current opinion in chemical biology* 14:3–9.
9. Fitzpatrick JAJ and Lillemeier BF (2011) Fluorescence correlation spectroscopy: linking molecular dynamics to biological function in vitro and in situ. *Current opinion in structural biology* 21:650–60.
10. Schäfer R and Schmidt PC, ed. (2012) *Methods in Physical Chemistry*. Weinheim, Germany: Wiley-VCH Verlag GmbH & Co. KGaA.
11. Barkai E, Jung Y, and Silbey R (2004) Theory of single-molecule spectroscopy: beyond the ensemble average. *Annual review of physical chemistry* 55:457–507.
12. Gopich IV and Szabo A (2006) Theory of the statistics of kinetic transitions with application to single-molecule enzyme catalysis. *The Journal of chemical physics* 124:154712.
13. Watkins LP and Yang H (2005) Detection of intensity change points in time-resolved single-molecule measurements. *The journal of physical chemistry. B* 109:617–28.
14. Yang H (2008) Model-Free Statistical Reduction of Single-Molecule Time Series. *… and Evaluation of Single-Molecule Signals edited by E …*:1–29.
15. Buschmann V, Weston KD, and Sauer M (2002) Spectroscopic study and evaluation of red-absorbing fluorescent dyes. *Bioconjugate chemistry* 14:195–204. American Chemical Society.
16. Resch-Genger U, Grabolle M, Cavaliere-Jaricot S, Nitschke R, and Nann T (2008) Quantum dots versus organic dyes as fluorescent labels. *Nature methods* 5:763–75. Nature Publishing Group.
17. Berezin MY and Achilefu S (2010) Fluorescence lifetime measurements and biological imaging. *Chemical reviews* 110:2641–84. American Chemical Society.
18. Gonçalves MST (2009) Fluorescent labeling of biomolecules with organic probes. *Chemical reviews* 109:190–212. American Chemical Society.
19. Bunt G (2011) Optical Fluorescence Microscopy. In *Optical Fluorescence Microscopy*, ed. A Diaspro, pp. 111–130. Berlin, Heidelberg: Springer Berlin Heidelberg.
20. Chudakov DM, Lukyanov S, and Lukyanov KA (2005) Fluorescent proteins as a toolkit for in vivo imaging. *Trends in biotechnology* 23:605–13.
21. Shaner NC, Steinbach PA, and Tsien RY (2005) A guide to choosing fluorescent proteins. *Nature methods* 2:905–9.
22. Müller-Taubenberger A and Anderson KI (2007) Recent advances using green and red fluorescent protein variants. *Applied microbiology and biotechnology* 77:1–12.
23. Chudakov DM, Matz MV, Lukyanov S, and Lukyanov KA (2010) Fluorescent proteins and their applications in imaging living cells and tissues. *Physiological reviews* 90:1103–63.
24. Patterson G, Davidson M, Manley S, and Lippincott-Schwartz J (2010) Superresolution imaging using single-molecule localization. *Annual review of physical chemistry* 61:345–67. Annual Reviews.
25. Wu B, Piatkevich KD, Lionnet T, Singer RH, and Verkhusha VV (2011) Modern fluorescent proteins and imaging technologies to study gene expression, nuclear localization, and dynamics. *Current opinion in cell biology* 23:310–7.

26. Michalet X, Siegmund OHW, Vallerga JV, Jelinsky P, Millaud JE, and Weiss S (2007) Detectors for single-molecule fluorescence imaging and spectroscopy. *Journal of modern optics* 54:239. Taylor & Francis.
27. Moerner WE and Fromm DP (2003) Methods of single-molecule fluorescence spectroscopy and microscopy. *Review of Scientific Instruments* 74:3597.
28. Rizzuto R, Carrington W, and Tuft RA (1998) Digital imaging microscopy of living cells. *Trends in cell biology* 8:288–92.
29. Cova S, Ghioni M, Lacaita A, Samori C, and Zappa F (1996) Avalanche photodiodes and quenching circuits for single-photon detection. *Applied Optics* 35:1956. OSA.
30. Zappa F (1996) Solid-state single-photon detectors. *Optical Engineering* 35:938.
31. Renker D and Lorenz E (2009) Advances in solid state photon detectors. *Journal of Instrumentation* 4:P04004–P04004.
32. Michalet X, Colyer RA, Scalia G, Kim T, Levi M, Aharoni D, Cheng A, et al. (2010) High-throughput single-molecule fluorescence spectroscopy using parallel detection. *Proceedings - Society of Photo-Optical Instrumentation Engineers* 7608:76082D–76082D–12.
33. Colyer RA, Scalia G, Villa FA, Guerrieri F, Tisa S, Zappa F, Cova S, Weiss S, and Michalet X (2011) Ultra high-throughput single molecule spectroscopy with a 1024 pixel SPAD. In *SPIE BiOS*, pp. 790503–790503–8.
34. Privitera S, Tudisco S, Lanzanò L, Musumeci F, Pluchino A, Scordino A, Campisi A, et al. (2008) Single Photon Avalanche Diodes: Towards the Large Bidimensional Arrays. *Sensors* 8:4636–4655. Molecular Diversity Preservation International.
35. Webb RH (1996) Confocal optical microscopy. *Reports on Progress in Physics* 59:427–471.
36. Cognet L, Harms GS, Blab GA, Lommerse PHM, and Schmidt T (2000) Simultaneous dual-color and dual-polarization imaging of single molecules. *Applied Physics Letters* 77:4052.
37. Kapanidis A and Laurence T (2005) Alternating-laser excitation of single molecules. *Accounts of chemical research* 38:523–533.
38. Glazer AN (1994) Phycobiliproteins — a family of valuable, widely used fluorophores. *Journal of Applied Phycology* 6:105–112.
39. MacColl R (1998) Cyanobacterial phycobilisomes. *Journal of structural biology* 124:311–34.
40. Ducret A, Sidler W, Wehrli E, Frank G, and Zuber H (1996) Isolation, Characterization and Electron Microscopy Analysis of A Hemidiscoidal Phycobilisome Type from the Cyanobacterium Anabaena sp. PCC 7120. *European Journal of Biochemistry* 236:1010–1024.
41. Adir N (2005) Elucidation of the molecular structures of components of the phycobilisome: reconstructing a giant. *Photosynthesis research* 85:15–32.
42. Schmauder R, Librizzi F, Canters GW, Schmidt T, and Aartsma TJ (2005) The oxidation state of a protein observed molecule-by-molecule. *ChemPhysChem* 6:1381–6.
43. Kuznetsova S, Zauner G, Schmauder R, Mayboroda O a, Deelder AM, Aartsma TJ, and Canters GW (2006) A Förster-resonance-energy transfer-based method for fluorescence detection of the protein redox state. *Analytical biochemistry* 350:52–60.

44. Zauner G, Lonardi E, Bubacco L, Aartsma TJ, Canters GW, and Tepper AWJW (2007) Tryptophan-to-dye fluorescence energy transfer applied to oxygen sensing by using type-3 copper proteins. *Chemistry Eur J* 13:7085–90.

45. Davis JJ, Burgess H, Zauner G, Kuznetsova S, Salverda J, Aartsma T, and Canters GW (2006) Monitoring interfacial bioelectrochemistry using a FRET switch. *The journal of physical chemistry. B* 110:20649–54.

46. Salverda JM, Patil AV, Mizzon G, Kuznetsova S, Zauner G, Akkilic N, Canters GW, Davis JJ, Heering HA, and Aartsma TJ (2010) Fluorescent Cyclic Voltammetry of Immobilized Azurin: Direct Observation of Thermodynamic and Kinetic Heterogeneity. *Angewandte Chemie (Intern. Ed.)* 122:5912–5915.

47. Goldsmith RH, Tabares LC, Kostrz D, Dennison C, Aartsma TJ, Canters GW, and Moerner WE (2011) Redox cycling and kinetic analysis of single molecules of solution-phase nitrite reductase. *Proceedings of the National Academy of Sciences of the United States of America* 108:17269–74.

48. Kuznetsova S, Zauner G, Aartsma TJ, Engelkamp H, Hatzakis N, Rowan AE, Nolte RJM, Christianen PCM, and Canters GW (2008) The enzyme mechanism of nitrite reductase studied at single-molecule level. *Proceedings of the National Academy of Sciences of the United States of America* 105:3250–5.

49. Gustiananda M, Andreoni A, Tabares LC, Tepper AWJW, Fortunato L, Aartsma TJ, and Canters GW (2011) Sensitive detection of histamine using fluorescently labeled oxido-reductases. *Biosensors and Bioelectronics*: Elsevier B.V.

50. Adman ET (1991) Structure and function of copper-containing proteins. *Current Opinion in Structural Biology* 1:895–904.

51. Jeuken LJC, Vliet PV, Verbeet MP, Camba R, Mcevoy JP, Armstrong FA, and Canters GW (2000) Role of the Surface-Exposed and Copper-Coordinating Histidine in Blue Copper Proteins: The Electron-Transfer and Redox-Coupled Ligand Binding Properties of His117Gly Azurin. *Journal of the American Chemical Society* 122:12186–12194.

52. Prigogine I and Rice SA, ed. (1978) *Advances in Chemical Physics*. Hoboken, NJ, USA: John Wiley & Sons, Inc.

53. Drexhage KH (1970) Influence of a dielectric interface on fluorescence decay time. *Journal of Luminescence* 1-2:693–701.

54. Hellen EH and Axelrod D (1987) Fluorescence emission at dielectric and metal-film interfaces. *Journal of the Optical Society of America B* 4:337. OSA.

55. Fort E and Grésillon S (2008) Surface enhanced fluorescence. *Journal of Physics D: Applied Physics* 41:013001.

56. Lakowicz JR (2005) Radiative decay engineering 5: metal-enhanced fluorescence and plasmon emission. *Analytical biochemistry* 337:171–94.

57. Waldeck DH, Alivisatos AP, and Harris CB (1985) Nonradiative damping of molecular electronic excited states by metal surfaces. *Surface Science* 158:103–125.

58. Härtling T, Reichenbach P, and Eng LM (2007) Near-field coupling of a single fluorescent molecule and a spherical gold nanoparticle. *Optics Express* 15:12806. OSA.

59. Kühn S, Håkanson U, Rogobete L, and Sandoghdar V (2006) Enhancement of Single-Molecule Fluorescence Using a Gold Nanoparticle as an Optical Nanoantenna. *Physical Review Letters* 97:017402.

60. Bharadwaj P, Anger P, and Novotny L (2007) Nanoplasmonic enhancement of single-molecule fluorescence. *Nanotechnology* 18:044017.

61. Taminiau TH, Stefani FD, Segerink FB, and van Hulst NF (2008) Optical antennas direct single-molecule emission. *Nature Photonics* 2:234–237.

62. Lakowicz JR and Fu Y (2009) Modification of single molecule fluorescence near metallic nanostructures. *Laser & Photonics Review* 3:221–232.

63. Anger P, Bharadwaj P, and Novotny L (2006) Enhancement and Quenching of Single-Molecule Fluorescence. *Physical Review Letters* 96:113002.

64. Adman E and Murphy M (2001) Copper Nitrite Reductase. In *Encyclopedia of Inorganic and Bioinorganic Chemistry*, ed. RA Scott. Chichester, UK: John Wiley & Sons, Ltd.

65. Vijgenboom E, Busch JE, and Canters GW (1997) In vivo studies disprove an obligatory role of azurin in denitrification in Pseudomonas aeruginosa and show that azu expression is under control of rpoS and ANR. *Microbiology* 143:2853–63.

Chapter 2

Dynamic fluorescence photobleaching of single phycobilisome complexes from Porphyridium cruentum[*]

---

[*] Liu L-N, Elmalk AT, Aartsma TJ, Thomas J-C, Lamers GEM, Zhiu B-C, Zhang Y-Z (2008) Light-Induced Energetic Decoupling as a Mechanism for Phycobilisome-Related Energy Dissipation in Red Algae: A Single Molecule Study. PLoS ONE 3(9): e3134. doi:10.1371/journal.pone.0003134

Summary: *Single molecule spectroscopy is applied to phycobilisomes (PBsomes), the light-harvesting antenna complex in cyanobacteria and red algae. Real-time spectral detection at the single particle level allows us to characterize the dynamic fluorescence behavior of individual phycobilisome in response to intense light. It is revealed that intense green laser light may affect the function of phycoerythrin molecules in intact phycobilisome, thus restricting energy transfer to the PBsome core. In this way, excess energy will be dissipated before photodamage to the reaction center takes place. Our work further indicates that this process is dependent on oxygen. Singlet oxygen is assumed to function at the interaction site between phycoerythins and other phycobilisome components. As a consequence, a novel photoprotective mechanism occuring in phycoerythrin-containing phycobilisomes is proposed. The spectral variety of phycobiliproteins in intact phycobilisome results in not only broader absorption at the visible range, but also in a photoprotective response to excess absorbed energy.*

2.1 Introduction

Phycobilisomes (PBsomes, see Figure 1) are the major light-harvesting antennae complexes in cyanobacteria and red algae. They are capable of absorbing solar light and transfer energy to the chlorophylls (Chls) of photosynthetic reaction centers (RCs) with a high efficiency. PBsomes are supramolecular protein complexes made up of watersoluble phycobiliproteins (PBPs) and linker polypeptides [1–3]. PBPs are a distinctively colored group of disk-shaped macromolecular proteins bearing covalently attached open-chain tetrapyrroles, known as phycobilins, orderly assembled into PBsomes. In the absence of photosynthetic RCs, the PBsomes are highly fluorescent. Four spectral groups of PBPs are commonly identified: phycoerythrins (PEs), phycoerythrocyanins (PECs), phycocyanins (PCs) and allophycocyanins (APCs). Solar energy is absorbed by the chromophores of PEs (λ_{max} = 545-565 nm) and transferred in turn by nonradiative transfer via PCs (λ_{max} = 620 nm), APCs (λ_{max} = 650 nm) to the reaction center.

The conventional PBsomes in cyanobacteria have a hemidiscoidal shape, and contain six peripheral rods and a core complex. The peripheral rods are composed of PEs and inner PCs, and three parallel cylinders consisting of APCs form the core of the PBsome complex. Hemiellipsoidal PBsomes in the unicellular red alga *Porphyridium (P.) cruentum* also contain a large number of PE molecules at the peripheral rod endings [4,5]. In addition to R-phycocyanin (R-PC) and APC, two different spectral types of PEs were found in *P. cruentum*: B-phycoerythrin (B-PE) and b-phycoerythrin (b-PE) [6]. A specialized type of linker polypeptides, the chromophoric c subunits, are responsible for the association of B-PE molecules in the rod elements, whereas they are absent in b-PEs [3,7]. The evolution of

PBPs, presumably from APC to PC and to PE, is accompanied by the diversity and increasing number of chromophores [8]. The spectral diversity of different PBPs within PBsomes is assumed to extend the absorbance range (500–650 nm) of cyanobacteria and red algae, and offers a stepwise transfer of the trapped energy to the RCs. More specifically, the presence of PE in red algae, especially the γ-subunit-containing PE, could broaden the absorbance of red algae which allows increasing light-harvesting capacity.

The large number of chromophores in PBsomes ensures a high light-harvesting yield of photosynthesis. On the other hand, it may be lethal if excess light is absorbed by the PBsomes in relation to the capacity of photosynthetic RCs. In response to excess excitation

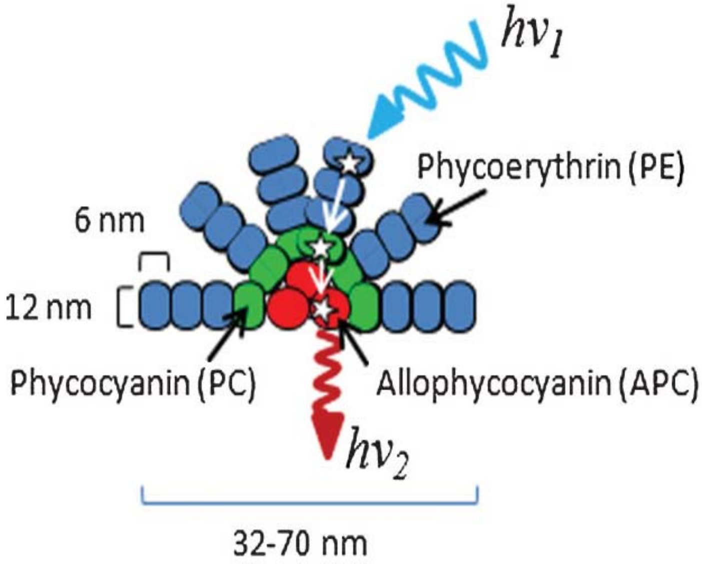

Figure 1: Schematic representation of the three main phycobiliprotein groups in the phycobilisome, the light-harvesting antenna complex in cyanobacteria and red algae. The phycobilisome docks to the membrane-embedded photosynthetic reaction center of the microorganism. The phycobiliproteins, which serve as scaffolding for covalently bound, linear tetrapyrrole chromophores are classified into three types based on their absorption spectra: phycoerythrin (PE), phycocyanin (PC), and allophycocyanin (APC). Hemispherically organized rods of PC and/or PE biliproteins join a core of APC biliproteins. The bulk of the absorption takes place in the rods, while the unique nanostructure facilitates efficient energy transfer towards the core, and from there to the photosynthetic reaction centers.
Phycobiliproteins have strong emission bands that extend well into the red region of the visible spectrum where there is minimal interference from biological materials (e.g. blood, sera and cell culture components). Because of these properties, phycobiliproteins have become promising fluorescent probes for use as a fluorescent marker in immunoassay, flow cytometry, and fluorescence microscopy.

energy, a soluble orange carotenoid protein (OCP) has been demonstrated to be involved in energy dissipation in cyanobacteria [9–11]. In contrast, the potential photoprotective response of PBsomes themselves with respect to excess energy is less understood.

The spectroscopy of single molecules or complexes has the great advantage to avoid the ensemble averaging encountered in bulk spectroscopy. Molecular dynamics, for instance molecular conformational changes, energy transfer and photobleaching, can be studied by measuring the real-time fluorescence spectrum at single molecule sensitivity [12]. Single-molecule techniques have been extensively applied in photosynthetic systems and provided new insights into the photophysical processes and functional properties of photosynthetic chromophore-protein complexes[13–18]. Effects of photobleaching and interprotein energy transfer of single PBPs have been previously reported, for systems such as B-PE[19], monomers of PEC[20,21] and APC trimers[22]. However, spectral properties of intact single PBsome complex are still enigmatic.

Recently a novel approach was explored to monitor single-molecule fluorescence spectra using an Amici prism as a dispersion element [23,24]. It provides the possibility to investigate real-time fluorescent emission dynamics of PBsomes as well as the energy transfer between various PBsome components. In the present work, we applied single-particle spectroscopy to investigate the PBsomes from *P. cruentum* at room temperature. Green-light-induced photobleaching of single PBsome was demonstrated to involve an energetic decoupling of B-PE within the PBsome rod, serving as a novel pathway of energy dispassion. Our results provide insights into the photobleaching dynamics of PBsomes in red algae, and their photoprotective roles in response to excess light energy.

2.2 Materials and Methods

2.2.1 Sample separation

Porphyridium (P.) cruentum wild-type and mutant F11 strain (UTEX 637) were grown in an artificial sea water medium [38]. Flasks were supplied with 3% CO_2 in air through a plug of sterile cotton at a constant temperature of 20 °C. Cultures were illuminated continuously with light provided by daylight fluorescent lamps at 6 $W.m^{-2}$. The *P. cruentum* F11 mutant was constructed before [29] and was shown by LiDS-PAGE [30] analyses to be deficient of the c subunit. Intact PBsomes were separated following previously described protocols[5].

2.2.2 Spectral analysis

Absorbance spectra were recorded with UV-160A spectrophotometer (Shimadzu, Japan). Room-temperature fluorescence spectra were measured with a LS 55 Luminescence

Spectrometer (Perkin-Elmer Instruments, USA). For single-particle experiments, PBsomes were dissolved in 0.75 M phosphate buffer with 1% polyvinyl alcohol (PVA) to a protein concentration of 0.5 µg/ml, after which samples were spin-coated on a freshly cleaned microscope cover-glass. For gluteraldehyde (GA) fixation, the dilution buffer contained not only PVA, but also GA with a final concentration of 1% (v/v).

2.2.3 Experimental Setup

The single-molecule fluorescence microscopy setup is based on an Axiovert S100TV inverted microscope with epifluorescent detection. The power density at the sample was 35–1050 W.cm^{-2}. The light from the laser sources, a Nd:YAG (532 nm) or a solid state laser (639 nm), was passed through a set of optical components (to control intensity and polarization), reflected by a dichroic mirror (transmission centered at 550 nm/660 nm), and focused on the sample by a high numerical aperture water-immersion objective (60×, numerical aperture 1.2, Olympus). By inserting an extra lens before the dichroic mirror, which focuses the laser beam at the backplane aperture of the microscope objective, the setup can be switched from a confocal to a wide-field imaging mode. Fluorescence emission from excited molecules was collected with the same objective, filtered after the dichroic mirror with an additional notch filter to reject the remaining scattered laser light and Raman scattered light. For spectral analysis, fluorescence emission was dispersed by an Amici prism and detected with a front-illuminated charge-coupled device (CCD) camera (Cascade 650, Photometrics). The integration time used for the spectral acquisition was 0.3 seconds.

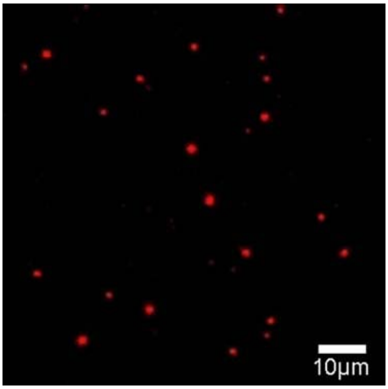

Figure 2. Fluorescence image (82x82 µm^2) of individual PBsomes at room temperature. Excitation wavelength is 532 nm.

2.3 Results

2.3.1 Fluorescence photobleaching of single PBsomes

Green (532 nm) and red (639 nm) lasers were utilized in this work for high-light illumination. Based on the ensemble absorption spectrum of PBsomes from *P. cruentum*, the 532 nm light is absorbed predominantly by PE, allowing us to investigate the full energy transfer chain within intact PBsomes, from PE to R-PC, then to APC and finally to the PBsome terminal emitters, LCM and αAPB [25]. Figure 2 shows the raw fluorescence image of individual PBsomes excited at 532 nm (260 W•cm^{-2}). The complexes were

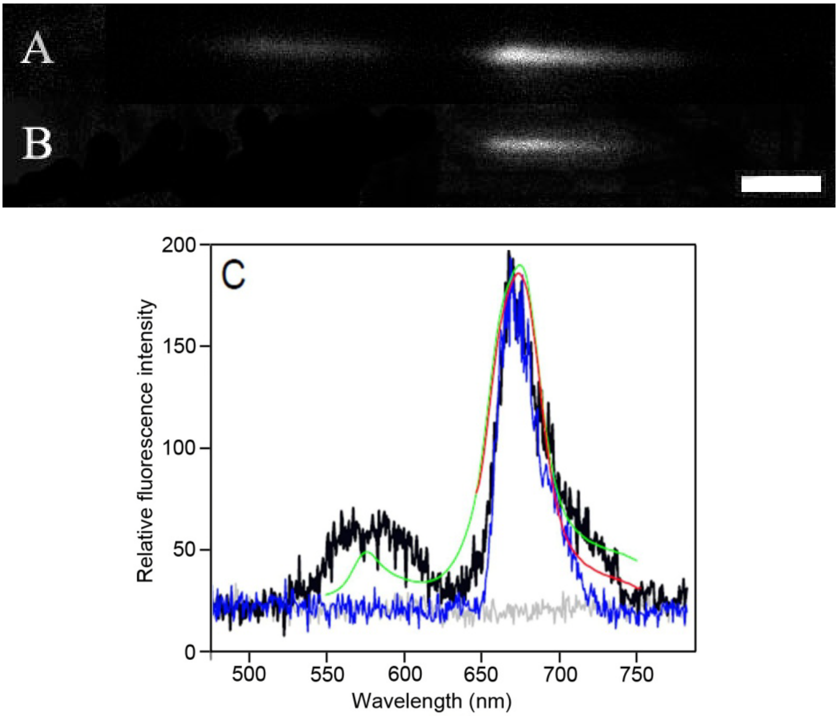

Figure 3. A,B: Fluorescence emission image of single PBsomes at room temperature. Images were obtained in wide-field microscopy combined with dispersion of the epifluorescence by an Amici prism in front of the CCD camera. Single PBsomes were imaged as two bands when excited at 532 nm (A), and a single fluorescence band was recorded when excited at 639 nm (B). C: fluorescence emission spectra of single PBsome excited at 532 nm (black) and 639 nm (blue). The background is shown with light gray. The two emission bands resemble the room-temperature fluorescence ensemble spectra of PBsome in bulk solution (0.75 M phosphate buffer, pH 7.0) when excited at 532 nm (green) and 639 nm (red), respectively.

immobilized on the glass slide by adding 1% (v/v) polyvinyl alcohol (PVA) to a diluted PBsome solution in 0.75 M phosphate buffer, pH 7.0. Due to the high dilution to 0.5 μg.ml^{-1}, most of the observed intensity spots represent single PBsomes. A good signal-to-noise ratio of the fluorescence emission was obtained due to the strong fluorescence of PBsome supramolecular complex which carries up to 2000 bilin chromophores, in combination with highly sensitive detection. After dispersion by an Amici prism, two discrete fluorescence bands were recorded simultaneously when a single PBsome was excited at 532 nm (Figure 3A). Full fluorescence emission spectrum of single PBsomes were obtained by integrating the total fluorescence intensities within a selected region on the CCD array and subtracting the background. Figure 3B shows the fluorescence image of a single PBsome when excited at 639 nm. As depicted in Figure 3C, a major fluorescence emission from the PBsome core (674 nm) and a minor fluorescence emission band of PE (576 nm) were observed. We recorded fluorescence spectra of 200 single PBsome complexes acquired with a 400 ms integration time per spectrum. 80% of them (162 single PBsomes) present typical fluorescence of PBsomes. Spectral variation was observed in the other 20% PBsomes, showing decreased fluorescence and a higher ratio of PE/PBsome core fluorescence. It is assumed that the photobleaching of a few PBsomes has taken place under laser illumination in the process of seeking targeting samples. Excitation energy at 639 nm is only absorbed by APC complexes. Therefore, the fluorescence emission of PBsome complex was detected as only a single fluorescence band attributed to the PBsome core (Figures 3B and 3C). These are consistent with the bulk fluorescence spectra (Figure 3C).

We further investigated the fluorescence photobleaching of individual PBsome complexes. As shown in Figure 4A, under illumination with 532 nm laser at 260 W•cm^{-2}, PBsome core fluorescence exhibited a successive decrease of the fluorescence intensity in combination with a minor blue-shift. This implies that intense green-light induces the photobleaching of the intact PBsome. Surprisingly, PE fluorescence did not present the same photobleaching behavior as the PBsome core fluorescence. Instead, an increase of PE fluorescence intensity at the first seconds of illumination was observed, followed by a decrease. This is clearly evident in the fluorescence intensity traces of two emission bands as a function of time (Figure 4B). It shows a 1.6-fold fluorescence increase of PE emission at the first stage of illumination and a decrease after 50 seconds.

These two distinct stages of PBsome are further revealed by examining the ratio of PE to PBsome core fluorescence. As seen in Figure 4B, the ratio of the fluorescence intensities of PE to PBsome core initially rises drastically above the value of 1.0, due to the combined effects of the increase of PE emission and the rapid decrease of PBsome core emission;

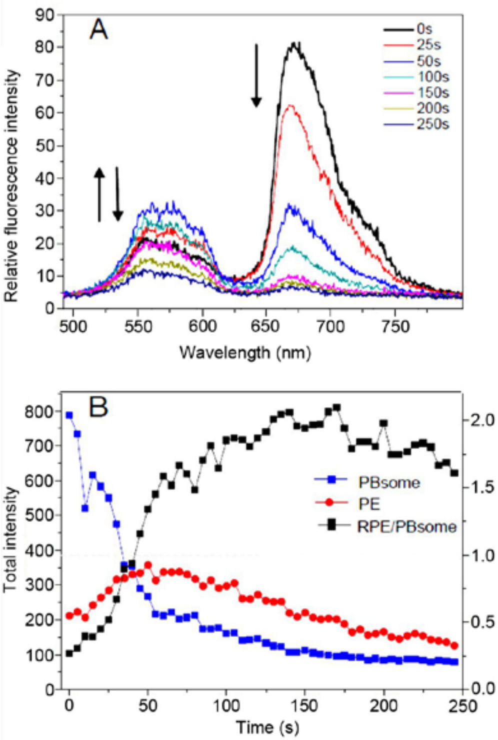

Figure 4. Fluorescence photobleaching of single PBsome under 532 nm illumination at 260 W•cm^{-2} during 250 seconds. Integration time is 400 ms. A: fluorescence spectral profiles of single PBsome during photobleaching. Arrows represent the fluorescence changes of PE and PBsome core. B fluorescence intensities of PE (red, 570 nm) and PBsome core (blue, 675 nm) of single PBsome as well as the ratio of fluorescence intensities of PE/PBsome core (black) as a function of time.

afterward it gradually decreases, indicating that at the late stage both emissions are bleached with relatively similar rates. The real-time spectral dispersion thus provides the opportunity to monitor the fluorescence dynamics of PBsome under specific illumination conditions, and to correlate the observations with changes of energy migration. We note that, due to the more complex pigment composition of the PBsomes from *P. cruentum*, the photobleaching profile of single PBsome in this case is different from those of individual PBPs observed before [19–22] .

2.3.2 Power-dependence of single PBsome fluorescence

To reveal the effect of illumination power on their fluorescence and photobleaching behavior, single PBSomes were illuminated with a green laser (532nm) at different power

Figure 5. Power-dependence of fluorescence photobleaching of single PBsomes.

A: normalized PBsome fluorescence intensity time courses over the laser power ranging from 35 to 1050 W•cm^{-2}. Excitation wavelength is 532 nm.

B: normalized PE (570 nm) fluorescence intensity time courses over the laser power range from 35 to 1050 W•cm^{-2}. Excitation wavelength is 532 nm.

C: normalized PBsome core (675 nm) fluorescence intensity time courses over the laser power range from 35 to 1050 W•cm^{-2}. Excitation wavelength is 639 nm which can only excite APC.

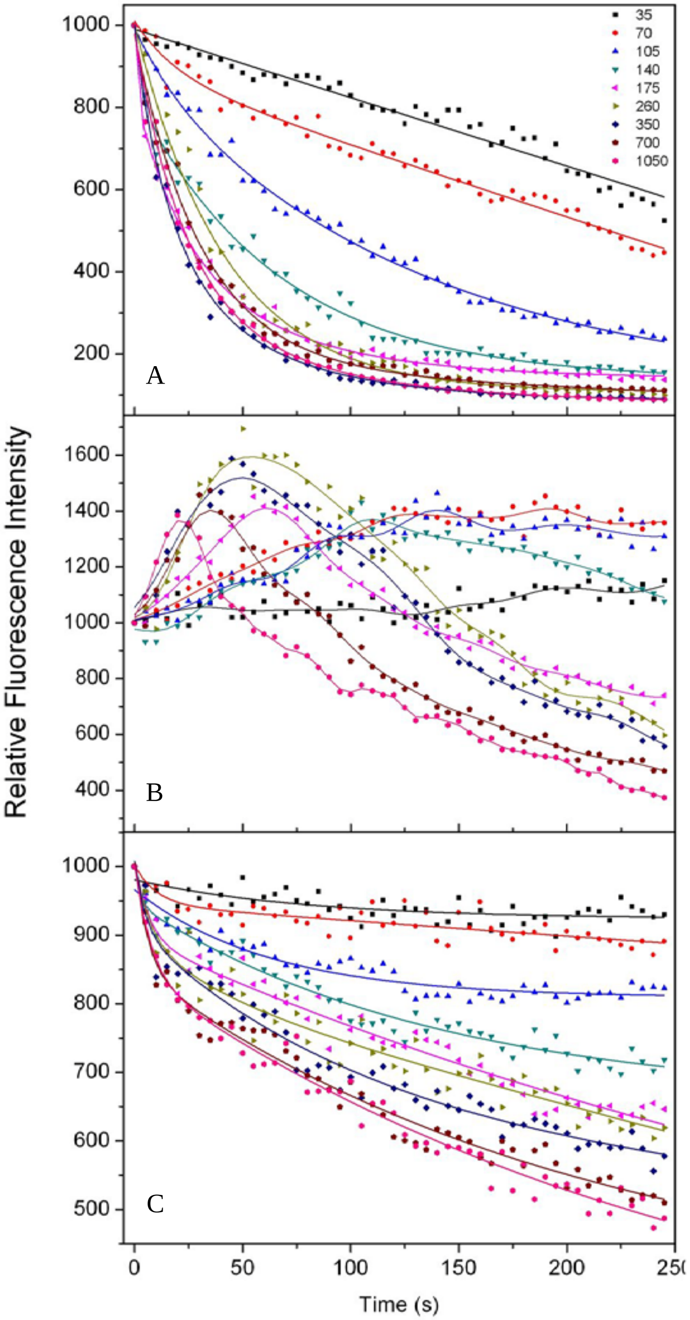

levels (35 to 1050 W•cm^{-2}). The light intensity in these experiments is up to a few orders of magnitude higher than under natural conditions. As shown in Figure 5A, the bleaching effect of the individual PBsomes is strongly depending on the laser power up to 140 W•cm^{-2}. Above 140 W•cm^{-2}, the photobleaching profiles appeared to be nearly indistinguishable and more than 80% photobleaching was obtained. Figure 5B presents the power dependence of PE emission with excitation at 532 nm. With the increase of laser power, a significant rise of PE emission intensity was observed. The maximum intensity was detected at 260 W•cm^{-2}. The PE intensity traces reflect competition between an increase of fluorescence intensity and photobleaching. Above 260 W•cm^{-2}, the photobleaching starts to dominate, limiting the maximal incline of fluorescence intensities. Furthermore, the maximum emission intensity presents a progressive blue-shift with the increase of laser power, indicating that more intense light can result in a faster increase of PE emission. Figure 5C shows the power dependence of PBsome core emission with excitation at 639 nm. Since only APCs can be excited at 639 nm, the power dependent behavior of PBsome core emission may be compared with the PBsome core fluorescence when excited at 532 nm, to provide more insights into energy transfer of intact PBsome.

It was found that the fluorescence of PBsome core complex is unable to be completely bleached (at most up to 50%) in 250 seconds. With absorbance of PBsomes at 532 nm being 6-fold higher than that at 639 nm (see absorption spectrum shown below in section 2.3.4), 1050 W•cm^{-2} red laser power is comparable to 175 W•cm^{-2} green laser power upon excitation the PBsome complex. 1050 W•cm^{-2} red laser induced 50% of photobleaching, whereas 175 W•cm^{-2} green laser resulted in as low as 80% of photobleaching, suggesting that the fluorescence loss of PBsome core when excited at 532 nm is composed not only of the photobleaching of PBsome core emission, but also of reduced PE-to-core energy transfer which contributes to the increase of PE emission.

2.3.3 Green laser induces an energetic decoupling of the PBsome

The possibilities for the fluorescence increase of PE are suggested. First, fast energy transfer from PE to the PBsome core allows the PE complexes to be less bleached than PBsome terminal emitters. When down-stream energy acceptors are bleached, excess energy captured by peripheral PE molecules is dissipated from the PE. Another possibility is the decoupling of PE from energy transfer path in the PBsome. Excess energy may increase the rate of bleaching of PE which exists as an isolated individual energy acceptor after the energetic decoupling, and result in further decrease of PE emission. In addition, it is also possible that energy transfer within the PBsomes is much decreased due to the photodamage without physical decoupling of the complex [26].

To further reveal the mechanism involved in the fluorescence increase of PE, we investigated single PBsome complex pre-treated with the protein cross-linking agent glutaraldehyde (GA). GA has been commonly used to stabilize PBsome conformations [5,27,28]. Under the treatment of GA (1%, v/v; 1 min incubation), the PBsome is assumed to remain conformationally and functionally intact. This is corroborated by the fact that bulk (Figure 6A) and single-molecule emission spectra (Figure 6B) before and after GA treatment are identical. Figure 7A shows time courses of the total intensity of PE emission in single PBsome untreated and pre-treated with GA. In contrast to the photobleaching behavior of untreated PBsome, no increase of PE emission was observed after fixation with GA, which indicates that the increase of PE emission observed in the photobleaching of untreated PBsome may be attributed to the energetic decoupling of PE in the PBsome.

In Figure 7B, the photobleaching percentage of PBsome core emission treated with GA is found to be 10% less than that of untreated PBsome. Such a difference is assumed to be attributed to the energetic decoupling of PE molecules. Figure 7C presents the distinct

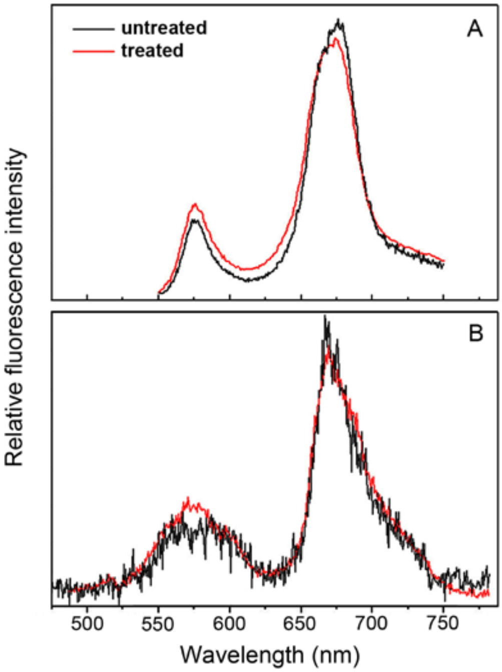

Figure 6. Comparison of the fluorescence properties of PBsomes treated and untreated with gluteraldehyde (GA, 1 min incubation). Excitation wavelength is 532 nm. A: ensemble fluorescence spectra; B: single-molecule fluorescence spectra.

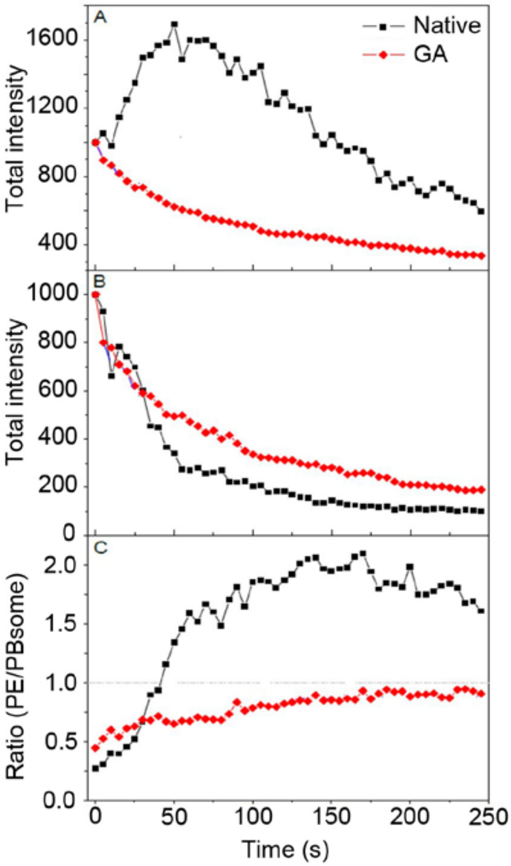

Figure 7. Fluorescence photobleaching of PBsome, native (black) and treated (red) with GA under illumination power of 260 W•cm^{-2}. A, time course of the photobleaching of PE emission after normalization; B, time course of the photobleaching of PBsome core emission after normalization; C, time course of the ratio of fluorescence intensities of PE/PBsome core.

ratios of PE to PBsome core fluorescence intensity in these two conditions. Untreated PBsome exhibited a drastic incline of the ratio up to the value of 2.0, which suggests that after bleaching PE fluorescence is more pronounced than that of the PBsome core. In contrast, the ratio of fluorescence intensity of the PBsome with GA treatment was observed to be less increased, constantly lower than the value of 1.0. Our data revealed that green-laser-induced energetic decoupling might involve changes of the protein-protein associations within the PBsome.

2.3.4 Fluorescence photobleaching of mutant PBsome

It is noteworthy that the light-induced decoupling of PE in single PBsome can only result in no more than 2 times of fluorescence increase and energy transfer within the complex can still take place. It apparently implies two discrete types of PEs: one group of PEs are involved in the light-induced decoupling, and another group still have a solid association in the PBsome rods to perform energy flow. This is reminiscent of previous observation that two types of PEs, B-PE and b-PE, were found in the rod of *P. cruentum* PBsomes [6]. The distinction between the two is the presence of a c peptide in B-PE but not in b-PE [7]. The mutant strain F11 of *P. cruentum* was characterized to contain a lower level of PE content in light of the complete deficiency of c subunits, the B-PE-associated chromophoric linker polypeptides, revealed by LiDS-PAGE (lithium dodecyl sulfate polyacrylamide gel electrophoresis) experiments [29,30]. Absorption spectra of ensemble PBsomes from wild-type (WT) and F11 *P. cruentum* show that one third of PE is retained in the mutant PBsome compared to WT PBsome (Figure 8A). It is most likely that the remaining are b-PE molecules which assemble with neighboring R-PC by linker polypeptides which are different from the c subunits. The smaller dimension of mutant PBsome because of a reduced PE content is also confirmed by our TEM results (data not shown).

As a comparative investigation, we examined the fluorescence emission properties of single PBsome prepared from mutant F11. In terms of the reduced absorbance at 532 nm in this mutant, a laser intensity of 700 $W \cdot cm^{-2}$ was applied on the F11 PBsome compared to 260 $W \cdot cm^{-2}$ on WT PBsome in order to obtain identical excitation conditions. Figure 8B shows a dispersed fluorescence emission of single PBsome from F11 excited at 532 nm green laser. Two separated fluorescence bands are detected, reminiscent of the fluorescence property of the WT PBsome. In addition to the identical emission positions, we found that the PE fluorescence of mutant PBsome is weaker than that of WT PBsome, which probably suggests a higher efficiency of energy transfer in mutant PBsome (Figure 8C). It may imply the flexible assembly between B-PE and b-PE in WT PBsomes, as well as the relatively solid interaction between b-PE and neighboring R-PC hexamer. During the process of photobleaching, both PE and PBsome core emissions of F11 PBsome are quenched in parallel (Figure 8D). The intensity ratios of b-PE to PBsome core fluorescence are relatively constant, lower than the value of 1.0. Unlike WT PBsomes, the increase of PE emission intensity during the bleaching was not seen, suggesting that B-PE molecules which are located at the peripheral side of WT PBsome rods are predominately responsible for the energetic decoupling of PBsome, whereas b-PE is probably not involved.

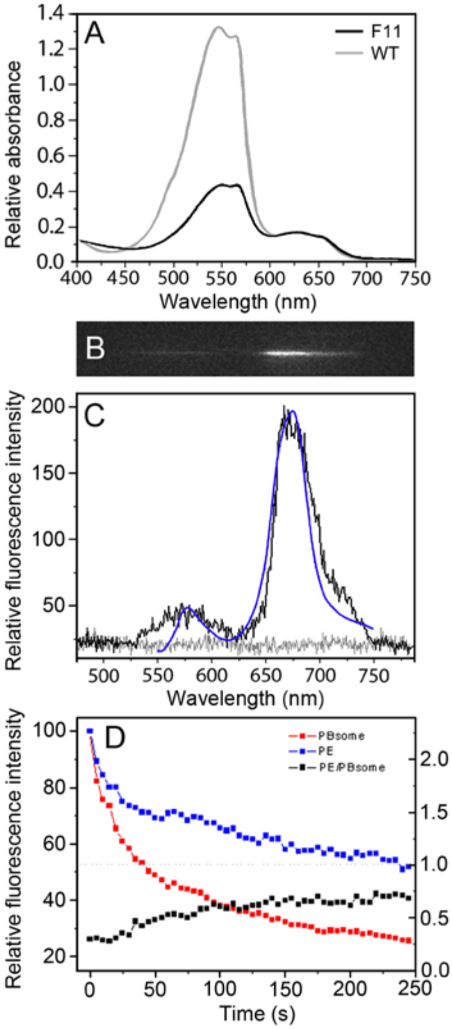

Figure 8. Single-molecule properties of PBsome from mutant *P. cruentum* F11. A, absorbance of ensemble PBsome from WT and mutant strain. A532 of F11 PBS is as low as 35% than WT PBsome, so laser power performed on F11 PBsome is 700 W·cm^{-2}. B, fluorescence emission image of single F11 PBsome at room temperature obtained in wide-field microscopy dispersed by the Amici prismin front of CCD camera. C, single PBsome was imaged as two fluorescence bands when excited at 532 nm (black). Background is presented with light gray. Room-temperature fluorescence emission spectra of isolated mutant PBsome (0.75 M phosphate buffer, pH 7.0) were recorded when excited at 532 nm (blue). D, total intensities of PE (■) and PBsome core (■) emission of single PBsome as well as their ratio (■) as a function of time.

2.4 Discussion and Conclusions

The strong fluorescence of the PBsomes, due to the abundance of chromophores carried in the PBsomes, is shown to be an advantage for the sensitive detection of individual complexes. We applied fluorescence detection at the single-molecule level to investigate, for the first time, the fluorescence of the PBsomes in *P. cruentum* dispersed through an Amici prism. The real-time fluorescence detection is able to reveal the spectral dynamics and energy transfer of the chromophore-protein complexes. The results allow us to better characterize the effects of intense light on the PBsomes. It is demonstrated that strong green-light can induce the photobleaching of the PBsomes, as shown by the drastic decline of PBsome core fluorescence. More importantly, a great proportion of excitation energy, surprisingly, is found to be dissipated in the form of PE fluorescence. Our comparative results, which show that such an increase is absent in the photobleaching of GA-treated PBsome, verified the green-light-induced energetic decoupling of PE in the PBsome. The PBsome rods in cyanobacteria comprise in general one or up to two types of PBPs, whereas those in red alga *P. cruentum* contain in turn B-PE that carries c-subunit, b-PE that does not carry a γ-subunit, and R-PC from the periphery to the interior of the rod. Therefore, the PBsomes of *P. cruentum* is an ideal model to study the energy transfer pathway. The different behaviors of PE fluorescence in WT and mutant experiments presented in this work strongly indicate the distinct contributions of B-PE and b-PE in the energy transfer of PBsomes.

On the basis of our observations, a schematic model of light induced energetic decoupling of PBsome was proposed, as depicted in Figure 9. It is characterized that B-PE and b-PE are coupled face-to-face at the periphery of PBsome rod. The outer B-PE presents potentially a flexible energetic association with the inner b-PE with the assistance of the c subunit of B-PE. The photobleaching of PBsome is accompanied by the energetic decoupling which preferentially occurs in the b-PE - B-PE interaction site. It is presumably that the c subunits, the specific linker polypeptides which carry phycobilins, might play an important role in the energetic decoupling of PBsomes in *P. cruentum*. On the other hand, assuming that the same process occurs also at the much lower physiological light intensities, our observations have important implications on the photoprotection function of PBsomes. So far, the mechanism of the antenna-related photoprotection of OCP in cyanobacteria has been elucidated [9–11]. The general concept is that PBsome can not dissipate excess absorbed energy without assistance [31–33]. Such an energetic decoupling of PBsomes with respect to intense light may presumably allow excess photon energy from PE to photosynthetic RCs to be modulated to minimize the risk of chlorophyll photooxidation. This is corroborated with the findings about high-light-induced reorganization [34] and photodegradation of PBsome [35]. The light-induced conformational altering of PBsome was also found in UV-treated PBsome from which a PE fluorescence increase has been observed, arising from the disassembly of PBsome components [36]. The photoprotection role of PE in the PBsomes of cyanobacteria on dissipating excess light energy to prevent the photodamage of RCs has been previously interpreted [37]. Here, despite the high involvement of PE in the light-induced energetic decoupling of PBsomes, we further found specifically that the different roles of BPE that carries chromophoric γ-subunit and b-PE that lacks c subunit in the photoprotective mechanism of red algae. In addition to the roles in PBPs assembly and energy migration, the chromophoric γ-subunit is preferentially sensitive to the intense light, and probably functions in the photoprotection of PBsome. As a primitive unicellular red alga, *P. cruentum* contains the specific γ-subunits and colorless linker polypeptides to assemble B-PE and b-PE hexamer complexes, respectively, in the PBsome rods. The evolution of cyanobacteria and red algae is revealed to be accompanied by the evolution of PBPs [8]. The chromophore variety and increasing number extend the absorbance spectrum and enhance the absorption capacity, enabling the photosynthetic organisms to survive in various environments. Furthermore, our data provide new insights into the biological roles of the chromophore variety: the spectral variety of PBPs in intact PBsomes and the appearance of chromophoric γ-subunit may generate a multi-step photoprotection to effectively prevent photodamage of photosynthetic RCs in response to excess excitation energy *in vivo*.

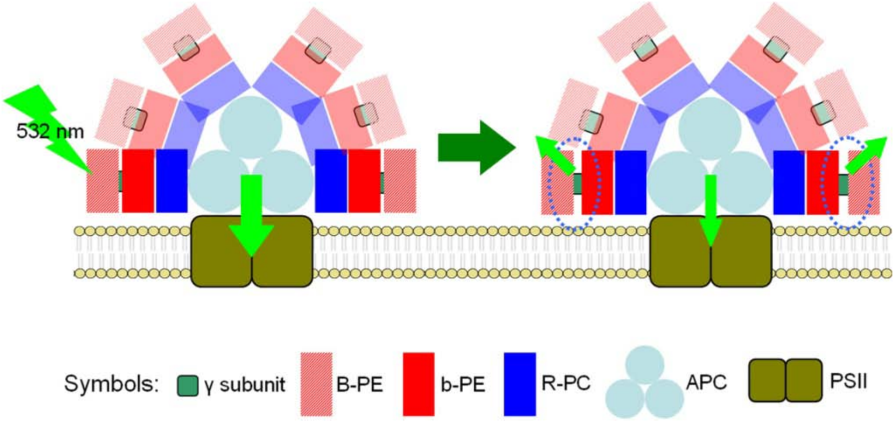

Figure 9. Schematic model of light-induced energetic decoupling of PBsomes. Arrows represent the fluorescence emissions from PBsome components during photobleaching. Dashed circles present the proposed decoupling sites within the PBsome.

References

1. MacColl R (1998) Cyanobacterial phycobilisomes. J Struct Biol 124: 311–334.
2. Adir N (2005) Elucidation of the molecular structures of components of the phycobilisome: reconstructing a giant. Photosynth Res 85: 15–32.
3. Liu LN, Chen XL, Zhang YZ, Zhou BC (2005) Characterization, structure and function of linker polypeptides in phycobilisomes of cyanobacteria and red algae:an overview. Biochim Biophys Acta 1708: 133–142.
4. Gantt E, Lipschultz CA, Zilinskas B (1976) Further evidence for a phycobilisome model from selective dissociation, fluorescence emission, immunoprecipitation,and electron microscopy. Biochim Biophys Acta 430: 375–388.
5. Arteni AA, Liu LN, Aartsma TJ, Zhang YZ, Zhou BC, et al. (2008) Structure and organization of phycobilisomes on membranes of the red alga Porphyridium cruentum. Photosynth Res 95: 169–174.
6. Gantt E, Lipschultz CA (1974) Phycobilisomes of Porphyridium cruentum: pigment analysis. Biochemistry 13: 2960–2966.
7. Ficner R, Huber R (1993) Refined crystal structure of phycoerythrin from Porphyridium cruentum at 0.23-nm resolution and localization of the gamma subunit. Eur J Biochem 218: 103–106.
8. Apt KE, Collier JL, Grossman AR (1995) Evolution of the phycobiliproteins. J Mol Biol 248: 79–96.
9. Kirilovsky D (2007) Photoprotection in cyanobacteria: the orange carotenoid protein (OCP)-related non-photochemical-quenching mechanism. Photosynth Res 93: 7–16.
10. Wilson A, Boulay C, Wilde A, Kerfeld CA, Kirilovsky D (2007) Light-induced energy dissipation in iron-starved cyanobacteria: roles of OCP and IsiA proteins. Plant Cell 19: 656–672.
11. Wilson A, Ajlani G, Verbavatz JM, Vass I, Kerfeld CA, et al. (2006) A soluble carotenoid protein involved in phycobilisome-related energy dissipation in cyanobacteria. Plant Cell 18: 992–1007.
12. Luong AK, Gradinaru CC, Chandler DW, Hayden CC (2005) Simultaneous time- and wavelength-resolved fluorescence microscopy of single molecules. J Phys Chem B 109: 15691–15698.
13. Bopp MA, Jia Y, Li L, Cogdell RJ, Hochstrasser RM (1997) Fluorescence and photobleaching dynamics of single light-harvesting complexes. Proc Natl Acad Sci U S A 94: 10630–10635.
14. Bopp MA, Sytnik A, Howard TD, Cogdell RJ, Hochstrasser RM (1999) The dynamics of structural deformations of immobilized single light-harvesting complexes. Proc Natl Acad Sci U S A 96: 11271–11276.
15. Hofmann C, Ketelaars M, Matsushita M, Michel H, Aartsma TJ, et al. (2003) Single-molecule study of the electronic couplings in a circular array of molecules: light-harvesting-2 complex from Rhodospirillum molischianum. Phys Rev Lett 90: 013004.
16. Hofmann C, Aartsma TJ, Michel H, Kohler J (2003) Direct observation of tiers in the energy landscape of a chromoprotein: a single-molecule study. Proc Natl Acad Sci U S A 100: 15534–15538.
17. Vacha F, Bumba L, Kaftan D, Vacha M (2005) Microscopy and single molecule detection in photosynthesis. Micron 36: 483–502.

18. van Oijen AM, Ketelaars M, Kohler J, Aartsma TJ, Schmidt J (1999) Unraveling the electronic structure of individual photosynthetic pigment-protein complexes. Science 285: 400–402.

19. Wu M, Goodwin PM, Ambrose WP, Keller RA (1996) Photochemistry and fluorescence emission dynamics of single molecules in solution: B-phycoerythrin. J Phys Chem 100: 17406–17409.

20. Zehetmayer P, Hellerer T, Parbel A, Scheer H, Zumbusch A (2002) Spectroscopy of single phycoerythrocyanin monomers: dark state identification and observation of energy transfer heterogeneities. Biophys J 83: 407–415.

21. Zehetmayer P, Kupka M, Scheer H, Zumbusch A (2004) Energy transfer in monomeric phycoerythrocyanin. Biochim Biophys Acta 1608: 35–44.

22. Ying L, Xie XS (1998) Fluorescence spectroscopy, exciton dynamics, and photochemistry of single allophycocyanin trimers. J Phys Chem B 102: 10399–10409.

23. Mackowski S, Woermke S, Brotosudarmo TH, Jung C, Hiller RG, et al. (2007) Energy transfer in reconstituted peridinin-chlorophyll-protein complex: ensemble and single molecule spectroscopy studies. Biophys J 93: 3249–3258.

24. Wormke S, Mackowski S, Brotosudarmo THP, Brauchle C, Garcia A, et al. (2007) Detection of single biomolecule fluorescence excited through energy transfer: Application to light-harvesting complexes. Appl Phys Lett 90: 193901–193903.

25. Glazer AN (1984) Phycobilisome. A macromolecular complex optimized for light energy transfer. Biochim Biophys Acta 768: 29–51.

26. Lao K, Glazer AN (1996) Ultraviolet-B photodestruction of a light-harvesting complex. Proc Natl Acad Sci U S A 93: 5258–5263.

27. Gantt E, Lipschultz CA (1972) Phycobilisomes of Porphyridium cruentum. I. Isolation. J Cell Biol 54: 313–324.

28. Biggins J, Campbell CL, Bruce D (1984) Mechanism of the light state transition in photosynthesis. 2. Analysis of phosphorylated polypeptides in the red alga, Porphyridium cruentum. Biochim Biophys Acta 767: 138–144.

29. Sivan A, Arad SM (1993) Induction and characterization of pigment mutants in the red microalga Porphyridium sp (Rhodophyceae). Phycologia 32: 68–72.

30. Sivan A, Thomas JC, Dubacq JP, Moppes D, Arad S (1995) Protoplast fusion and genetic complementation of pigment mutations in the red microalga Porphyridium sp. J Phycol 31: 167–172.

31. Suter GW, Mazzola P, Wendler J, Holzwarth AR (1984) Fluorescence decay kinetics in phycobilisomes isolated from the bluegreen alga Synechococcus 6301. Biochim Biophys Acta - Bioenergetics 766: 269–276.

32. Rakhimberdieva MG, Stadnichuk IN, Elanskaya IV, Karapetyan NV (2004) Carotenoid-induced quenching of the phycobilisome fluorescence in photosystem II-deficient mutant of Synechocystis sp. FEBS Lett 574: 85–88.

33. Rakhimberdieva MG, Bolychevtseva YV, Elanskaya IV, Karapetyan NV (2007) Protein-protein interactions in carotenoid triggered quenching of phycobilisome fluorescence in Synechocystis sp. PCC 6803. FEBS Lett 581: 2429–2433.

34. Stoitchkova K, Zsiros O, Javorfi T, Pali T, Andreeva A, et al. (2007) Heat- and light-induced reorganizations in the phycobilisome antenna of Synechocystis sp. PCC 6803. Thermo-optic effect. Biochim Biophys Acta 1767: 750–756.

35. Rinalducci S, Pedersen JZ, Zolla L (2008) Generation of reactive oxygen species upon strong visible light irradiation of isolated phycobilisomes from Synechocystis PCC 6803. Biochim Biophys Acta 1777: 417–424.

36. Six C, Joubin L, Partensky F, Holtzendorff J, Garczarek L (2007) UV-induced phycobilisome dismantling in the marine picocyanobacterium Synechococcus sp. WH8102. Photosynth Res 92: 77–86.

37. Wyman M, Gregory RP, Carr NG (1985) Novel role for phycoerythrin in a marine cyanobacterium, Synechococcus strain DC2. Science 230: 818–820.

38. Jones RF, Speer HL, Kury W (1963) Studies on the growth of the red alga Porphyridium cruentum. Physiol Plant 16: 636–643.

Chapter 3

Probing redox proteins on a gold surface by single molecule fluorescence spectroscopy[†]

[†] Elmalk AT, Salverda JM, Tabares LC, Canters GW, Aartsma TJ (2012) Probing redox proteins on a gold surface by single molecule fluorescence spectroscopy. Journal of Chemical Physics 136: 235101

Summary. *The interaction between the fluorescently labeled redox protein, azurin, and a thin gold film is characterized using single-molecule fluorescence intensity and lifetime measurements. Fluorescence quenching starts at distances below 2.5 nm from the gold surface. At shorter distances the quenching may increase up to 80% for direct attachment of the protein to bare gold. Outside of the quenching range, a four-fold enhancement of the fluorescence is observed with increasing roughness of the gold layer. Fluorescence-detected redox activity of individual azurin molecules, with a lifetime switching ratio of 0.4, is demonstrated for the first time close to a gold surface.*

3.1. Introduction

Redox reactions drive a plethora of biological and chemical processes ranging from photosynthesis and respiration to industrial catalysis and the operation of fuel cells [1, 2]. Recently, due to their unique properties redox proteins have gained strong interest because of possible applications in biomolecular electronics and biosensing. However, to manipulate single redox proteins and attach them to an electrode surface without affecting their biochemical activity is a challenge. Gold has been used extensively for this purpose as it has a higher surface stability than other metals or non-metallic electrodes, while the surface chemistry of gold is well understood [3-5].

To monitor the activity of redox proteins under single-molecule conditions, it is necessary to maximize sensitivity and specificity. Our recent research efforts have targeted the implementation of a novel fluorescence method allowing single-molecule observation of redox events with enhanced sensitivity [6-9]. Optical tracking of electrochemical events made it possible to determine the electrochemical parameters and redox activity of ensembles of as few as 100 protein molecules [10-12]

For the combination of fluorescent redox state detection and electronic control the protein together with its fluorescent label needs to be placed close to an electrode, usually a metal surface. This raises questions about the fluorophore-metal interaction. The subject has raised considerable interest in recent years because of fundamental and application-oriented reasons [13]. The effect of a metal surface on a nearby fluorophore can lead to both enhancement and quenching of the fluorescence [14-24].

A striking aspect of the fluorophore-metal interaction is its strong and complicated distance dependence. At values of d (where d is the distance between the fluorophore or dye and the metal surface) that are comparable to the wavelength of the exciting light (d > 500 nm), interference occurs (both positive and negative) between light emitted in a direction away from the metal surface and light emitted towards the metal surface and reflected off it [24-26].

At intermediate ranges (10 nm < d < 500 nm), the interaction of the molecular transition dipole with the nearby metal surface plasmons can lead to quenching of the emission as well as to enhanced excitation rates [18, 20, 26]. At very close ranges (d < 10 nm), a surface energy transfer model (SET) has been proposed as a quenching mechanism. SET denotes the energy transfer from an oscillating dipole to the free conduction electrons of the metal [27, 28]. It has been found that the quenching efficiency is proportional to $1/d^{3}$ [18, 24, 26, 29]. Even at these very small distances enhancement of the excitation rate can occur, especially for rough metal surfaces. This is the regime that we focus on.

We studied the fluorescence of labeled redox proteins immobilized on coated glass or on gold films (bare or coated with a self-assembling monolayer (SAM)) as a function of the thickness of the gold film and the thickness of the SAM. Intensity and lifetime measurements allowed for the separation of enhancement and quenching effects on the fluorescence. In addition, the effect of the redox state on the fluorescence of the labeled protein was investigated. While this effect has been successfully studied for the enzyme nitrite reductase (NiR) at the single molecule level [7], the influence of a nearby Au layer has not been reported so far.

The results of the present study are of relevance for the implementation of redox proteins in bio-optoelectronic (nano)devices. To the best of our knowledge, this study is the first successful attempt to examine the single molecule fluorescence lifetimes of labeled redox proteins immobilized on a metal surface.

3.2 Experimental Methods

Protein labeling. Azurin from *Pseudomonas aeruginosa* was used as a redox protein model. It is a small (M_r=14.6 kDa) blue copper protein that functions as an electron carrier possibly in the oxidative stress response of the organism[30]. The intense 600 nm absorption band of this protein in the oxidized state is absent in the reduced state, which makes it suitable for redox state detection by fluorescent labeling. A covalently attached fluorescent label and the redox cofactor (the Cu center) form a FRET pair by which a change in redox state is reflected by a change in fluorescence intensity and fluorescence lifetime [7, 8, 31, 32].

Preparation and purification of the K27C azurin variant was done as previously described [32]. The protein was labeled by incubation of a solution of 0.5 mM protein in 20 mM Hepes, pH 8.3, with a 5 times molar excess of Atto-655 succinimidyl ester (ATTO-TEC GmbH, Germany) for 1 h at room temperature for N-terminal labeling. The unbound dye was removed using centrispin-10 columns (Princeton Separations; Adelphia, NJ, USA). Labeled protein was diluted with 20 mM Hepes buffer, pH 7.0, to the desired final concentrations as determined by UV-vis spectroscopy.

Preparation of surfaces. All glass slides (Menzel, Germany) used to prepare gold films and silanized glass were sonicated in spectrometer grade acetone (30 min), washed several times with water (Millipore water), dipped in 10% NaOH/H_2O (30 min), washed again several times with water and stored in methanol. Before use the cover slips were dried and ozone-cleaned (UVP PR-100 UV-ozone photoreactor) for 1 h immediately before silanization or sputtering.

For the preparation of gold films, first, a 1 nm thick adhesion layer of molybdenum-germanium (MoGe) films was prepared by depositing MoGe onto freshly cleaned glass slides by magnetron sputtering using an ATC 1800-F system (AJA corporation). The MoGe films were sputtered with a deposition rate of 1.32 nm/min (10 mTorr Argon environment). Second, gold films of specified thickness were prepared by sputtering at a deposition rate of 9.06 nm/min (10 mTorr environment composed of a mixture of argon with 1% oxygen) on top of the MoGe film. The Au films were used immediately after preparation. Their thickness was varied between 10 and 100 nm.

Atomic force microscopy. Atomic force microscopy (AFM) imaging of the samples was performed with a commercial AFM microscope (Nanoscope IIIa, Veeco, USA). Tapping mode images in air were acquired with an E-scanner (14 μm range), using Si probes with a resonance frequency of 75 kHz and a nominal spring constant of 2.8 N m^{-1}.

Protein immobilization. In one type of experiment the labeled protein was immobilized on a glass slide or a sputtered bare gold surface for optical measurements. Immobilization in the former case was achieved by depositing a layer of a 100:1 mixture of triethoxysilane (TES) and mercaptopropyl trimethoxysilane (MPTS) on a cleaned glass slide (chemicals from Fluka, used as received). The K27C azurin was bound to the silanized glass through a 1–11-bismaleimidotetraethyleneglycol linker (BM(PEO)$_3$, Pierce) as described by Kuznetsova et al. [7]. Immobilization on bare gold was realized by incubating the Au film with a solution of the K27C azurin overnight at room temperature and rinsing the surface afterwards by flushing with buffer. This gave reproducible results of specifically immobilized K27C azurin without protein aggregation at the surface.

In a second type of experiment mixed SAMs of 1,n-alkanedithiol $HS(CH_2)_nSH$ (n= 4, 6, 8 and 10) and OH-terminated alkanethiol $HS(CH_2)_mOH$ (m = n-2, except for n=4 in which case we chose m=3), denoted by C*n*d (‘d’ denoting di-thiol), were prepared by immersing slides with freshly sputtered Au films into a 2-propanol solution containing a mixture of $HS(CH_2)_mOH$ (10 mM) and $HS(CH_2)_nSH$ (1 mM) overnight at room temperature [33] (all chemicals purchased from Aldrich Chemicals, dissolved in 2-propanol). The choice for n>m, *i.e.*, for an alkanedithiol that is longer than the OH-terminated alkanethiol, was made to expose the reactive thiol of the linker. It provides the reaction site for immobilization of the K27C azurin, while the OH-terminated alkanethiol serves as the diluant to control the density of immobilized protein, as it prevents non-specific binding of K27C azurin (Fig. 1). Au slides were removed from solution, rinsed extensively with 2-propanol, and dried in a pure N_2 flow. A 200 pM solution of the labeled azurin (Az) in 20 mM Hepes buffer, pH 7, was deposited onto the SAM-covered Au slide and left to incubate overnight at 4°C. The slide was then rinsed with 20 mM Hepes buffer (pH 7) to remove free azurin. Measurements were performed in the same 20 mM Hepes buffer (pH 7) as used for immobilization.

In all experiments reduction was performed with sodium ascorbate, oxidation was performed by adding potassium ferricyanide. Reducing and oxidizing agents were added from freshly prepared stock solutions to final concentrations of 10mM sodium ascorbate or 1 mM potassium ferricyanide. The thickness of the sputtered Au films was varied between 10 and 100 nm.

The success of the immobilization procedure was verified using tapping mode AFM (Figures S1 and S2 in the supplementary material of reference 34)[34]. For the mixed alkanedithiol/OH-alkanethiol SAMs, distinct features with a height of 4.0±0.2 nm were observed. This value corresponds with the size of azurin (3.5 x 3.5 x 4.4 nm^3) as determined by X-ray crystallography [35]. As a control for the specificity of the attachment

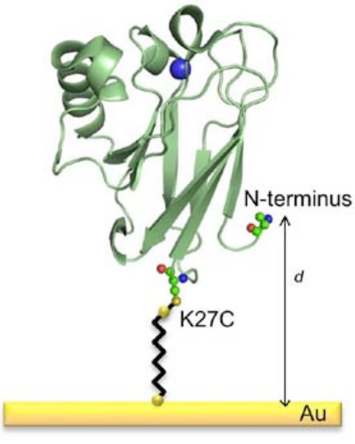

Figure 1. Representation of the azurin (K27C) structure and schematic view of the covalent coupling of azurin to a SAM-modified Au surface. The distance *d* between the dye label at the N-terminus and the Au surface is indicated.

on the SAM, azurin was incubated on a SAM of 8-mercapto-1-octanol only, applied on a 20 nm Au film. No protein was found on this surface after rinsing with pure buffer solution. The immobilization strategy described above, thus, establishes an effective and specific coupling between the protein and the gold surface [3, 36-38].

Table 1. Root-mean square (rms) values of height variations for various Au films, as determined by AFM.

Au thickness (nm)	rms (nm)
10	0.2
20	0.3
50	1.4
100	1.7

The change of surface morphology of the gold film with increasing thickness was also characterized by AFM. Calculated roughness values are given in Table 1. Thin sputtered gold films (10 nm) have root-mean square (rms) height variations of about 0.2 nm. With increasing thickness of the Au film, the roughness goes up, reaching 1.7 nm rms value at 100 nm thickness. The thin Au films exhibit an exceptionally smooth and homogenous surface due to the presence of the MoGe wetting layer. At thicknesses above 20 nm the effect of the wetting layer diminishes and the surface roughness of thick Au films has a value more typical of a sputtered metal surface.

Confocal microscopy. The fluorescence measurements were conducted on a home-built sample scanning confocal microscope. For fluorescence excitation a pulsed picosecond diode laser (PDL 800-B, PicoQuant GmbH) with an output wavelength of 639 nm was sent through a narrow-band clean-up filter (LD01-640/8-25, Semrock, USA), coupled into a single-mode fiber and reflected by a dichroic mirror (Z 532/633 M, Chroma technology, USA) to a high numerical aperture oil objective (100× oil, NA 1.4, Zeiss, Germany) and focused to a diffraction-limited spot (~300 nm) on the sample surface. The power density at the sample was 0.5–1 kW/cm^2. Epi-fluorescence from the labeled azurin was filtered with a band filter (D 675/50 M, Chroma technology, USA) and focused with a +45 mm focal length achromatic lens on to the active area of a single photon avalanche photodiode (Perkin-Elmer SPCM-AQR-14). The microscope was equipped with Time-Correlated Single-Photon Counting (TCSPC) capabilities. The data acquisition was done by the TimeHarp 200 TCSPC PC-board operating in the special Time-Tagged Time-Resolved (T3R) mode, which stores the arrival time of each individual photon event [39]. Samples were

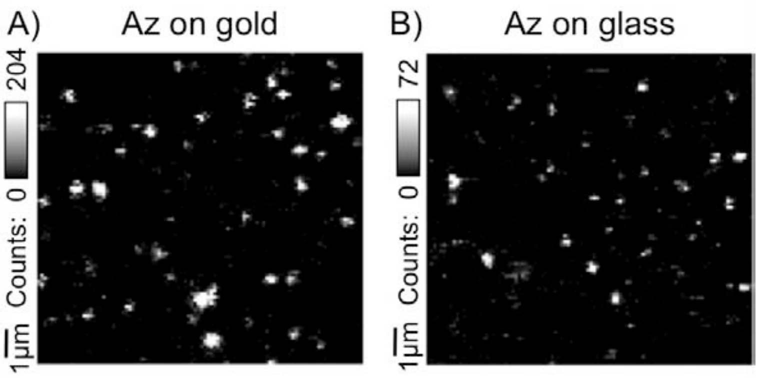

Figure 2. 10x10 μm^2 fluorescence images of immobilized K27C azurin (20 mM Hepes buffer, pH 7). A) on a 100nm Au film coated with C*10*d SAM. B) on glass. The scale bars show the intensity counts in 1.8 msec bin time. The fluorescence intensities of individual spots on the 100 nm coated Au film are brighter than on glass (notice different scale bars).

mounted onto a Physik Instrumente P-517 nanopositioner. Scanning, accurate positioning, data collection and analysis were performed by the Picoquant SymPho-Time software (PicoQuant GmbH).

The excitation beam was focused through (transmissive mode) or impinged on (direct mode) the gold films in order to excite the molecules on the surface. The direct mode was used for the Au films with a thickness of 20 nm and higher, because they are not transparent. For thicknesses of 10 and 15 nm the transmissive mode of detection was compared to the direct mode, using the same sample in both geometries. Identical results were obtained in both cases.

Life time analysis. The fluorescence intensity decays were analyzed as the sum of mono-exponential decays [40]:

$$I(t) = \sum_{i=1}^{n} \alpha_i \exp(-t/\tau_i)\,, \qquad [1]$$

where τ_i are the decay times and α_i are the amplitudes. The contribution of each component to the average intensity is given by

$$f_i = \frac{\alpha_i \tau_i}{\sum_j \alpha_j \tau_j}\,. \qquad [2]$$

The average lifetime of the multi- exponential decay is defined by

$$\bar{\tau} = \sum_i f_i \tau_i \ . \qquad [3]$$

The values of α_i and τ_i were determined using the PicoQuant SymPho-Time software. The data are fitted with a convolution of the instrument response function (IRF) and a sum of exponential decays according to a least-squares criterion [41].

3.3 Results

3.3.1 Fluorescence intensity vs. film thickness

To investigate the effect of **Au film thickness** on the **fluorescence** of labeled azurin, a single-molecule fluorescence experiment was carried out on labeled K27C Az immobilized on Au films of different thicknesses, coated with a C*10*d mixed SAM (no fluorescence quenching occurs for this SAM; vide infra). A characteristic confocal image (10 by 10 µm) of individual reduced azurin molecules on 100 nm thick Au film coated with C*10*d SAM (in buffer) is shown in Fig. 2A. For comparison, we also recorded a confocal fluorescence image of labeled azurin molecules on a glass surface, see Fig. 2B. As can be seen from the scale bars in Fig. 2, there is a difference in fluorescence intensity of roughly a factor of 3-4.

In order to quantitatively compare the fluorescence properties for different azurin molecules and explore the underlying photophysics, we monitored the fluorescence of individual azurin molecules. A typical fluorescence time trace of a single, labeled azurin

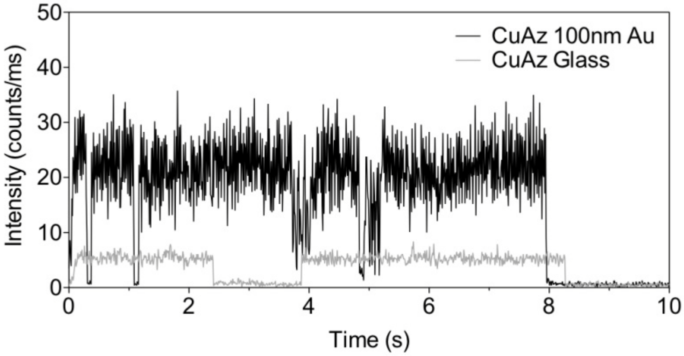

Figure 3. Fluorescence time traces obtained from immobilized reduced Cu-Az (K27C azurin) on 100 nm Au film coated with C*10*d SAM (black) and from reduced Cu-Az on a glass surface (gray).

molecule on a 100 nm Au film coated with a C*10*d mixed SAM is shown in Fig. 3, which corresponds to a four-fold higher fluorescence emission rate than that of azurin on glass (Fig. 3).

In Fig. 4, count rate histograms of collections of individual molecules are shown for azurin on glass and on C*10*d coated Au films, the latter with thicknesses of 20 nm, 50 nm and 100 nm. All measurements were carried out at the same laser intensity of 1 kW/cm^2. The count rate distribution of azurin immobilized on 50 and 100 nm Au films is strongly bimodal,

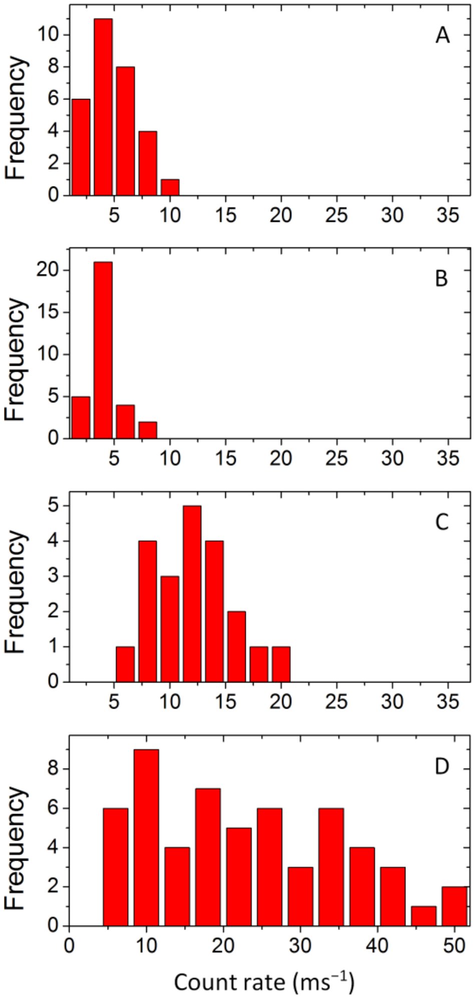

FIG. 4. Intensity count rate histograms for reduced K27C azurin molecules immobilized on silanized glass (A) and on Au films (B: 20 nm, C: 50 nm and D: 100 nm thickness) coated with a C*10*d SAM.

with maxima at 6 and 25 counts/ms. The former count rate is similar to the fluorescence count rate of labeled azurin on glass and on gold films with a thickness of 10 and 20 nm. The high count rate of what is by far the largest fraction (80%) of azurin molecules on 50 and 100 nm Au films suggests a strong fluorescence enhancement as compared to azurin molecules immobilized on glass or 10 and 20 nm Au films. The average enhancement for azurin on 50 and 100 nm Au films as estimated from the count rate histograms in Fig. 4 is four-fold.

The main difference between the thick (50 and 100 nm) and the thin (10 and 20 nm) Au films is the surface roughness (see Table 1). Apparently, the fluorescence enhancement strongly depends on this particular property. In general, the fluorescence near metal surfaces is governed by the distance-dependent competition between quenching and (local-field) enhancement [16, 23]. These aspects were examined in more detail by means of lifetime measurements.

3.3.2. Fluorescence life time vs. SAM thickness

When immobilizing proteins on a SAM-coated Au film the SAM layer constitutes a spacer between the bare gold surface and the protein. By using a series of *n*-alkanedithiols with lengths ranging from 4 to 10 carbon atoms the effect of a **SAM thickness** variation of from 5.9 to 12.5 Å [37, 42-44] on the **fluorescence lifetime** could be studied. The results are shown in Fig. 5 for a 50 nm thick Au film. Fluorescence decays were averaged over more than 500

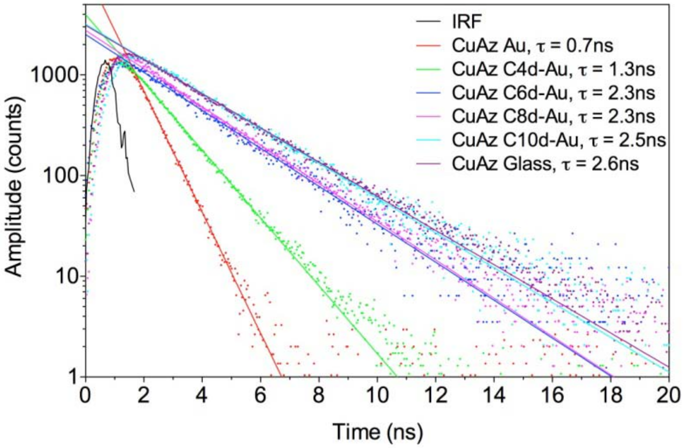

FIG. 5. Fluorescence decay curves of azurin immobilized on glass (purple), immobilized directly on 50 nm Au film (red) and on 50 nm Au films coated with C*4*d (green), C*6*d (blue), C*8*d (magenta) or C*10*d (cyan). IRF (black) is also included. Each decay curve represents an average over more than 500 individual molecules.

single-molecule traces and quantified by fitting to mono-exponential decays convoluted with the instrument response function (IRF). Reduced azurin immobilized on C*10*d, the thickest SAM used, shows approximately the same lifetime as reduced azurin on glass (2.5 resp. 2.6 ns). Significantly reduced lifetimes are observed for the shorter SAMs (C*8*d, C*6*d and C*4*d with lifetimes of 2.3, 2.3 and 1.2 ns respectively), down to 0.7 ns for azurin immobilized directly on Au, see Table 2.

To verify that the observed lifetimes were not affected by redox effects, the experiments were repeated with Zn azurin, which is redox-inactive. The lifetimes were similar to those observed for Cu-azurin. This confirms that the decrease in lifetime is not due to a redox-state dependent interaction between Cu site and dye label [31]. We suggest that the reduced lifetime at shorter distances reflects the fluorescence quenching by molecule-metal interactions. Notably, labeled azurin molecules bound to C*10*d SAM seem to be at a distance which is sufficiently large to prevent fluorescence quenching. Nevertheless, the thickness of this SAM is only 1.3 nm [42]. Apparently, the probed interaction is very short-ranged.

3.3.3 Fluorescence life time vs. Au film thickness

In order to examine the effect of the Au film **thickness** on the **fluorescence lifetime**, the measurement series described above was repeated for Au films with thicknesses of 10, 20, 50 and 100 nm. The fluorescence data were all collected under the same excitation and detection conditions, allowing a direct comparison between the different measurements (Fig. 6). The fluorescence lifetime is found to be completely independent of the Au film thickness, from which it is concluded that the morphology of the Au surface does not affect the degree of fluorescence quenching.

TABLE II. Fluorescence lifetimes of azurin immobilized on glass and on 50 nm Au films coated with SAMs of varying thicknesses.

SAM	τ (ns) [b)]
__ [a)]	0.7±0.1
C4d	1.3±0.1
C6d	2.3±0.1
C8d	2.3±0.1
C10d	2.5±0.1
Glass	2.6±0.1

a) azurin immobilized directly on bare Au; no SAM;.
b) fluorescence lifetime.

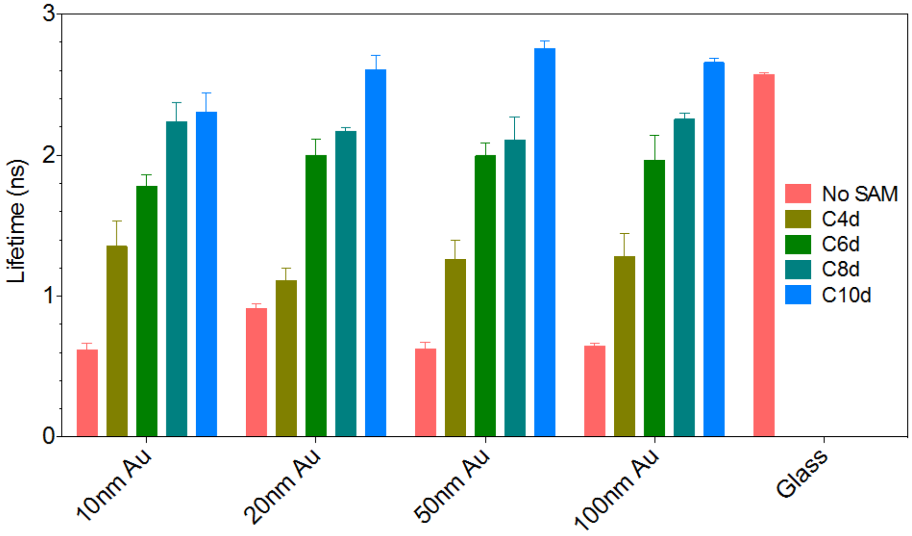

FIG. 6. Fluorescence lifetimes of reduced Cu-Az immobilized on Au films of different film thicknesses (from 10 to 100 nm) that are coated with C*4*d (olive), C*6*d (green), C*8*d (blue-green) and C*10*d (bright blue) SAMs and of reduced Cu-Az adsorbed directly on 50 nm Au (red). Also presented is the lifetime of reduced Cu-Az immobilized on silanized glass (red). The lifetimes were obtained by monitoring the total emission of a 10x10μm^2 surface area. For each bar the lifetimes measured for a number of pictures (varying from 2 to 16) were averaged. The error bars correspond to standard deviations.

Thus, the fluorescence lifetime only depends on the distance between fluorophore and Au surface, independent of film thickness. The shortest fluorescence lifetimes were observed when azurin was adsorbed directly on the Au films, which is to be expected as quenching is known to be stronger at shorter distance. The lifetime of azurin bound to C*10*d is the longest and similar to the lifetime of azurin on glass. Interestingly, azurin bound to C*6*d and C*8*d shows similar lifetimes, suggesting that different SAM chain lengths do not always lead to different SAM thicknesses.

In conclusion it can be stated that, whereas the fluorescence *lifetime* is independent of Au film thickness, the fluorescence *intensity* does depend on it (see Fig. 4). Clearly, two different mechanisms play a role.

3.3.4 Effect of redox state

The experiments reported so far relate to azurin in the reduced state. To check how the redox state of the protein might affect the fluorescence behavior, we also measured the fluorescence intensity and lifetime for azurin in the oxidized state. The redox state could be

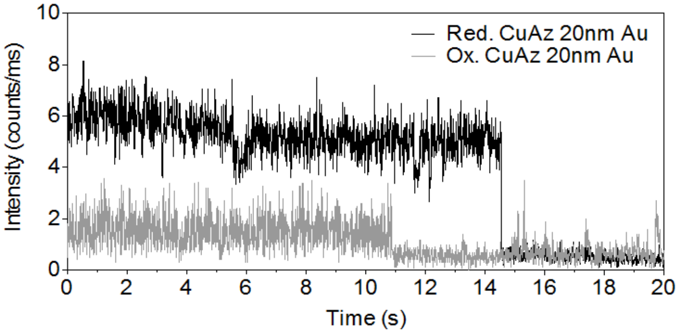

Fiure 7. Time traces for two individual labeled K27C azurin molecules immobilized on a 20 nm Au film coated with C*10*d SAM, one trace for azurin in the reduced state (black, τ_{red} = 2.6 nsec), and one for azurin in oxidized form (gray, τ_{oxid} = 1.6 nsec).

easily controlled by the addition of reducing or oxidizing agents (see above). Figure 7 shows time traces for two individual azurin molecules immobilized on a 20 nm Au film coated with C*10*d SAM, one in the reduced state (black), and one in oxidized form (gray). The intensity ratio between the two states is about a factor of 3 in this instance.

Lifetime histograms are shown in Fig. 8 for oxidized (bottom, left) and reduced (bottom, right) single azurin molecules bound to C*10*d SAM on 20 nm Au films, which appear

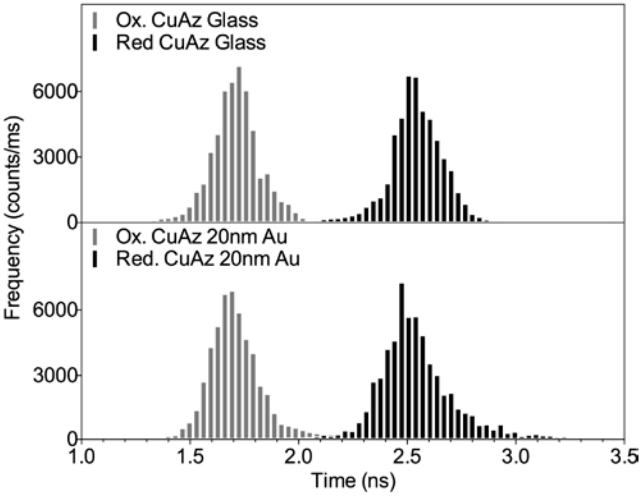

FIG. 8. Fluorescence lifetime histograms of labeled K27C azurin in the oxidized (histograms at the left) and the reduced state (histograms at the right) immobilized on 20 nm Au coated with a C*10*d SAM (bottom) and immobilized on glass (top).

similar to azurin on glass surfaces (top). Reduced and oxidized molecules exhibit a long (2.6±0.2 ns, black bars) and a short lifetime (1.6±0.2 ns, gray bars), respectively. The oxidized azurin lifetimes were found to be independent of the Au film thickness, just as for reduced azurin. For azurin immobilized on a C*8*d SAM on Au films of varying thicknesses the reduced and oxidized forms exhibited lifetimes of 2.3±0.2 ns and 1.1±0.2 ns, respectively. Thus, it is still possible to discern the two redox states in the presence of fluorescence quenching by a metal surface. Lifetimes were also measured for oxidized azurin immobilized on C*6*d and C*4*d SAMs and on bare Au. The results exhibit the same trend as the distance dependent fluorescence quenching data observed for reduced azurin.

3.4 Discussion

In the following we discuss the distance dependence of the fluorescence quenching, the relation between fluorescence enhancement and surface roughness, and the redox switching behavior.

Both quenching and enhancing interactions between fluorophores and metal surfaces have an effect on the fluorescence intensity and lifetime. The fluorescence intensity (below saturation) is proportional to the fluorescence emission rate γ_{em}, which is the product of the excitation rate γ_{exc} and quantum yield q [15] :

$$\gamma_{em} = \gamma_{exc} q \, . \qquad [4]$$

In the absence of a metal surface, the free-space quantum yield q_0 is given by:

$$q_0 = \left(\gamma_r \big/ \gamma_r + \gamma_{nr} \right), \qquad [5]$$

where γ_r is the radiative rate and γ_{nr} the (intrinsic) nonradiative decay rate of the molecule. When the fluorophore is placed near the metal surface, both the excitation rate γ_{exc} and the quantum yield q are modified by the fluorophore-metal interaction [15, 16, 45]. Especially on rough surfaces, γ_{exc} may be increased due to the enhanced local electric field near the metal surface. Interaction of the molecular transition dipole moment with such an enhanced local field may also lead to an increase in the radiative decay rate. An increase in γ_{exc} and/or γ_r will result in an increased emission rate and hence an enhanced fluorescence intensity, but only a change in γ_r will affect the excited state lifetime.

At the very close ranges probed here (fluorophore-metal distance $d < 10$ nm), so-called surface energy transfer (SET) takes place from the excited molecule to the free conduction electrons of the metal. This introduces an additional non-radiative channel (which partly quenches the fluorescence) with rate γ_{set} [16]. As a consequence, the modified quantum yield can be written as

$$q = {\gamma_r}\big/{\gamma_r + \gamma_{nr} + \gamma_{set}} \, . \tag{6}$$

For transfer to a metal occupying the half-space below the dipole, γ_{set} is proportional to 1/*d* [3 18, 24]. This also applies to thin films as long as they are much thicker than *d*, which is the case here.

The competition between the increase of the excitation rate γ_{exc}, the increase of the radiative rate γ_r, and the increase of γ_{set}, which enhances fluorescence quenching, becomes highly significant in the sub-5 nm distance range studied here. We believe that γ_r is not affected in our measurements. This can be concluded from the complete decoupling in our data between the lifetime changes (which only occur for a change in SAM thickness) and the intensity enhancement (which only occurs with a change in Au film thickness). The lifetime is given by

$$\tau = 1\big/{\gamma_r + \gamma_{nr} + \gamma_{set}} \tag{7}$$

while the intensity is proportional to

$$I \approx {\gamma_{exc}\gamma_r}\big/{\gamma_r + \gamma_{nr} + \gamma_{set}} \tag{8}$$

Thus, an increase in γ_r would affect both lifetime and fluorescence enhancement at the same time. Since this is not what is observed, only γ_{set} and γ_{exc} change. To monitor changes in γ_{set}, we look at the thinner gold films, for which there is no enhanced excitation, i.e. γ_{exc} is not affected. For the change in γ_{exc} we look at the data for the thickest SAM (C*10*d), for which the lifetime is unchanged compared to Az on glass, and thus γ_{set} must be zero.

The SAM thickness dependence investigation we have carried out showed that fluorescence emission of labeled azurin is quenched significantly at close distances to the gold surface (Figures 5 and 6). This was observed as a fluorescent lifetime reduction when the alkanethiol spacer length was decreased. We suggest that the fluorescence from labeled azurin immobilized on C*8*d, C*6*d, C*4*d and labeled azurin directly adsorbed on the Au surface is quenched due to the surface energy transfer process. For this we calculate γ_{set} in terms of the unquenched value (found for the C*10*d SAM) $\gamma_0 = \gamma_r + \gamma_{nr}$, using $\tau_0 = 1/\gamma_0$ and

$$\tau = \frac{1}{\gamma_r + \gamma_{nr} + \gamma_{set}} = \frac{1}{\gamma_0 + \gamma_{set}} \qquad [9]$$

which gives

$$\frac{\gamma_{set}}{\gamma_0} = \frac{\tau_0}{\tau} - 1 \qquad [10]$$

(see Table 3). The relation of γ_{set} to the distance is found to be in agreement with the expected $1/d^3$ dependence (Fig. 9), with d as indicated in Fig. 1.

By varying the Au film thickness the dependence of the fluorescence enhancement on the surface roughness was investigated. The enhancement observed for the 50 and 100 nm gold films is attributed to the change in excitation rate caused by local enhancement of the electromagnetic field of the incident light as it interacts with the rough metal surface [40, 46-50]. Fluorescence enhancement for dye molecules directly deposited on rough metallic surfaces has been reported before, also in the sub-5 nm regime [40, 46, 47, 51]. Our data show that this local field enhancement can lead to an increase in the emission rate γ_{em}, and, thereby, in the emission intensity, without altering the radiative decay rate γ_r or introducing any quenching effects. Such a change in intensity without a change in lifetime has been observed previously for a similar dye-metal system [52]. The presence of two populations

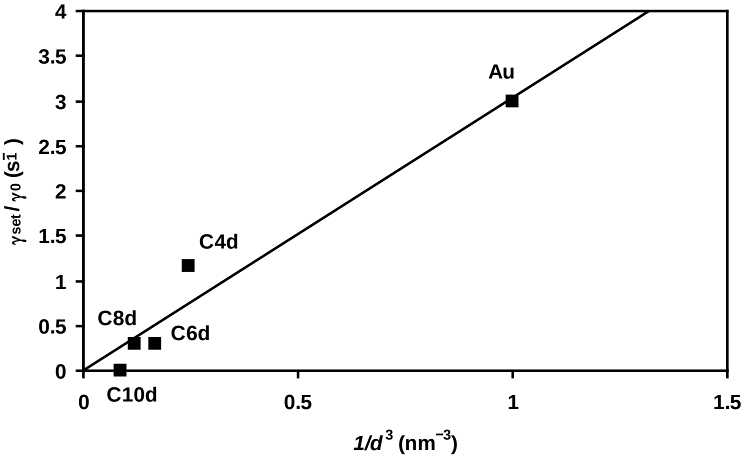

FIG. 9. Dependence of the surface energy transfer rate γ_{set} on the inverse cubic distance, $1/d^3$. The straight line is a linear fit to the data points. Data taken from Table III.

(enhanced and unenhanced emitters, both with the same lifetime, see Fig. 4) is ascribed to the microscopic features of the metal surface. It is well known that the electromagnetic field enhancement depends upon the local surface roughness and the surface morphology [49]. Therefore, local variation in the surface morphology may lead to a variation in the enhancement.

The results on chemical oxidation and reduction of azurin show that the proteins remain redox active on the gold surfaces with the used immobilization strategy. To compare the redox switching as inferred from the intensity time traces and from the fluorescence lifetimes the amount of switching for both types of measurement was calculated. We find the intensity-based switching ratio, Q_{I}, to be 0.7 with

$$Q_{\mathrm{I}} = 1 - (F_{\mathrm{oxid}} / F_{\mathrm{red}}) \qquad [11]$$

in which F_{oxid} and F_{red} denote the fluorescence intensity of the Az in the reduced and oxidized form, respectively [31], while the lifetime-based switching ratio [53], Q_{L},

$$Q_{\mathrm{L}} = 1 - (\tau_{\mathrm{oxid}} / \tau_{\mathrm{red}}) \qquad [12]$$

appears to be 0.4. Here, τ_{oxid} and τ_{red} denote the fluorescence lifetime of the Az in the reduced and oxidized form, respectively. The discrepancy between these two values is currently the subject of further investigation.

SAM	d/ nm [a]	q/q_0 [b]	γ_{set}/γ_0 [c]
none	1	0.25	3
C4d	1.6	0.46	1.2
C6d	1.8	0.77	0.3
C8d	2.0	0.77	0.3
C10d	2.3	1	0

Table 3. Distance dependence of the fluorescence quantum yield q and the surface energy transfer rate γset.

a) Distance from dye label to gold surface, calculated by increasing the SAM thickness by 1 nm to account for the distance between the label and the SAM layer (see Figure 1). SAM thickness was calculated according to Heering and Canters 39 and Love et al. 37, using a C-C bond length of 1.27 Å, a CS endgroup size of 1.79 Å and a SAM/Au angle of 30°.
b) $q/q_0 = \tau/\tau_0$. Lifetime values taken from Table II; τ0 values refer to C10d data.
c) Calculated from Equation [10].

3.5. Conclusion

In summary, the combination of labeled azurin immobilized on Au with a mixed SAM has enabled us to characterize the label-metal interaction in detail. Fluorescence quenching is shown to be a short range effect, reflecting energy transfer between the fluorophore and conduction electrons of the metal. Significant fluorescence enhancement is observed with increasing roughness of the gold layer. These results are in good agreement with theoretical predictions based on earlier, non-single molecule, experiments with fluorophores on metal films.

The results also illustrate how the redox states of a single protein molecule can be investigated by fluorescence lifetime analysis both for Az on gold and for Az on glass. Thus, the combination of FLIM (fluorescence lifetime imaging) with our FRET-based redox detection method provides a new approach for studying the kinetics of biological electron transfer at the single molecule level. Furthermore, the ability to tune the emission properties of labeled redox proteins immobilized on metal surfaces opens a way to design improved biosensing devices.

Acknowledgment.

The authors thank Alessio Andreoni, MSc, for helpful suggestions. They are grateful to Dr. Thyra de Jong and Ing. Lionel Ndamba for protein purification, and to Dr. Razvan Stan and Mohammed Kamran, MSc, for assistance with AFM measurements. M.E. thanks the late Marten Durieux, the Stichting Steunfonds voor Sudanese Studenten, and Al Neelain University for supporting his stay in Leiden. J.M.S. was supported by a Veni Grant from NWO, the Netherlands Foundation for Scientific Research. L.C.T. was supported by the European Community through the EdRox Network (contract no. MRTN-CT-2006-035649) and by NWO, the Netherlands Foundation for Scientific Research through a travel grant (Grant nr. 040.11.223).

Reference List

1. Willner I. Biomaterials for sensors, fuel cells, and circuitry. Science 2002; 298(5602):2407-2408.
2. Gilardi G, Fantuzzi A. Manipulating redox systems: application to nanotechnology. Trends in Biotechnology 2001; 19(11):468-476.
3. Chi QJ, Farver O, Ulstrup J. Long-range protein electron transfer observed at the single-molecule level: In situ mapping of redox-gated tunneling resonance. Proceedings of the National Academy of Sciences of the United States of America 2005; 102(45):16203-16208.
4. Astier Y, Canters GW, Davis JJ, Hill HAO, Verbeet MP, Wijma HJ. Sensing nitrite through a pseudoazurin-nitrite reductase electron transfer relay. Chemphyschem 2005; 6(6):1114-1120.

5. Tepper AWJW. Electrical Contacting of an Assembly of Pseudoazurin and Nitrite Reductase Using DNA-Directed Immobilization. Journal of the American Chemical Society 2010; 132(18):6550-6557.

6. Goldsmith RH, Tabares LC, Kostrz D, Dennison C, Aartsma TJ, Canters GW, Moerner WE. Redox cycling and kinetic analysis of single molecules of solution-phase nitrite reductase. Proceedings of the National Academy of Sciences of the United States of America 2011; 108(42):17269-17274.

7. Kuznetsova S, Zauner G, Aartsma TJ, Engelkamp H, Hatzakis N, Rowan AE, Nolte RJM, Christianen PCM, Canters GW. The enzyme mechanism of nitrite reductase studied at single-molecule level. Proceedings of the National Academy of Sciences of the United States of America 2008; 105(9):3250-3255.

8. Schmauder R, Librizzi F, Canters GW, Schmidt T, Aartsma TJ. The oxidation state of a protein observed molecule-by-molecule. Chemphyschem 2005; 6(7):1381-1386.

9. Tabares LC, Kostrz D, Elmalk, Andreoni A, Dennison C, Aartsma TJ, Canters GW. Fluorescence lifetime analysis of nitrite reductase from Alcaligenes xylosoxidans at the single-molecule level reveals the enzyme mechanism. Chemistry a European Journal 2011; 17:12015-12019.

10. Davis JJ, Burgess H, Zauner G, Kuznetsova S, Salverda J, Aartsma T, Canters GW. Monitoring interfacial bioelectrochemistry using a FRET switch. Journal of Physical Chemistry B 2006; 110(41):20649-20654.

11. Salverda JM, Patil AV, Mizzon G, Kuznetsova S, Zauner G, Akkilic N, Canters GW, Davis JJ, Heering HA, Aartsma TJ. Fluorescent Cyclic Voltammetry of Immobilized Azurin: Direct Observation of Thermodynamic and Kinetic Heterogeneity. Angewandte Chemie-International Edition 2010; 49(33):5776-5779.

12. Krzeminski L, Ndamba L, Canters GW, Aartsma TJ, Evans SD, Jeuken LJC. Spectroelectrochemical Investigation of Intramolecular and Interfacial Electron-Transfer Rates Reveals Differences Between Nitrite Reductase at Rest and During Turnover. Journal of the American Chemical Society 2011; 133(38):15085-15093.

13. Rinaldi R, Biasco A, Maruccio G, Arima V, Visconti P, Cingolani R, Facci P, De Rienzo F, Di Felice R, Molinari E, Verbeet MP, Canters GW. Electronic rectification in protein devices. Applied Physics Letters 2003; 82(3):472-474.

14. Andolfi L, Bruce D, Cannistraro S, Canters GW, Davis JJ, Hill HAO, Crozier J, Verbeet MP, Wrathmell CL, Astier Y. The electrochemical characteristics of blue copper protein monolayers on gold. Journal of Electroanalytical Chemistry 2004; 565(1):21-28.

15. Anger P, Bharadwaj P, Novotny L. Enhancement and quenching of single-molecule fluorescence. Physical Review Letters 2006; 96(11).

16. Bharadwaj P, Novotny L. Spectral dependence of single molecule fluorescence enhancement. Optics Express 2007; 15(21):14266-14274.

17. Chance RR, Prock A, Silbey R. Lifetime of An Emitting Molecule Near A Partially Reflecting Surface. Journal of Chemical Physics 1974; 60(7):2744-2748.

18. Chance RR, Prock A, Silbey R. Comments on Classical Theory of Energy-Transfer. Journal of Chemical Physics 1975; 62(6):2245-2253.

19. Chance RR, Prock A, Silbey R. Comments on Classical-Theory of Energy-Transfer .2. Extension to Higher Multipoles and Anisotropic Media. Journal of Chemical Physics 1976; 65(7):2527-2531.

20. Ford GW, Weber WH. Electromagnetic-Interactions of Molecules with Metal-Surfaces. Physics Reports-Review Section of Physics Letters 1984; 113(4):195-287.
21. Fort E, Gresillon S. Surface enhanced fluorescence. Journal of Physics D-Applied Physics 2008; 41(1).
22. Fu Y, Lakowicz JR. Modification of single molecule fluorescence near metallic nanostructures. Laser & Photonics Reviews 2009; 3(1-2):221-232.
23. Lakowicz JR. Radiative decay engineering 5: metal-enhanced fluorescence and plasmon emission. Analytical Biochemistry 2005; 337(2):171-194.
24. Waldeck DH, Alivisatos AP, Harris CB. Nonradiative Damping of Molecular Electronic Excited-States by Metal-Surfaces. Surface Science 1985; 158(1-3):103-125.
25. Drexhage KH. Influence of A Dielectric Interface on Fluorescence Decay Time. Bulletin of the American Physical Society 1969; 14(8):873-&.
26. Hellen EH, Axelrod D. Fluorescence Emission at Dielectric and Metal-Film Interfaces. Journal of the Optical Society of America B-Optical Physics 1987; 4(3):337-350.
27. Yun CS, Javier A, Jennings T, Fisher M, Hira S, Peterson S, Hopkins B, Reich NO, Strouse GF. Nanometal surface energy transfer in optical rulers, breaking the FRET barrier. Journal of the American Chemical Society 2005; 127(9):3115-3119.
28. Persson BNJ, Lang ND. Electron-Hole-Pair Quenching of Excited-States Near A Metal. Physical Review B 1982; 26(10):5409-5415.
29. Danos L, Greef R, Markvart T. Efficient fluorescence quenching near crystalline silicon from Langmuir-Blodgett dye films. Thin Solid Films 2008; 516(20):7251-7255.
30. Vijgenboom E, Busch JE, Canters GW. In vivo studies disprove an obligatory role of azurin in denitrification in Pseudomonas aeruginosa and show that azu expression is under control of RpoS and ANR. Microbiology-Sgm 1997; 143:2853-2863.
31. Schmauder R, Alagaratnam S, Chan C, Schmidt T, Canters GW, Aartsma TJ. Sensitive detection of the redox state of copper proteins using fluorescence. Journal of Biological Inorganic Chemistry 2005; 10(6):683-687.
32. Kuznetsova S, Zauner G, Schmauder R, Mayboroda OA, Deelder AM, Aartsma TJ, Canters GW. A Forster-resonance-energy transfer-based method for fluorescence detection of the protein redox state. Analytical Biochemistry 2006; 350(1):52-60.
33. Cui XD, Primak A, Zarate X, Tomfohr J, Sankey OF, Moore AL, Moore TA, Gust D, Harris G, Lindsay SM. Reproducible measurement of single-molecule conductivity. Science 2001; 294(5542):571-574.
34. See supplementary material at XXXX for additional figures illustrating the features of azurin molecules on a C10d mixed SAM on gold and the difference in roughness between a 10 nm and a 100nm Au film
35. Nar H, Messerschmidt A, Huber R, Vandekamp M, Canters GW. Crystal-Structure Analysis of Oxidized Pseudomonas-Aeruginosa Azurin at Ph 5.5 and Ph 9.0 - A Ph-Induced Conformational Transition Involves A Peptide-Bond Flip. Journal of Molecular Biology 1991; 221(3):765-772.
36. Wink T, vanZuilen SJ, Bult A, vanBennekom WP. Self-assembled monolayers for biosensors. Analyst 1997; 122(4):R43-R50.

37. Love JC, Estroff LA, Kriebel JK, Nuzzo RG, Whitesides GM. Self-assembled monolayers of thiolates on metals as a form of nanotechnology. Chemical Reviews 2005; 105(4):1103-1169.

38. Qu D, Kim BC, Lee CWJ, Uosaki K. 1,n-Alkanedithiol (n=2, 4, 6, 8, 10) Self-Assembled Monolayers on Au(111): Electrochemical and Theoretical Approach. Bulletin of the Korean Chemical Society 2009; 30(11):2549-2554.

39. Benda A, Hof M, Wahl M, Patting M, Erdmann R, Kapusta P. TCSPC upgrade of a confocal FCS microscope. Review of Scientific Instruments 2005; 76(3).

40. Zhang J, Lakowicz JR. Metal-enhanced fluorescence of an organic fluorophore using gold particles. Optics Express 2007; 15(5):2598-2606.

41. Ray K, Zhang J, Lakowicz JR. Fluorescence lifetime correlation spectroscopic study of fluorophore-labeled silver nanoparticles. Analytical Chemistry 2008; 80(19):7313-7318.

42. Heering HA, Canters GW. Activating Redox Enzymes through Immobilisation and Wiring. In: Davis J. J. (ed) Engineering the Bioelectronic Interface: Applications to Analyte Biosensing and Protein Detection. Royal Society of Chemistry: 2009; pp 119-152.

43. O'Dwyer C, Gay G, de Lesegno BV, Weiner J. The nature of alkanethiol self-assembled monolayer adsorption on sputtered gold substrates. Langmuir 2004; 20(19):8172-8182.

44. Yao X, Wang JX, Zhou FM, Wang J, Tao NJ. Quantification of redox-induced thickness changes of 11-ferrocenylundecanethiol self-assembled monolayers by electrochemical surface plasmon resonance. Journal of Physical Chemistry B 2004; 108(22):7206-7212.

45. Kelly KL, Coronado E, Zhao LL, Schatz GC. The optical properties of metal nanoparticles: The influence of size, shape, and dielectric environment. Journal of Physical Chemistry B 2003; 107(3):668-677.

46. Aroca R, Kovacs GJ, Jennings CA, Loutfy RO, Vincett PS. Fluorescence Enhancement from Langmuir-Blodgett Monolayers on Silver Island Films. Langmuir 1988; 4(3):518-521.

47. Chumanov G, Sokolov K, Gregory BW, Cotton TM. Colloidal Metal-Films As A Substrate for Surface-Enhanced Spectroscopy. Journal of Physical Chemistry 1995; 99(23):9466-9471.

48. Biteen JS, Pacifici D, Lewis NS, Atwater HA. Enhanced radiative emission rate and quantum efficiency in coupled silicon nanocrystal-nanostructured gold emitters. Nano Letters 2005; 5(9):1768-1773.

49. Shen H, Lu GW, Ou MG, Marquette CA, Ledoux G, Roux S, Tillement O, Perriat P, Cheng BL, Chen ZH. How the morphology of biochips roughness increases surface-enhanced chemiluminescence. Chemical Physics Letters 2007; 439(1-3):105-109.

50. Wokaun A, Lutz HP, King AP, Wild UP, Ernst RR. Energy-Transfer in Surface Enhanced Luminescence. Journal of Chemical Physics 1983; 79(1):509-514.

51. Sokolov K, Chumanov G, Cotton TM. Enhancement of molecular fluorescence near the surface of colloidal metal films. Analytical Chemistry 1998; 70(18):3898-3905.

52. Aussenegg FR, Leitner A, Lippitsch ME, Reinisch H, Riegler M. Novel Aspects of Fluorescence Lifetime for Molecules Positioned Close to Metal-Surfaces. Surface Science 1987; 189:935-945.

53. Sapsford KE, Berti L, Medintz IL. Materials for fluorescence resonance energy transfer analysis: Beyond traditional donor-acceptor combinations. Angewandte Chemie-International Edition 2006; 45(28):4562-4588.

Chapter 4

Enhancement and quenching of the fluorescence of labeled single proteins immobilized on gold nanoparticles[†]

[†] Elmalk AT, Tabares LC, Salverda JM, Gaiduk A, Orrit M, Canters GW, Aartsma TJ (2012) Single-Molecule Activity of Oxido-Reductases Attached to Gold Nanoparticles. Submitted for publication.

Summary. *We report on a new method to measure the redox activity of oxido-reductases as a function of time at the single molecule level under high amplicifation and with increased sensitivity. The enzymes are fluorescently labeled so that the fluorescence intensity of the label reflects the redox state of the enzyme's active site. Amplification is realized by immobilization of enzyme molecules on gold nanoparticles (AuNPs). The method is illustrated by using a labeled 14 kDa large copper protein (i.e., azurin (Az) from Pseudomonas aeruginosa) and immobilizing it on gold AuNPs of varying size (1.4-80 nm). The Zn substituted variant is used as a control. Intensity and life time variations are analyzed quantitatively by taking into account the influence of the AuNP on the fluorophore excitation rate and quantum yield. Attachment of fluorescently labeled CuAz to a AuNP may lead to a tenfold enhancement of the sensitivity for detecting a redox change of the protein. These findings open new ways to study hitherto unexplored mechanistic details of oxido-reductases. They are also of relevance for the design of biosensors and devices for electronic data storage.*

1. Introduction

Nanoparticles (NPs) of noble metals like Au and Ag have been at the center of attention[1-12] (see also reviews[13-15] and references therein) because of their unique optical properties. These properties derive from the collective oscillation of the confined conduction electrons. Surface plasmon resonance (SPR) gives rise to absorption in the visible region with very high extinction coefficients (typically 10^9 M^{-1} cm^{-1} at around 500 nm for a 20 nm AuNP, for instance[16]), very intense Rayleigh scattering, and a strong enhancement of the local electric field near the nanoparticle surface[13, 17-21]. Because of these properties, the use of NPs as optical labels has been advocated as an alternative to fluorescent dyes or quantum dots[17, 21-23].

NPs have been proposed as read-outs for interparticle spacing and local dielectric as their optical properties markedly depend on these parameters[5, 15, 17, 18, 24]. NPs can strongly enhance the fluorescence and photostability of nearby fluorophores and may find application in new fluorescent high-throughput detection schemes at single molecule level [22, 25, 26]. All these properties in combination with their electrical conductivity make NPs suitable for possible applications as electrically conducting links in optical biosensors[27, 28].

Fluorescence enhancement by NPs and their application in biotechnology is a relatively new subject [3, 4, 6, 12, 13, 15, 20]. Fluorophores can be described as oscillating point dipoles and when the fluorophore is localized near a metal surface, its oscillator strength and, therefore, its fluorescence can be enhanced [29-31]. Three different near-field interactions between the fluorophore and the NP have to be taken into account in the description of this phenomenon [3, 5, 20, 21, 32-36]. Firstly, the *excitation rate* can be enhanced due to an increase of the oscillating electromagnetic field strength close to the nanoparticle. Secondly, in a similar way the *radiative rate* of the excited fluorophore can be increased. And, finally, the fluorescence may be *quenched* by energy transfer from the excited fluorophore to the conduction electrons in the NP. Depending on which term is dominant the fluorescence may be enhanced or decreased [3-5, 11, 12, 20]. It has proven difficult in the past to obtain reliable quantitative measurements of the fluorescence enhancement effect, especially at distances below a few nm from the NP surface[3, 12] and widely different fluorescence dynamics have been reported for dye-NP systems [3, 6, 12, 37, 38].

Here, the effect of nanoparticle size (ranging from 1.4 to 80 nm) on the fluorescence of an attached (fluorescently labeled) azurin molecule is investigated. Azurin (Az) from *Pseudomona aeruginosa* is a so-called blue copper protein, that contains a Cu-ion as a redox-cofactor. For most of the present experiments zinc azurin is employed in which the Cu has been replaced by Zn. Zn has only one stable oxidation state, Zn^{2+}, so that the fluorescence of the attached label is not affected by redox state changes that might complicate analysis of the experiments. By measuring the fluorescence intensity and lifetime of single dye-labeled ZnAz molecules, the effects of excitation enhancement and fluorescence quenching have been established.

To study the effect of the redox state on the fluorescence intensity and lifetime CuAz has been employed. The Cu in the azurin may occur in the Cu^{+} or Cu^{2+} oxidation state. In the latter state the protein is dark blue due to a strong absorption around 625 nm whereas in the former state it is colourless. As the 625 nm absorption may give rise to Förster resonant energy transfer (FRET) from an attached dye label to the Cu, a switch in the redox state of azurin may lead to a change in fluorescence intensity of the dye. (It should be noted that the Cu centre itself is non-luminescent.) In the present study the redox state of azurin was monitored through fluorescence detection. Attachment of the protein to an 1.4 nm nanoparticle resulted in an enhanced S/N ratio. This shows that the application of nanoparticles can be used for single-molecule redox-state sensing and may offer a viable route to optically detected single-protein electrochemistry [39-47].

2. Experimental methods

Protein labeling. Azurin N42C was obtained and purified according to literature methods [39, 48]. For dye labeling the NHS-ester of Atto-647N (ATTO-TEC GmbH, Germany) was coupled to the N-terminus of either copper or zinc azurin (N42C) according to the manufacturer's instructions. Unbound label was removed using centri-spin 10 size-exclusion chromatography spin columns with a 5-kDa cut-off (Princeton Separations;

Adelphia, NJ, USA). The degree of labeling usually amounted to around 16%. Labeled protein was diluted with 20 mM Hepes buffer, pH 7.0, with final concentrations determined by UV-vis spectroscopy.

Sample preparation. The samples for fluorescence and photothermal imaging were prepared by spin coating a solution of citric-acid coated gold nanoparticles (BB International, UK; NP sizes of 10, 20, 40 or 80 nm) onto glass cover slips modified with 3-aminopropyltrimethoxysilane (APTS). The dilution and spinning speed were chosen such that the spheres were uniformly distributed over the surface (*vide infra*)[49-51]. Then 200 µL of a 50 pM of labeled Atto647N-azurin solution was applied on the coated slide and left at 4°C for 12 h. This was sufficient for obtaining strong adsorption of Az on the NPs. The slides were then washed multiple times with Hepes buffer (20mM, pH 7). The resulting azurin-gold nanoparticle constructs (Az-AuNPs) on coated glass slides were used for fluorescence measurements (see Figure 1).

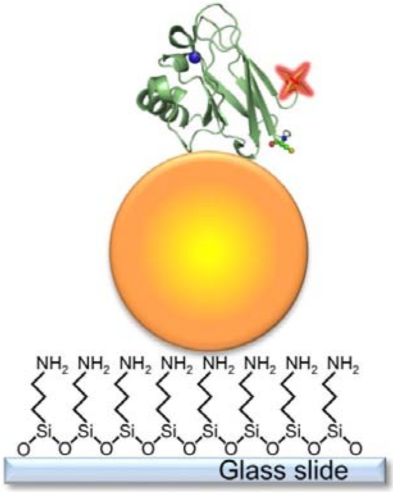

Figure 1: A schematic representation of Atto647N-labeled azurin adsorbed to AuNPs on a glass slide modified with APTS. The protein framework is depicted in green, the Cu atom in blue and the dye label in red.

For the immobilization of the azurin on 1.4 nm AuNPs a slightly different procedure was followed. The AuNPs were commercially obtained as mono-sulfo-NHS–nanogold conjugates and labeling of the azurin with these particles was performed in Hepes buffer (20 mM, pH 7) following the manufacturers protocol (Nanoprobes, USA). Subsequently, a 100 pM solution of the Az-AuNP conjugate was incubated overnight on APTS-modified glass slides at 4^{o}C. The slides were subsequently washed multiple times. Measurements were performed in the same 20 mM Hepes buffer.

Control measurements were performed on azurin immobilized on *glass* and on sputtered *gold films*. *Glass slides* were cleaned by sonication in acetone, rinsed in distilled water, sonicated in aqua regia, rinsed again with water, and stored in methanol. Right before use they were dried in a stream of air and cleaned in an ozone cleaner. ATTO 647N-labeled N42C azurin was immobilized on a cleaned glass slide in high purity agarose IV (Sigma) with a gel point of 36 ± 1.5 °C. The agarose (1 %) was melted in 20 mm HEPES pH 7.0 and cooled to 50 °C. N42C azurin was added to give a final labeled protein concentration of 0.3 nM. 20 µl of azurin-containing agarose was spin-coated onto a cleaned glass slide at 2000 rpm for 10 sec yielding a thin layer of gel. The coated glass was rapidly put into a holder and covered with 1ml of 20 mm HEPES pH 7.0.

For the preparation of the 50 nm *Au films*, first a 1 nm thick adhesion layer of molybdenum-germanium (MoGe) was prepared by depositing MoGe onto a freshly cleaned glass slide through magnetron sputtering using an ATC 1800-F system (AJA corporation) at a deposition rate of 1.32 nm/min (10 mTorr Argon environment). Subsequently, gold was sputtered at a deposition rate of 9.06 nm/min (10 mTorr environment composed of a mixture of argon and 1% oxygen) on top of the MoGe film. The Au films were used immediately after preparation. Azurin (200 pM solution in 20 mM Hepes, pH 7) was immobilized directly on the bare Au films by aspecific absorption. After incubation for a few minutes, unbound azurin was washed off with buffer solution (20 mM HEPES pH 7) and the slides were used directly for measurements.

Absorption spectroscopy. Absorption spectra were measured on a Perkin-Elmer Instruments Lambda 800 spectrophotometer with a spectral bandwidth of 2 nm.

Confocal microscopy. Single-molecule fluorescence studies were performed with a home-built scanning confocal microscope equipped with Time-Correlated Single-Photon Counting (TCSPC) capabilities. For fluorescence excitation the output of a 40 MHz pulsed picosecond diode laser (PDL 800-B, PicoQuant GmbH, output wavelength: 639 nm) was sent through a narrow band clean-up filter (LD01-640/8-25, Semrock, USA), coupled into a single-mode fiber, reflected by a dichroic mirror (Z 532/633 M, Chroma technology, USA) to a high numerical aperture oil objective (100× oil, NA 1.4, Zeiss, Germany) and focused to a diffraction-limited spot (~300 nm) on the sample surface. The power density at the sample was 0.5-1 kW/cm^2. Epi-fluorescence from the labeled azurin was filtered with a band filter (D 675/50 M, Chroma technology, USA) and focused with a +45 mm focal length achromatic lens on the active area of a single photon avalanche photodiode (Perkin-Elmer SPCM-AQR-14). The data acquisition was done by the TimeHarp 200 TCSPC PC-board operating in the special Time-Tagged Time-Resolved (T3R) mode, which stores each individual photon event without on-line data reduction [52]. Samples were mounted onto a P-517 nanopositioner (Physik Instrumente, GmbH) which was driven by an E-710 PZT controller (Physik Instrumente, GmbH). Scanning, accurate positioning, data collection and analysis were performed with the help of Picoquant SymPhoTime software (PicoQuant GmbH).

Fluorescence lifetime images were obtained by scanning a 15x15 µm^2 area of the sample with a step size of 100 nm and a dwell time of 3 ms per pixel. To accurately determine the fluorescence lifetimes of immobilized labeled Cu-azurin in the reduced and in the oxidized state, photon decay histograms of the photons collected over the whole image were constructed. Lifetimes for individual particles were obtained from the photon decay histograms recorded by placing the laser excitation spot on the individual particles. Deconvolution with the instrumental response function (IRF) and a fit to a bi-exponential decay was carried out by using the SymPhoTime software.

Photothermal imaging setup. A photothermal imaging setup was used as described earlier in detail [53]. Briefly, it was based on an inverted microscope (Olympus IX71) which was equipped with an oil immersion objective (60x, NA = 1.45, Olympus,). The heating beam was provided by an Ar-ion laser (Coherent) at 514 nm. The heating light passed an acousto-optical modulator (AOM) which also sent a reference signal to a lock-in detector (SR844, Stanford Research Systems). The probe beam at 790 nm was provided by a Ti:sapphire laser (3900S, Spectra Physics, pumped by 90% of the power of the Ar-ion laser). Both beams were expanded to diameters of about 20 mm to overfill the entrance pupil of the microscope objective (approximately 10 mm), and were combined on a dichroic mirror (BS 669, AHF).

The back/scattered probe light returned from the sample, passed the dichroic mirror, and was directed by a 50/50 beam splitter (Halle) towards a clean-up interference filter (Omega) and a Si photodiode (DHPCA-100-F, Femto). Optionally the probe beam was monitored by a CCD camera (Ganz).

The photodiode provided the signal for demodulation of the photothermal response with the lock-in amplifier, while the sample was scanned with a 3-axis piezostage (MARS, Physik Instrumente). Data acquisition and processing were controlled by an acquisition card (ADWin Gold) linked to a computer.

3. Results

3.1 Optical characterization of Az-AuNPs in solution.

The bulk solution optical properties of the Au colloids were recorded prior to use in the single-molecule study. Figure 2 presents the absorption spectra, which exhibit the characteristic surface plasmon peaks of the AuNPs. The excitation maxima undergo a red shift from 519 to 540 nm as the particle diameter increases from 10 to 80 nm, illustrating the wavelength dependence of the surface plasmon resonance (SPR) on particle size [54]. The peak widths are also observed to increase with particle diameter.

The influence of Az binding on the absorption spectrum of a AuNP solution is shown in Figure 3 for several concentrations (0, 5µM, 10 µM and 50 µM) of CuAz in a buffered (20 mM HEPES pH 7) solution of 80 nm AuNPs. The absorption spectrum of Cu azurin [55] shows two main peaks at 280 nm and 628 nm. The latter peak only appears in the oxidized form [55]. The spectra in Figure 3 are dominated by the AuNP SPR absorption, with a small contribution around 625 nm from azurin (the spectra were not corrected for free azurin present in solution), as the extinction coefficient of the AuNP (around 10^8 - 10^{11} M^{-1} cm^{-1} depending on particle size [16, 54]) is much higher than that of Az (5700 $M^{-1}cm^{-1}$ at 625 nm) [55]. The red shift and the width of the SPR band increase as the Az concentration increases

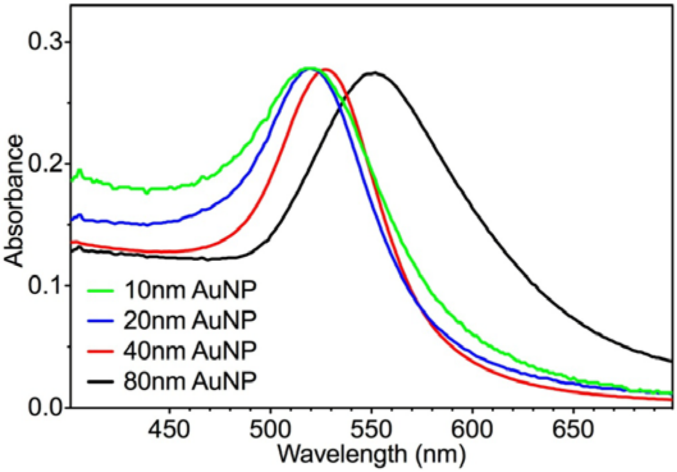

Figure 2: Absorption spectra of four sizes of Au nanoparticles in solution normalized at the peak height in the 500-600 nm region. The solutions were prepared as 1:1 dilutions from the solutions obtained from the manufacturer. Spectra taken in Millipore water at ambient temperature. Particle sizes (as indicated by the colors in the graph): 10, 20, 40 and 80 nm. Spectra are normalized with respect to their absorption maxima. Absorbance in arbitrary units.

(Figure 3, inset) corresponding to an increase in the amount of surface immobilized Az. This suggests that a single AuNP can bind several Az molecules, in line with the facile binding between Az and AuNPs observed previously [51]. The shift is ascribed to the protein-induced change in local dielectric environment of the AuNPs [56-58]. The largest shift amounts to about 5 nm at the highest Az concentration (50 µM)

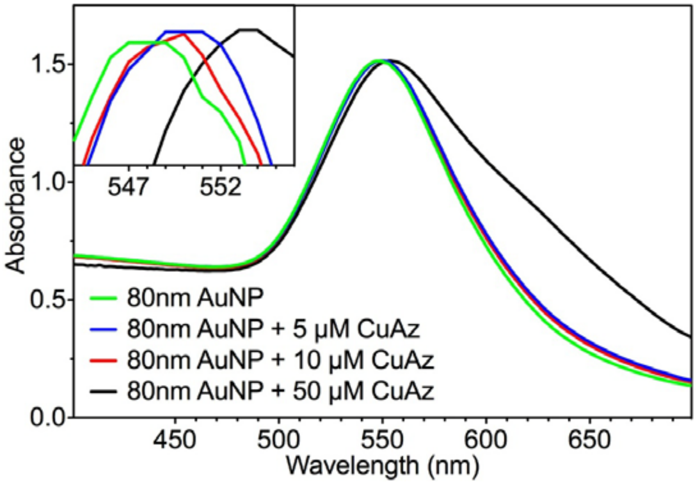

Figure 3: Absorption spectra of a AuNP (80nm diameter) solution (20 mM Hepes, pH 7) in the presence of various amounts of CuAz : 0µM (green), 5µM (blue), 10µM (red) and 50µM (black). The spectra are normalized on the height of the peak around 550 nm. Inset: zoom of the SPR bands showing up to 5nm peak shifts to higher wavelengths with the Az concentration increasing from 5 to 50µM (0, 5, 10 and 50µM). Absorbance in arbitrary units.

The maximum number of Az molecules that can bind to a single AuNP was estimated at 1700 /NP corresponding with a close and uniform Az layer around the NP[‡]. In our case the number of Az molecules in solution is larger than what is needed to form a monolayer on the NP. Thus, because the number of Az bound to the NP still depends on the concentration under excess Az conditions, we conclude that the theoretical maximum is not reached, and

---

[‡] The number of Az molecules that can ultimately bind to a single AuNP depends on the size of the protein and the NP size. The theoretical number of Az molecules that can be packed around a spherical NP, N_{Az}, can be estimated by [50,56]: $N_{Az} = 0.65(R_T^3 - R_{NP}^3) / R_{Az}^3$ [1]

where R_{NP} is the radius of the NP (40 nm), R_{Az} is the azurin radius (2 nm, assuming a quasi-spherical shape [59], and R_T is the radius of the AuNP plus bound Az molecules (R_{NP}+2R_{Az}).

that an equilibrium between free and bound azurin sets in at sub-monolayer coverage of the NP. In the single-molecule studies, we took special care to ensure the binding of only one labeled azurin per NP (*vide infra*).

3.2 Fluorescence images and time traces

Photothermal microscopy was applied to verify that AuNPs were bound as single particles without clustering. Figure 4A shows a photothermal image of a sample with 40 nm diameter gold NPs immobilized on top of an APTS modified glass slide in water. The distribution of photothermal signals is monodisperse and well-offset from the background (Fig. 4B). These results confirm the effectiveness of the protocol used for preparation of samples of single particles bound to the glass surface without clustering, since the photothermal signal is proportional to the absorption-cross section of NPs and thus to the third power of NP diameter. Similar results (not shown) were obtained for 10, 20 and 80 nm diameter AuNPs.

The intrinsic luminescence signal from individual AuNPs occurs at the same wave length as the excitation light while the fluorescence of labeled Az molecules occurs at longer wave lengths. Thus the Az-modified AuNPs can be easily separated from unmodified ones. We also keep the fluorescence excitation power low in our experiments to avoid saturation effects and possible modification of intrinsic fluorescence properties of AuNPs [8].

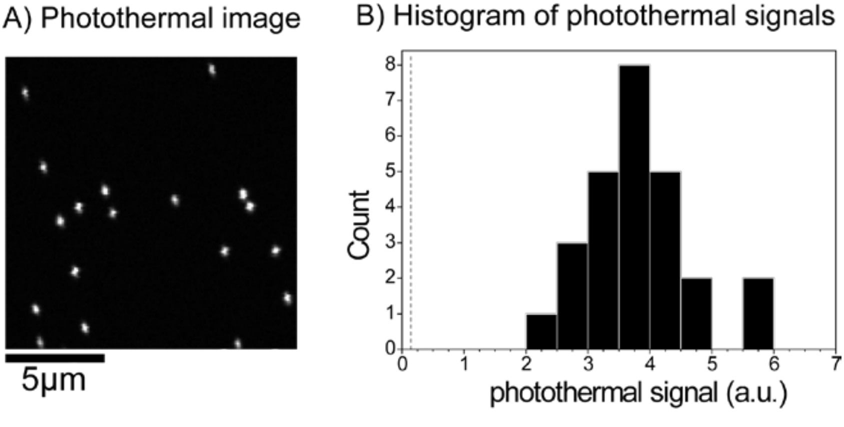

Figure 4. A) (A) Photothermal image of individual 40 nm diameter AuNPs spin-coated on an APTS-modified glass surface. Particles are well-separated from each other. (B) Histogram of photothermal signals from several images obtained at the same experimental conditions. Vertical dashed line indicates signal background level. The monodisperse character of the distribution and its clear off-set from the background is a clear indication for the absence of aggregates.

To investigate the effect of NP size on the fluorescence intensity, confocal images (Figure 5A) were recorded for labeled Zn-Az immobilized on AuNPs ranging in size from 1.4 to 80 nm. Control measurements were performed for Zn-Az immobilized on glass and on flat gold (Figure 5A). Well-separated bright spots derive from single Az molecules. A big variation in peak intensity among the different images is immediately evident from the scale bars (compare f.i. in Figure 5A the panel ‘ZnAz on glass’ (maximum count number of 120) with the panel ‘10 nm AuNP-ZnAz’ (maximum count number of 1415)). Compared to ZnAz on glass the fluorescence emission from Atto-647N-labeled ZnAz increases significantly when the protein is bound to 1.4 nm AuNPs and the intensity keeps increasing with the size of the AuNPs (see Figure 5, panels B and C). By contrast, labeled Zn-Az which is deposited directly onto a 50 nm thick gold film experiences fluorescence *quenching* instead of *enhancement* (see Figure 5). The images show some heterogeneity in the fluorescence intensity, which is ascribed to variation in protein orientation leading to

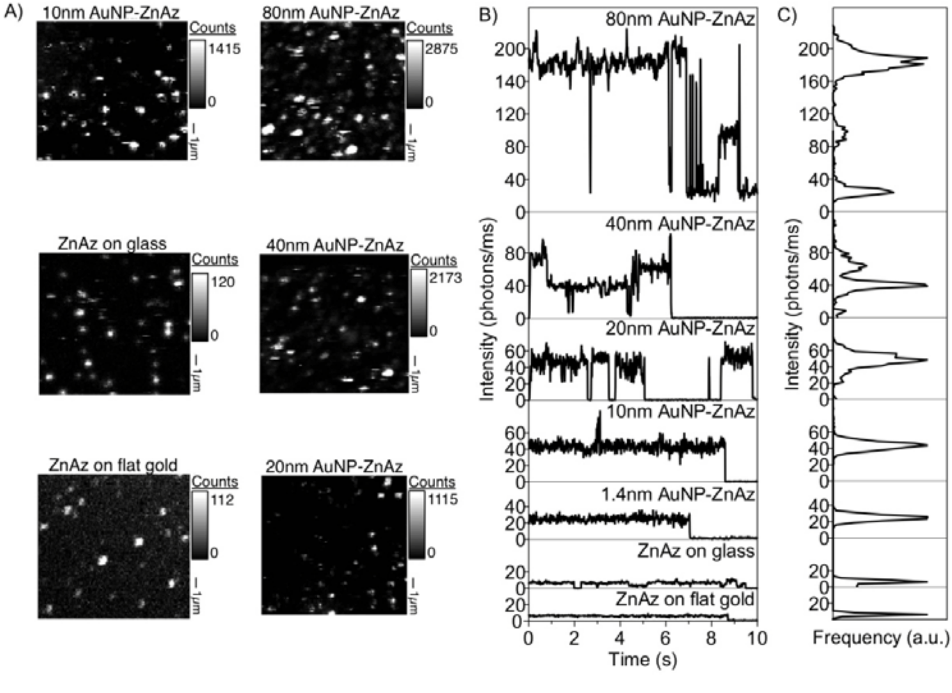

Figure 5: A). Confocal images (15×15 μm, step size 100 nm, dwell time 3 ms/pixel) of labeled Zn-azurin bound to AuNPs, labeled Zn-azurin on flat gold and labeled Zn-azurin on an APTS-modified glass side. Scale bar shows the intensity counts in 3 msec bins. B) Time traces of individual azurin molecules on 50 nm thick flat gold, APTS-modified glass and AuNPs. C) Count rate histograms corresponding to the traces in panel B.

variation in the fluorophore-NP distance and the fluorophore orientation.

Typical intensity time traces of single Az molecules attached to all of the five AuNPs used in this study (1.4, 10, 20, 40, and 80 nm) and of Az molecules on glass and flat Au are presented in Figure 5B. From the observed single-step bleaching in the Az-AuNP fluorescence time traces (Figure 5B, discussed in more detail below), we conclude that at most a single fluorescent azurin is bound per nanoparticle. As already seen in Figure 5A, compared to Az immobilized on a glass surface the fluorescence intensities increase significantly with AuNP size, from a 3-fold enhancement for the 1.4 nm AuNPs up to 29-fold for Az bound to an 80 nm AuNP. The enhancement factors have been collected in Table 1, 2nd column (vide infra).

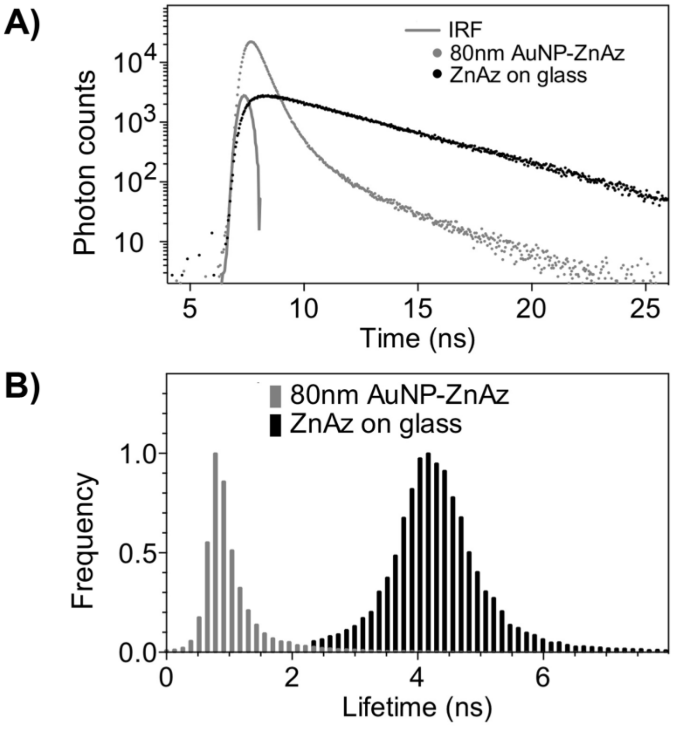

Figure 6: A). Typical TCSPC decay curves of single Zn azurin molecules on an APTS-modified glass slide (black dots) and on an AuNP of 80nm diameter (light gray dots). The light gray line shows the instrument response function (IRF). B). Normalized histograms of lifetimes of single azurin molecules (data taken from over 150 molecules) on glass (black) and AuNP 80 nm diameter (light gray).

3.3 Lifetime measurements and fluorescence enhancement

To provide further insight into the fluorophore-nanoparticle interaction fluorescence lifetime studies were carried out on the conjugate Az-AuNPs. As an example the fluorescence intensity decay of labeled Zn-Az attached to an 80 nm AuNP is shown in Figure 6A. A bi-exponential decay model with a main component (amplitude = 0.96) and a lifetime τ = 0.85 ns, and a minor component with τ = 2.4 ns describes well the experimental decay histograms. Figure 6B shows histograms of the lifetimes estimated from fluorescence decays of more than 150 individual molecules.

The fluorescence lifetime distributions of Zn-Az are plotted for all NP sizes in Figure 7 together with the flat-gold and glass distributions. A dramatic decrease in the lifetime with increasing particle size is observed, with the lifetime changing from 3.5 to 0.85 ns for NP sizes going up from 1.4 to 80 nm (see also Table 1, 3rd column). Some of the lifetime distributions are somewhat asymmetric with a tail towards longer lifetimes. For the NPs we ascribe this to variation in fluorophore-NP distance and orientation. The long-lifetime tail which is noticeable in the Az-on-glass distribution is attributed to the background, which is relatively strong for the non-enhanced signal of Az on glass.

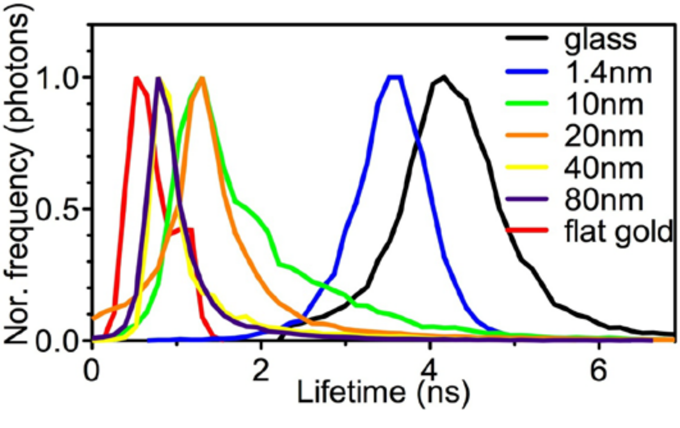

Figure 7: Lifetime histograms of Atto647N-labeled single Zn-azurin molecules immobilized on a glass surface, on a 50 nm thick flat gold film and on AuNPs of varying size (1.4, 10, 20, 40 and 80 nm).

3.4 Single-molecule redox state detection

We checked whether the FRET-based fluorescence detection method [39, 40] can be applied to the observation of the redox state changes of single Cu-Az molecules bound to AuNPs. Oxidizing ($K_3 [Fe (CN)_6]$) and reducing (sodium ascorbate) reagents were used to change the redox state of the protein. Time traces and TCSPC decay curves of Atto647N-labeled Cu-Az bound to 1.4 nm AuNPs are shown in Figures 8A and B, respectively. The ratio between reduced (Figure 8A, top trace) and oxidized (Figure 8A, bottom trace) intensities is about 4. The excited state lifetimes are 3.5 ns and 1.4 ns for reduced and oxidized azurin, respectively. As expected, the reduced Az lifetime is the same as for the redox-inactive Zn-Az bound to this NP. The decay of oxidized Az had to be fitted to a bi-exponential model,

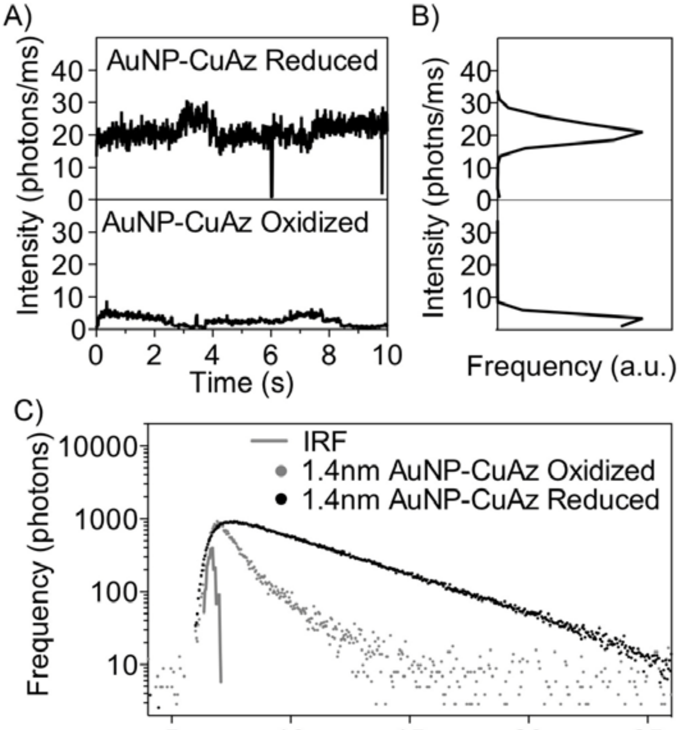

Figure 8: A) Time traces, B) intensity histograms and C) TCSPC decay curves of individual A647N-labeled Az (Cu-Az) proteins bound to 1.4 nm AuNP in reduced and oxidized states. Best fits for the decay curves were 3.5 ns for the reduced form and 1.4 ns for the oxidized form. The TCSPC curve of the instrument response function (IRF) is also included (panel C light gray line).

with 1.4 ns the dominant lifetime and a relative amplitude of more than 90%. The second component had a lifetime of 0.5 ns and an amplitude of less than 10%, and was attributed to the background. Thus, the redox activity can be measured down to single molecule level. Attachment to the AuNP is responsible for enhanced fluorescence and, thereby, for enhanced sensitivity.

We find the intensity-based switching ratio, Q_I, to be 0.75 with

$$Q_I = 1 - (F_{oxid} / F_{red}) . \qquad [2]$$

Here, F_{oxid} and F_{red} denote the fluorescence intensity of the Az in the reduced and oxidized form, respectively [40]. The lifetime-based switching ratio [60] is given by Q_L with:

$$Q_L = 1 - (\tau_{oxid} / \tau_{red}) . \qquad [3]$$

Here, τ_{oxid} and τ_{red} denote the fluorescence lifetime of the Az in the reduced and oxidized form, respectively. Q_L is found to be around 0.6, slightly lower than the intensity-based value. A much more pronounced discrepancy between Q_I and Q_L was found for Atto655-labeled Az immobilized on gold films [61] with $Q_I = 0.7$ and $Q_L = 0.4$. This discrepancy may be due to dye-specific photophysics and is currently subject of further investigation.

4. Discussion

From the results presented above, it is clear that immobilization of a dye-labeled protein onto a nanoparticle may have a pronounced effect on the fluorescence of the protein-dye construct. Enhancement of the emission intensity and shortening of the fluorescence lifetime occur simultaneously, and both effects increase monotonously with increasing NP size. The combination of intensity enhancement and lifetime shortening has been demonstrated previously for fluorophore-nanoparticle combinations [1, 3, 4, 6, 12, 20, 62] and for fluorophores immobilized on several types of metal film[13, 61, 63-65].

It is of interest to compare our observations to these reports in more detail. Enhancement factors ranging from 8 to 13 have been reported for single dye molecules close to 80 nm and 100 nm AuNPs [3, 4, 12, 20]. In the present case we see an enhancement by a factor of 29 for 80 nm AuNPs. Several factors may account for this difference: firstly, previous values were taken from confocal images rather than time traces. Values from images will be an average over bright and dark phases if blinking is present, whereas in our experiments only the bright phases were taken into account. Secondly, the enhancement is strongly dye-dependent and in previous studies other dyes were used than the one employed in the present study [66]. Thirdly, the fluorophore-metal interaction may also be enhanced by the dielectric medium. It was shown by Härtling et al. [5] that a medium with an intermediate refractive index such as water, will result in a larger enhancement than when air or a higher-refractive index medium such as immersion oil, is used. Water is the medium used in our experiments, whereas in most previous single-molecule studies [3, 4, 12, 20] the medium was a spin-coated film of PMMA or para-terphenyl, both with a rather higher refractive index than water. There is a report by Fu et al. [6] in which water is used with NP-dye constructs in solution, showing an intensity enhancement factor of 15, but the dye-NP distance is rather longer than ours and silver NPs are used, so that the results are not directly comparable.

Results of lifetime measurements can be compared to a few literature reports. Kühn et al. [3] observe a 20-fold lifetime reduction together with a 13-fold intensity enhancement for a terrylene dye at 2 nm distance of a 100 nm AuNP. Fu et al. [6] report a 15-fold enhancement of Cy5 fluorescence for a distance of 8 nm between the dye and a 50 nm AgNP; the Cy5 lifetime is shortened from 2.3 to 0.43 ns. A similar result is obtained by Fu and Lakowicz for Cy5 on silver island films [65]. These three studies thus show similar combinations of intensity enhancement and lifetime shortening as we report. For SAMSA, a fluorescein derived dye, on 5 to 20 nm size AuNPs, a reduction in both intensity and lifetime (compared to the free-dye case) is observed by Cannone et al. [2], presumably because of the small size of the NPs. Most measurements of lifetime shortening were carried out on ensembles of fluorophores, which, moreover, were mostly immobilized on silver and gold island films or particle films [31, 62-64, 67]. Hence, these results are not fully comparable to ours. Although combinations of intensity enhancement and lifetime shortening were reported similar to the results of the present study, the absolute values are less unequivocal as the data may have been averaged over a heterogeneous population while also concentration differences between experiments cannot be excluded.

A more quantitative analysis of our data is based on previously developed theoretical models of fluorophore-metal interactions [12, 20, 21, 33-36]. The fluorescence rate (γ_{em}) of a single molecule can be expressed as [12, 20]:

$$\gamma_{em} = \gamma_{exc} q \qquad [4]$$

with γ_{exc} and q the excitation rate and quantum yield respectively. For a free molecule in solution the quantum yield is denoted as q_0, which takes the form

$$q_0 = \frac{\gamma_{r,0}}{\gamma_{r,0} + \gamma_{nr.0}} = \gamma_{r,0}\tau_0 \qquad [5]$$

with $\gamma_{r,0}$ and $\gamma_{nr,0}$ the (free-space) radiative and nonradiative decay rate, respectively, and τ_0 is the fluorescence lifetime of the free molecule. The presence of metal particles will lead to a change in the quantum yield in two ways. The radiative decay may be enhanced by coupling of the excited state dipole into the locally modified electromagnetic field, and the nonradiative decay may increase due to quenching by energy transfer from the fluorophore to the metal. In the expression for the quantum yield this is incorporated by taking γ_r to be variable, and by introducing an additional quenching ('energy absorption') rate γ_{abs}; the nonradiative decay rate γ_{nr} is taken to be intrinsic, *i.e.*, $\gamma_{nr} = \gamma_{nr,0}$ [4, 12, 31]. This gives:

$$q = \frac{\gamma_r}{\gamma_r + \gamma_{nr.0} + \gamma_{abs}} = \gamma_r \tau \qquad [6]$$

The lifetime of a fluorophore-metal system is also modified by the change in γ_r and the additional decay rate, γ_{abs}, and is given by

$$\tau = (\gamma_r + \gamma_{nr,0} + \gamma_{abs})^{-1} \qquad [7]$$

If the enhancement of the radiative rate dominates over the quenching effect, the quantum yield may increase in the vicinity of a metal NP. The largest attainable value of q is 1 [3-5, 12, 20, 21, 66].

More commonly, it is assumed that γ_{exc} is strongly enhanced in the vicinity of a NP. For weak excitation (below saturation) which is applicable here, the excitation rate is proportional to $|\mathbf{E} \cdot \mathbf{p}|^2$, with $\boldsymbol{E}$ the local electric field and $\boldsymbol{p}$ the transition dipole moment [5, 12, 20]. Therefore, the highly enhanced local electromagnetic field near a AuNP can effectively increase the excitation rate. The net enhancement is, therefore, a composite result of excitation enhancement, radiative rate enhancement and increased quenching. All of these terms depend on the metal particle properties and on the distance between the fluorophore and the NPs. In the sub-5 nm regime of Az-NP distances, the radiative rate enhancement is usually calculated to be small compared to the other two effects [12, 20].

From our data we can estimate the magnitude of the three effects using fluorescence intensity and lifetime information (Table 1). Taking the results on the glass surface to correspond to the free molecule quantities $\gamma_{em,0}$, $\gamma_{exc,0}$ and q_0, we obtain [20]:

$$\frac{\gamma_{em}}{\gamma_{em,0}} = \frac{\gamma_{exc}}{\gamma_{exc,0}} \frac{q}{q_0} \qquad [8]$$

We calculate $\gamma_{exc}/\gamma_{exc,0}$ for two limiting cases. In the *'quenching limit'*, we assume the radiative rate change is negligible. This implies that the change in quantum yield is proportional to the change in lifetime:

$$\frac{q}{q_0} = \frac{\tau}{\tau_0} \qquad [9]$$

which gives

$$\frac{\gamma_{exc}}{\gamma_{exc,0}} = \frac{\gamma_{em}}{\gamma_{em,0}} \frac{\tau}{\tau_0} \qquad [10]$$

with the enhancement of γ_{em} equal to the increase in intensity observed in the fluorescence time traces (Figure 6B). The resulting values for the excitation enhancement ($\gamma_{exc}/\gamma_{exc,0}$) are listed in column 4 of Table 1. It is seen that γ_{exc} increases with nanoparticle size up to 145-

Substrate	$\gamma_{em} / \gamma_{em,0}$ [b]	τ (ns) [c]	$\gamma_{exc} / \gamma_{exc,0}$ [d]	$\gamma_{exc} / \gamma_{exc,0}$ [e]
Glass	1	4.2	1	1
1.4 [a]	3	3.50 (1.45)	4	2.0
10 [a]	6	1.60 (0.95)	16	4
20 [a]	7	1.55 (0.93)	19	4.6
40 [a]	11	0.85 (0.62)	55	7.2
80 [a]	29	0.85 (0.62)	145	19
Au film [f]	0.7	0.65	7	0.4

Table 1: Fluorescence enhancement values and lifetimes for labeled Zn-azurin and Cu-azurin bound to AuNPs with different sizes. All data pertain to Zn-azurin except the data in parentheses in column three, which refer to oxidized Cu-azurin. Calculations for Zn-azurin are based on equations [8]-[10].

a) Diameter of Au NP, nm.

b) Observed fluorescence rate γ_{em} (Eq. [4]) normalized to the rate measured for Atto647N-labeled ZnAz on glass in the absence of NPs. Fluorescence rates are taken from the peak value of the count rate histograms of the intensity time traces (Fig. 5B). Note that these values reflect only the bright parts of the traces, i.e. the effect of blinking is not included.

c) Fluorescence lifetime, as obtained from TCSPC decay curves (Figs 6 and 7). The data in parentheses refer to oxidized Cu-azurin. See text for further details on the Cu-azurin data.

d) Calculated excitation rate γ_{exc} (using Eq. 10]) normalized to the rate for Az on glass, assuming that the radiative rate γ_r is not affected by the NP, i.e., $\gamma_r = \gamma_{r,0}$ (see text for details). The lifetime τ_0 of Atto-647N-labeled Az on glass is 4.2 ns.

e) Excitation rate γ_{exc} as in c, but now under the assumption that the radiative rate is increased and the quantum yield increases from 0.65 ($=q_0$) to 1($=q$) (see Eq. [8] and text for details).

f) Labeled Zn-azurin immobilized on a bare, 50 nm thick Au film fold for the 80 nm NP.

The second limiting case, which we refer to as the '*radiative limit*', is based on the assumption that the radiative rate increase is large and that the lifetime shortening should be fully ascribed to radiative enhancement [31, 36, 63]. In our calculation we use this limit to the extent that q is taken to be ≤ 1. With q_0 equal to 0.65 for Atto647N (value provided by the manufacturer) and $q = 1$, we calculate the excitation rate enhancements from Equation [8] as shown in column 5 of Table 1. Again, we see an increase of the excitation enhancement with NP size, with a maximum of 19 for the 80 nm NP.

A value of 25 for the enhancement of γ_{exc} was calculated by Kühn et al. [3] for a 100 nm nanoparticle, which seems to suggest that the value of 19 found in the radiative limit is more realistic than the factor of 145 calculated above for the quenching limit. However, the relative importance of the factors found by Kühn et al. corresponds more to the 'quenching limit', as they unequivocally show that the net enhancement (*i.e.*, the increase in γ_{em}, for which they find a factor 13) is *lower* than the excitation rate (γ_{exc}) enhancement in their case (in the radiative limit, the opposite obtains with the net enhancement of 29 in our case being *higher* than the factor of 19 for γ_{exc}) and that quenching cannot be neglected. We believe this - *i.e.*, the presence of both significant quenching and excitation enhancement - to be applicable to our fluorophore-NP system as well, and expect the real values for the excitation enhancement to lie in between the two limits and above the enhancement factor for γ_{em}. Full-scale modeling of the three components is required to shed more light on this issue.

As shown above, the net enhancement of fluorescence intensity increases with nanoparticle size. Such a size effect was previously predicted [4, 5, 68]. Anger et al. [4] calculate a factor of 5 difference in the γ_{em} values of Nile blue dye molecules close to 20 and to 80 nm AuNPs, and Härtling et al. [5] calculate the effect for 30 nm and 80 nm AuNPs and find a difference of about a factor 6 between these two sizes, for configurations comparable to ours, at ~5 nm distance between dye and NP. These differences are close to the factor of 4 we see between the γ_{em} enhancements induced by 20 nm and 80 nm NPs. The *absolute* values predicted by these authors for the γ_{em} enhancements, on the other hand, are rather lower than what we observe. The 20 resp. 30 nm NPs are predicted to produce a net change of fluorescence intensity by a factor of 0.3 [4] and 0.2, respectively [5], (*i.e.*, a *decrease* in intensity) in marked contrast to the 7-fold intensity enhancement we observe for 20 nm NPs. Thus, the experimental verification provided by our study may be of help in refining the theoretical predictions.

Furthermore, we find that in the same fluorophore-metal distance regime (up to 4 nm) the fluorescence enhancement is dominant when Az is coupled to AuNPs, whereas the fluorescence of Az is quenched when it is adsorbed on a gold film (Figure 6A, bottom right). In the latter case, the interaction will be dominated by quenching, as there are more states available to which energy transfer can take place. At the same time, for gold films the roughness of the surface also has a large effect on the net intensity change [61, 62, 67, 69-73], with more enhancement for rougher films (i.e. with larger, more nanoparticle-like surface structures).

With the strong size dependence of both enhancement and quenching, it is of interest to see how far we can take the redox state detection in the vicinity of gold NPs. So far, we have measured redox switching for CuAz attached to a 1.4 nm NP only (see Figure 8). For this NP size, reduced and oxidized CuAz lifetimes are 3.5 ns and 1.4 ns respectively. We can analyze the data further by looking into the contribution of the FRET mechanism to the lifetime shortening in the Cu(II)Az form. For the reduced form it was stated (see Eq. 7) that $\tau_{red} = \left(\gamma_r + \gamma_{nr} + \gamma_{abs}\right)^{-1}$. For the oxidized form the expression for the lifetime becomes $\tau_{ox} = \left(\gamma_r + \gamma_{nr} + \gamma_{abs} + \gamma_{FRET}\right)^{-1}$ in which γ_{FRET} is the rate of energy transfer from the label to the Cu as a result of FRET. With τ_{red} = 3.5 ns and τ_{ox} = 1.4 ns one finds $1/\gamma_{FRET}$ = 2.33 ns. It may be assumed safely that γ_{FRET} is independent of AuNP size (the FRET phenomenon in our case is an intramolecular effect between Cu and label and has nothing to do with the label-NP interaction) and that the fluorescence lifetimes of Cu(I)Az and ZnAz (there is no FRET between label and metal in both cases) are the same it is easy to calculate τ_{ox} for the other AuNP sizes. The data are collected in Table 1, 3rd column (numbers in parentheses).

The numbers in Table 1 show that as the nanoparticle size increases the difference between τ_{red} and τ_{ox} becomes progressively smaller and more difficult to detect, therefore. This is because the increase in radiative rate makes the life times less sensitive to differences in the non-radiative rates[74]. However, the smaller difference in life times is more than compensated by the concomitant increase in fluorescence intensity which allows for higher signal to noise ratios. The net effect is a slight increase in sensitivity for detecting redox changes at the single molecule level with increasing NP size. Larger NPs, however, allow for multiple attachment of labeled protein molecules which would result in greatly enhanced sensitivity for detecting environmental changes in redox potential.

Further improvements may be obtained by applying specific immobilization strategies which give more control over the dye-AuNP distance and orientation. Changes in orientations and distances may affect the quenching and enhancement terms differently, so that obtaining an even larger intensity enhancement without a further increase in quenching may be feasible. Even more promising might be the application of nanorods instead of spherical AuNPs (‘lightning effect’)[75, 76]. For electrochemical applications, the distance between redox center and metal should be within 1 or 2 nm to ensure sufficient electronic coupling between protein and electrode. Investigations into the electrochemical control of an Az-AuNP system are currently underway.

5. Conclusion

We have shown that the fluorescence of dye-labeled azurin can be enhanced by attaching the protein to a gold nanoparticle. This study demonstrates for the first time the theoretically predicted NP size dependence of fluorophore-NP interaction. In addition, the observed enhancement factors, of up to 29 times increase in intensity for Az on 80 nm AuNPs, are a huge improvement compared to previous observations. By controlling the distance and the orientation of the protein on the AuNP through a covalent link, the fluorescence enhancement may yet be further improved.

In the used AuNP-labeled protein system, the detection of the protein redox state with enhanced fluorescence intensity was shown to be feasible. The system can be easily prepared and applied to various redox proteins and biomolecules, offering new possibilities of single-molecule redox state detection as well as of high-throughput analysis.

References

1. Dulkeith E, Morteani AC, Niedereichholz T, Klar TA, Feldmann J, Levi SA, van Veggel FCJM, Reinhoudt DN, Moller M, Gittins DI. Fluorescence quenching of dye molecules near gold nanoparticles: Radiative and nonradiative effects. *Physical Review Letters* 2002; **89**(20).
2. Cannone F, Chirico G, Bizzarri AR, Cannistraro S. Quenching and blinking of fluorescence of a single dye molecule bound to gold nanoparticles. *Journal of Physical Chemistry B* 2006; **110**(33):16491-16498.
3. Kuhn S, Hakanson U, Rogobete L, Sandoghdar V. Enhancement of single-molecule fluorescence using a gold nanoparticle as an optical nanoantenna. *Physical Review Letters* 2006; **97**(1).
4. Anger P, Bharadwaj P, Novotny L. Enhancement and quenching of single-molecule fluorescence. *Physical Review Letters* 2006; **96**(11).
5. Hartling T, Reichenbach P, Eng LM. Near-field coupling of a single fluorescent molecule and a spherical gold nanoparticle. *Optics Express* 2007; **15**(20):12806-12817.

6 Fu Y, Zhang J, Lakowicz JR. Plasmonic enhancement of single-molecule fluorescence near a silver nanoparticle. *Journal of Fluorescence* 2007; **17**(6):811-816.

7. Gaiduk A, Yorulmaz M, Orrit M. Correlated Absorption and Photoluminescence of Single Gold Nanoparticles. *Chemphyschem* 2011; **12**(8):1536-1541.

8 Gaiduk A, Ruijgrok PV, Yorulmaz M, Orrit M. Making gold nanoparticles fluorescent for simultaneous absorption and fluorescence detection on the single particle level. *Physical Chemistry Chemical Physics* 2011; **13**(1):149-153.

9. Yun CS, Javier A, Jennings T, Fisher M, Hira S, Peterson S, Hopkins B, Reich NO, Strouse GF. Nanometal surface energy transfer in optical rulers, breaking the FRET barrier. *Journal of the American Chemical Society* 2005; **127**(9):3115-3119.

10. Chhabra R, Sharma J, Wang HN, Zou SL, Lin S, Yan H, Lindsay S, Liu Y. Distance-dependent interactions between gold nanoparticles and fluorescent molecules with DNA as tunable spacers. *Nanotechnology* 2009; **20**(48).

11. Taminiau TH, Stefani FD, Segerink FB, Van Hulst NF. Optical antennas direct single-molecule emission. *Nature Photonics* 2008; **2**(4):234-237.

12. Bharadwaj P, Anger P, Novotny L. Nanoplasmonic enhancement of single-molecule fluorescence. *Nanotechnology* 2007; **18**(4).

13. Fu Y, Lakowicz JR. Modification of single molecule fluorescence near metallic nanostructures. *Laser & Photonics Reviews* 2009; **3**(1-2):221-232.

14. Fort E, Gresillon S. Surface enhanced fluorescence. *Journal of Physics D-Applied Physics* 2008; **41**(1).

15. Lakowicz JR. Plasmonics in biology and plasmon-controlled fluorescence. *Plasmonics* 2006; **1**(1):5-33.

16. Liu XO, Atwater M, Wang JH, Huo Q. Extinction coefficient of gold nanoparticles with different sizes and different capping ligands. *Colloids and Surfaces B-Biointerfaces* 2007; **58**(1):3-7.

17. Pelton M, Aizpurua J, Bryant G. Metal-nanoparticle plasmonics. *Laser & Photonics Reviews* 2008; **2**(3):136-159.

18. Barnes WL. Fluorescence near interfaces: the role of photonic mode density. *Journal of Modern Optics* 1998; **45**(4):661-699.

19. Girard C. Near fields in nanostructures. *Reports on Progress in Physics* 2005; **68**(8):1883-1933.

20. Bharadwaj P, Novotny L. Spectral dependence of single molecule fluorescence enhancement. *Optics Express* 2007; **15**(21):14266-14274.

21. Bharadwaj P, Deutsch B, Novotny L. Optical Antennas. Advances in Optics and Photonics. *Optics and Photonics* 2009; **1**:438-483.

22. Anker JN, Hall WP, Lyandres O, Shah NC, Zhao J, Van Duyne RP. Biosensing with plasmonic nanosensors. *Nature Materials* 2008; **7**(6):442-453.

23. Salata OV. Applications of nanoparticles in biology and medicine. *Journal of Nanobiotechnology* 2004; **2**:3-8.

24. Zhang J, Fu Y, Chowdhury MH, Lakowicz JR. Single-molecule studies on fluorescently labeled silver particles: Effects of particle size. *Journal of Physical Chemistry C* 2008; **112**(1):18-26.

25. Sanvicens N, Pastells C, Pascual N, Marco MP. Nanoparticle-based biosensors for detection of pathogenic bacteria. *Trac-Trends in Analytical Chemistry* 2009; **28**(11):1243-1252.

26. Li YY, Schluesener HJ, Xu SQ. Gold nanoparticle-based biosensors. *Gold Bulletin* 2010; **43**(1):29-41.

27. Katz E, Willner I. Integrated nanoparticle-biomolecule hybrid systems: Synthesis, properties, and applications. *Angewandte Chemie-International Edition* 2004; **43**(45):6042-6108.

28. Willner I, Willner B, Katz E. Biomolecule-nanoparticle hybrid systems for bioelectronic applications. *Bioelectrochemistry* 2007; **70**(1):2-11.

29. Zhang J, Fu Y, Chowdhury MH, Lakowicz JR. Enhanced Forster resonance energy transfer on single metal particle. 2. Dependence on donor-acceptor separation distance, particle size, and distance from metal surface. *Journal of Physical Chemistry C* 2007; **111**(32):11784-11792.

30. Lakowicz JR. Radiative decay engineering: Biophysical and biomedical applications. *Analytical Biochemistry* 2001; **298**(1):1-24.

31. Zhang YX, Aslan K, Previte MJR, Geddes CD. Metal-enhanced fluorescence from copper substrates. *Applied Physics Letters* 2007; **90**(17).

32. Waldeck DH, Alivisatos AP, Harris CB. Nonradiative Damping of Molecular Electronic Excited-States by Metal-Surfaces. *Surface Science* 1985; **158**(1-3):103-125.

33. Chance RR, Prock A, Silbey R. Comments on Classical-Theory of Energy-Transfer .2. Extension to Higher Multipoles and Anisotropic Media. *Journal of Chemical Physics* 1976; **65**(7):2527-2531.

34. Chance RR, Prock A, Silbey R. Comments on Classical Theory of Energy-Transfer. *Journal of Chemical Physics* 1975; **62**(6):2245-2253.

35. Chance RR, Prock A, Silbey R. Lifetime of An Emitting Molecule Near A Partially Reflecting Surface. *Journal of Chemical Physics* 1974; **60**(7):2744-2748.

36. Lakowicz JR. Radiative decay engineering 5: metal-enhanced fluorescence and plasmon emission. *Analytical Biochemistry* 2005; **337**(2):171-194.

37. Enderlein J. A theoretical investigation of single-molecule fluorescence detection on thin metallic layers. *Biophysical Journal* 2000; **78**(4):2151-2158.

38. Enderlein J. Theoretical investigation of aspects of single-molecule fluorescence detection in microcapillaries. *Cytometry* 1999; **36**(3):195-199.

39. Kuznetsova S, Zauner G, Schmauder R, Mayboroda OA, Deelder AM, Aartsma TJ, Canters GW. A Forster-resonance-energy transfer-based method for fluorescence detection of the protein redox state. *Analytical Biochemistry* 2006; **350**(1):52-60.

40. Schmauder R, Alagaratnam S, Chan C, Schmidt T, Canters GW, Aartsma TJ. Sensitive detection of the redox state of copper proteins using fluorescence. *Journal of Biological Inorganic Chemistry* 2005; **10**(6):683-687.

41. Schmauder R, Librizzi F, Canters GW, Schmidt T, Aartsma TJ. The oxidation state of a protein observed molecule-by-molecule. *Chemphyschem* 2005; **6**(7):1381-1386.

42. Davis JJ, Burgess H, Zauner G, Kuznetsova S, Salverda J, Aartsma T, Canters GW. Monitoring interfacial bioelectrochemistry using a FRET switch. *Journal of Physical Chemistry B* 2006; **110**(41):20649-20654.

43. Kuznetsova S, Zauner G, Aartsma TJ, Engelkamp H, Hatzakis N, Rowan AE, Nolte RJM, Christianen PCM, Canters GW. The enzyme mechanism of nitrite reductase studied at single-molecule level. *Proceedings of the National Academy of Sciences of the United States of America* 2008; **105**(9):3250-3255.

44. Salverda JM, Patil AV, Mizzon G, Kuznetsova S, Zauner G, Akkilic N, Canters GW, Davis JJ, Heering HA, Aartsma TJ. Fluorescent Cyclic Voltammetry of Immobilized Azurin: Direct Observation of Thermodynamic and Kinetic Heterogeneity. *Angewandte Chemie-International Edition* 2010; **49**(33):5776-5779.

45. Strianese M, Zauner G, Tepper AWJW, Bubacco L, Breukink E, Aartsma TJ, Canters GW, Tabares LC. A protein-based oxygen biosensor for high-throughput monitoring of cell growth and cell viability. *Analytical Biochemistry* 2009; **385**(2):242-248.

46. Zauner G, Strianese M, Bubacco L, Aartsma TJ, Tepper AWJW, Canters GW. Type-3 copper proteins as biocompatible and reusable oxygen sensors. *Inorganica Chimica Acta* 2008; **361**(4):1116-1121.

47. Zauner G, Lonardi E, Bubacco L, Aartsma TJ, Canters GW, Tepper AWJW. Tryptophan-to-dye fluorescence energy transfer applied to oxygen sensing by using type-3 copper proteins. *Chemistry-A European Journal* 2007; **13**(25):7085-7090.

48. Vandekamp M, Hali FC, Rosato N, Agro AF, Canters GW. Purification and Characterization of A Nonreconstitutable Azurin, Obtained by Heterologous Expression of the Pseudomonas-Aeruginosa Azu Gene in Escherichia-Coli. *Biochimica et Biophysica Acta* 1990; **1019**(3):283-292.

49. Freeman RG, Grabar KC, Allison KJ, Bright RM, Davis JA, Guthrie AP, Hommer MB, Jackson MA, Smith PC, Walter DG, Natan MJ. Self-Assembled Metal Colloid Monolayers - An Approach to Sers Substrates. *Science* 1995; **267**(5204):1629-1632.

50. Daniel MC, Astruc D. Gold nanoparticles: Assembly, supramolecular chemistry, quantum-size-related properties, and applications toward biology, catalysis, and nanotechnology. *Chemical Reviews* 2004; **104**(1):293-346.

51. Delfino I, Cannistraro S. Optical investigation of the electron transfer protein azurin-gold nanoparticle system. *Biophysical Chemistry* 2009; **139**(1):1-7.

52. Benda A, Hof M, Wahl M, Patting M, Erdmann R, Kapusta P. TCSPC upgrade of a confocal FCS microscope. *Review of Scientific Instruments* 2005; **76**(3).

53. Gaiduk A, Ruijgrok PV, Yorulmaz M, Orrit M. Detection limits in photothermal microscopy. *Chemical Science* 2010; **1**(3):343-350.

54. Jain PK, Lee KS, El-Sayed IH, El-Sayed MA. Calculated absorption and scattering properties of gold nanoparticles of different size, shape, and composition: Applications in biological imaging and biomedicine. *Journal of Physical Chemistry B* 2006; **110**(14):7238-7248.

55. Kolczak, U., Dennison, C, Messerschmidt, A., and Canters, G. W. Azurin and azurin mutants. Messerschmidt, A., Huber, R., Poulos, T., and Wieghardt, K. 1170-1194. 2001. John Wiley & Sons. Handbook of Metalloproteins.

56. Pompa PP, Chiuri R, Manna L, Pellegrino T, del Mercato LL, Parak WJ, Calabi F, Cingolani R, Rinaldi R. Fluorescence resonance energy transfer induced by conjugation of metalloproteins to nanoparticles. *Chemical Physics Letters* 2006; **417**(4-6):351-357.

57. Pastoriza-Santos I, Gomez D, Perez-Juste J, Liz-Marzan LM, Mulvaney P. Optical properties of metal nanoparticle coated silica spheres: a simple effective medium approach. *Physical Chemistry Chemical Physics* 2004; **6**(21):5056-5060.

58. Lunt EAM, Pitter MC, O'Shea P. Quantitative Studies of the Interactions of Metalloproteins with Gold Nanoparticles: Identification of Dominant Properties of the Protein that Underlies the Spectral Changes. *Langmuir* 2009; **25**(17):10100-10106.

59. Nar H, Messerschmidt A, Huber R, Vandekamp M, Canters GW. Crystal-Structure Analysis of Oxidized Pseudomonas-Aeruginosa Azurin at Ph 5.5 and Ph 9.0 - A Ph-Induced Conformational Transition Involves A Peptide-Bond Flip. *Journal of Molecular Biology* 1991; **221**(3):765-772.

60. Sapsford KE, Berti L, Medintz IL. Materials for fluorescence resonance energy transfer analysis: Beyond traditional donor-acceptor combinations. *Angewandte Chemie-International Edition* 2006; **45**(28):4562-4588.

61. Elmalk AT, Salverda JM, Tabares LC, Canters GW, Aartsma TJ. Probing redox proteins on a gold surface by single molecule fluorescence spectroscopy. *Journal of Chemical Physics* 2012; **136**:235101.

62. Zhang J, Lakowicz JR. Metal-enhanced fluorescence of an organic fluorophore using gold particles. *Optics Express* 2007; **15**(5):2598-2606.

63. Chowdhury MH, Ray K, Aslan K, Lakowicz JR, Geddes CD. Metal-enhanced fluorescence of phycobiliproteins from heterogeneous plasmonic nanostructures. *Journal of Physical Chemistry C* 2007; **111**(51):18856-18863.

64. Aslan K, Malyn SN, Geddes CD. Angular-dependent metal-enhanced fluorescence from silver island films. *Chemical Physics Letters* 2008; **453**(4-6):222-228.

65. Fu Y, Lakowicz JR. Single-molecule studies of enhanced fluorescence on silver island films. *Plasmonics* 2007; **2**(1):1-4.

66. Kinkhabwala A, Yu ZF, Fan SH, Avlasevich Y, Mullen K, Moerner WE. Large single-molecule fluorescence enhancements produced by a bowtie nanoantenna. *Nature Photonics* 2009; **3**(11):654-657.

67. Le Moal E, Leveque-Fort S, Potier MC, Fort E. Nanoroughened plasmonic films for enhanced biosensing detection. *Nanotechnology* 2009; **20**(22).

68. Mie G. *Annals of Physics* 1908; **25**:377.

69. Aroca R, Kovacs GJ, Jennings CA, Loutfy RO, Vincett PS. Fluorescence Enhancement from Langmuir-Blodgett Monolayers on Silver Island Films. *Langmuir* 1988; **4**(3):518-521.

70. Biteen JS, Pacifici D, Lewis NS, Atwater HA. Enhanced radiative emission rate and quantum efficiency in coupled silicon nanocrystal-nanostructured gold emitters. *Nano Letters* 2005; **5**(9):1768-1773.

71. Chumanov G, Sokolov K, Gregory BW, Cotton TM. Colloidal Metal-Films As A Substrate for Surface-Enhanced Spectroscopy. *Journal of Physical Chemistry* 1995; **99**(23):9466-9471.

72. Wokaun A, Lutz HP, King AP, Wild UP, Ernst RR. Energy-Transfer in Surface Enhanced Luminescence. *Journal of Chemical Physics* 1983; **79**(1):509-514.

73. Shen H, Lu GW, Ou MG, Marquette CA, Ledoux G, Roux S, Tillement O, Perriat P, Cheng BL, Chen ZH. How the morphology of biochips roughness increases surface-enhanced chemiluminescence. *Chemical Physics Letters* 2007; **439**(1-3):105-109.

74. Estrada LC, Roberti MJ, Simoncelli S, Levi V, Aramendia PF, Martinez OE. Detection of Low Quantum Yield Fluorophores and Improved Imaging Times Using Metallic Nanoparticles. *Journal of Physical Chemistry B* 2012; **116**(7):2306-2313.

75. Zijlstra P, Paulo PMR, Yu K, Xu Q-H, Orrit M. Chemical Interface Damping in Single Nanorods and Its Near Elimination by Tip-Specific Functionalization. *Angewandte Chemie-International Edition* 2012; **51**:8352-8355.

76. Kelly KL, Coronado E, Zhao LL, Schatz GC. The optical properties of metal nanoparticles: The influence of size, shape, and dielectric environment. *Journal of Physical Chemistry B* 2003; **107**(3):668-677.

Chapter 5

Fluorescence lifetime analysis of nitrite reductase from A. xylosoxidans at the single molecule level reveals enzyme mechanism[†]

[†] Tabares LC, Kostrz D, Elmalk A, Andreoni A, Dennison C, Aartsma TJ, Canters GW (2011) Fluorescence Lifetime Analysis of Nitrite Reductase from Alcaligenes xylosoxidans at the Single-Molecule Level Reveals the Enzyme Mechanism. Chemistry-A European Journal 17:12015-12019

Summary: *Immobilized fluorescently labelled bacterial nitrite reductase (NiR) has been studied during steady-state turn-over by single molecule fluorescence life time imaging (FLIM) microscopy. Two populations of single NiR molecules can be distinguished experimentally exhibiting different turn-over rates. The relative size of the populations varies with substrate (nitrite) concentration. The two populations are tentatively connected with two enzymatic routes: the 'reduction first' and the 'binding first' pathway.*

5.1 Introduction

Copper containing nitrite reductase (NiR) is a key enzyme in the bacterial denitrification and therefore plays important role in the global nitrogen cycle [1, 2]. The mode of action of this enzyme is highly contentious[3]. Herein we report new evidence on the enzyme's mechanism obtained from single molecule fluorescence lifetime imaging (FLIM) studies. We find two populations of molecules which correspond to two distinct mechanisms for the conversion of NO_2^- to NO. To our knowledge this is the first example of the use of lifetime switching as a tool to study the activity of a redox enzyme at the single molecule level.

NiR is a homotrimer with two Cu atoms per monomer (see section 5.6, Appendix, Figure A3)[4]. A type-1 (T1) copper site acquires reducing equivalents (electrons) which are transferred to a type 2 (T2) copper site where NO_2^- is converted into NO ($NO_2^- + e^- + 2H^+ \rightarrow NO + 2\ H_2O$). The dispute about the mechanism of this enzyme revolves around whether NO_2^- binds to the T2 copper site only after the latter has received an electron from the T1 copper site ('reduction first' mechanism)[5-9], or whether the electron is transferred only after binding of NO_2^- ('binding first' mechanism)[10-15]. These 'ordered' mechanisms are based on the assumption that there is some form of communication between the two centers about their state of reduction or the status of the substrate binding [16]. Conversely it has been argued by Wijma et al. that the enzyme operates according to a random sequential mechanism by which either pathway is feasible, the preponderant route depending on parameters such as pH and nitrite concentration [17]. This mechanism has received further support later on from the work of Scrutton and co-workers [18].

Herein we report evidence from single molecule FLIM studies that sheds new light on the catalytic mechanism of NiRs. This method is based on a newly devised technique which allows the redox behavior of T1 copper-containing oxido-reductases to be monitored[19-22]. The enzyme is covalently labeled with a fluorescent molecule whose emission spectrum overlaps with the absorption spectrum of the T1copper site (section 5.6, Appendix, Figure A4). A reduced T1 copper site has no absorption in the visible region and fluorescence is (partly) quenched through Förster resonant energy transfer (FRET) only when the site is oxidized. During turn-over the fluorescence changes reflect fluctuations in the redox state of the T1 copper site [19-23]. The application of this approach to the study of the electrochemical behavior of electron transfer proteins has been recently reported in this journal [24].

In earlier studies on green NiR (gNiR, section 5.6, Appendix, Figure A4) from *Alcaligenes faecalis*-S6 the intensity distributions in the fluorescence time traces of single molecules during turn-over exhibited severe overlap between the intensity histograms of the ox and the red form, allowing only an autocorrelation analysis of the data [22]. In the present case we have used the blue NiR from *A. xylosoxidans* (bNiR, section 5.6, Appendix, Figure A4) whose T1 copper site exhibits a much more pronounced absorbance around 600 nm (when oxidized) responsible for the protein's blue color [25]. This allows for an enhanced contrast between the red and ox forms of the T1 copper site of NiR, permitting more advanced data analysis. Another difference to the earlier studies is that instead of monitoring variations in intensity we have monitoring the fluorescence life time of labeled single enzyme molecules. The advantage is that the life time is insensitive to intensity fluctuations due to instrumental instabilities [26]. Two enzyme populations turning-over at different rates can be distinguished. Combining this information with a waiting time analysis we conclude that the two populations likely reflect the existence of two pathways, which may well correspond to the 'reduction first' and 'binding first' mechanisms.

5.2 Materials and Methods

5.2.1 Protein labeling

K329C bNiR was labeled at the free thiol group of the introduced Cys residue whilst the wild type (WT) protein was labeled at the N-terminus using modified versions of published protocols [18;19]. WT bNiR was exchanged into 100 mM 4-(2-hydroxyethyl)piperazine-1-ethanesulfonic acid (Hepes) pH 8.3 and the protein was incubated with 0.25 equivalents of ATTO 647N succinimidyl ester (ATTO-TEC GmbH) for 30 min at 4 ºC. Prior to labeling K329C bNiR was incubated for 2 h at 4 °C with 25-equivalents of TCEP and desalted on a Superdex 200 10/300 GL column (GE Healthcare) equilibrated in 20 mM Tris pH 7.5 containing 200 mM NaCl. Following this procedure, which removed some of the glutathione bound to Cys329 (*vide infra*), the protein was exchanged into 100 mM potassium phosphate pH 7.5 and incubated with an excess (in this case the exact amount of dye used was less important as the labeling ratio was dependent upon the amount of glutathione that had been removed from Cys329) of ATTO 647N maleimide (ATTO-TEC GmbH) for 1 h at 4 °C. Free dye was removed by desalting on a PD10 column (GE

Healthcare) equilibrated in 100 mM potassium phosphate pH 7.5. Labeling ratios were determined using ε values of 150 $mM^{-1}cm^{-1}$ at 644 nm for ATTO 647N and 60 $mM^{-1}cm^{-1}$ at 280 nm per monomer for bNiR.

5.2.2 Determination of switching ratios

Fluorescence time course experiments were performed on a Cary Eclipse fluorimeter in 50 mM potassium phosphate pH 7.5 using excitation and emission wavelengths of 630 and 657 nm respectively. The labeled protein concentrations were 31 nM for WT and 48 nM for K329C bNiR. The fluorescence intensities corresponding to the proteins in which the T1 copper was present as either Cu(I) or Cu(II) were determined by reducing the protein with sodium ascorbate containing phenazine-ethosulfate (PES) (stock solution of 1 M ascorbate plus 50 μM PES) and oxidizing with potassium ferricyanide (0.5 M stock solution) respectively. The switching ratio is the difference between the maximum (fully reduced protein) and the minimum fluorescence intensity (fully oxidized sample) divided by the maximum value.

5.2.3 Sample separation of single molecule studies

ATTO 647N-labeled K329C bNiR was immobilized on a glass slide in high purity agarose IV (Sigma) with a gel point of 36 ± 1.5 °C using a previously described procedure with some modifications. Prior to agarose deposition, the glass slides were incubated overnight in 10 % TritonX and sonicated sequentially for 30 min in 10 % TritonX, acetone, 3 M potassium hydroxide and methanol. Between these sonication steps the cover slips were rinsed and sonicated for 5 min in deionised (MilliQ) water. Subsequently the glass slides were incubated for 15 min in a 3:1 mixture of hydrochloric acid and nitric acid, sonicated for an additional 30 min, extensively rinsed with deionised water and spin-dried at 6000 rpm for 25 sec. The agarose (1 %) was melted in 100 mM potassium phosphate pH 7.5 and cooled to 50 °C. ATTO 647N-labeled K329C bNiR was added to give a final labeled protein concentration of 0.3 nM (the labeled protein is stable at 50 °C). Catalase (100 μg/ml) was added to the agarose in order to prevent possible deactivation of the enzyme. 200 μl of enzyme-containing agarose was spin coated onto a cleaned glass slide at 2000 rpm for 10 sec yielding a thin layer of gel. The coated glass was rapidly put into a holder and covered with 1ml of 100 mM potassium phosphate pH 7.5. Reduction was achieved using 100 mM phosphate pH 7.5 containing 100 μg/ml catalase, sodium ascorbate (10 mM) and phenazine-ethosulfate (PES) (100 nM). Oxidation was achieved with 100 mM phosphate pH 7.5 containing 100 μg/ml catalase and either 1.5 mM potassium ferricyanide or 50 mM $NaNO_2$. Enzyme turnover was studied in the presence of 100 mM phosphate pH 7.5 containing 100 μg/ml catalase, sodium ascorbate (10 mM) and PES (100 nM) plus

$NaNO_2$ (measurements were made using 5 μM, 50 μM, 500 μM, 1 mM and 5 mM $NaNO_2$). Although diffusion of chemicals through the thin agarose layer is very fast, a minimum of 10 minutes was allowed for equilibration. A fresh sample was used for each condition and measured for no more than one hour before discarding. Even at the lowest concentration of $NaNO_2$ the change in substrate concentration during this time is less than 1%.

5.2.4 Single molecule setup

Single-molecule fluorescence measurements were performed with a home-built scanning confocal microscope with Time-Correlated Single-Photon Counting (TCSPC) capabilities. Excitation was achieved with a pulsed picosecond diode laser (PDL 800-B, PicoQuant GmbH) emitting at 639 nm with 40 MHz repetition rate. The excitation beam was coupled into a single-mode fiber, passed through a narrow band clean-up filter (LD01-640/8-25, Semrock) and reflected by a dichroic mirror (Z 532/633 M) to a high numerical aperture (NA) oil objective (100× oil, NA 1.4, Zeiss) and on the sample surface. The power density at the sample was 0.5-1 $kWatt/cm^2$. The emitted fluorescence was filtered with an emission filter (D 675/50 M) and imaged onto the active area of a single photon counting avalanche photodiode (Perkin-Elmer SPCM-AQR-14) using a +4.5 mm achromatic lens. The data acquisition was done by the TimeHarp 200 TCSPC PC-board (PicoQuant, GmbH) working in the Time-Tagged Time-Resolved Mode. Samples were mounted onto a Physik Instrumente P-517 nanopositioner. Controlling of all the equipment and data acquisition were performed using SymPhoTime software (PicoQuant, GmbH).

5.2.5 Data collection

Fluorescence lifetime images were taken by scanning a 15x15 μm area of the sample with a step size of 75 nm and a dwell time of 4 ms per point. To determine the fluorescence lifetimes of the reduced and oxidized states (Figures 1A and 1B), a photon decay histogram of the photons collected over the whole image was constructed (Figure 2). Deconvolution with the instrumental response function (IRF) and a fit to a mono-exponential decay was carried out by using the SymPhoTime software (PicoQuant GmbH). Fluorescence decay times of (3.67±0.01) ns and (1.14±0.01) ns were found for the enzyme in the fully reduced and fully oxidized state, respectively. For all other conditions a sum of two exponentials was needed to obtain a satisfactory fit, demonstrating that in all these cases the sample contained a mixture of reduced and oxidized enzyme molecules. Fits were performed with fixed values of τ_1=1.1 and τ_2=3.7 ns.

5.2.6 Data analysis

To generate the FLIM pictures the fluorescence decay observed for each pixel was fit to a double exponential decay with fixed τ_1 and τ_2 (τ_1=1.1 and τ_2=3.7 ns) and by using the maximum likelihood algorithm, as implemented by the SymPhoTime software. Each pixel was colored either blue or red depending on whether the resulting average lifetime was smaller or larger than 2.5 ns, respectively. Pixels with a signal strength of less than 20 photons were discarded to reduce noise. Thus, we see (Figure 1) mostly red spots in the presence of reducing agents and mostly blue spots in the presence of oxidizing agents, while under turn-over conditions the spots consist of a mixture of red and blue pixels. The latter observation is a clear indication that during the scanning of a particular spot the T1 Cu is cycling between the oxidized and reduced state. A minimum of 6 pictures deriving from at least two independent measurements and containing an average of 50 spots per picture were analyzed for each condition.

To obtain the probability distribution of P_{ox} (Figure 3) for a spot a circular area around the center of the spot with a 15-pixel diameter (1.125μm) was selected and P_{ox} was calculated by dividing the number of blue pixels by the total number of red and blue pixels. Pixels containing less than 20 photons were rejected. P_{ox} histograms were fitted to a double Gaussian distribution except for the completely reduced or oxidized samples that were fit to a single Gaussian.

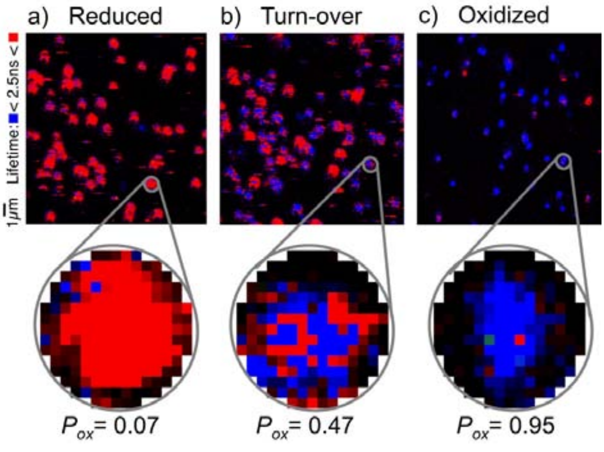

Figure 1. FLIM pictures of Atto647N-labelled bNIR-K329C immobilized in agarose gel. Top: in the presence of (a): 10mM ascorbate and 100 nM PES; (b): 10mM ascorbate,100 nM PES and 500 µM $NaNO_2$; and (c): 5 mM $NaNO_2$. Red and blue pixels correspond with fluorescence life times larger and smaller than 2.5 ns, respectively. Bottom: amplifications of selected spots.

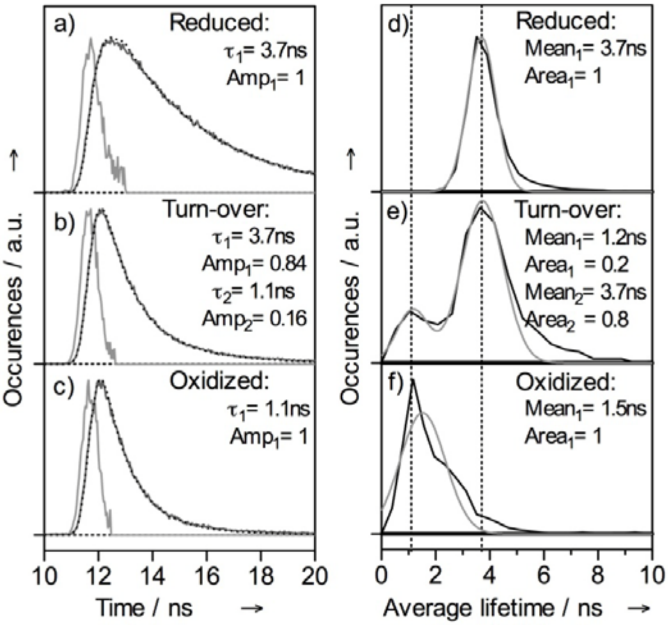

Figure 2. Fluorescence experiments on a sample of Atto647N-labelled bNIR-K329C immobilized in agarose gel. Data correspond to an area as depicted in Figure 1 containing ~40 spots. Left: Photon arrival time histograms for all photons present in one picture (dark lines) in the presence of (a):10mM ascorbate and 100 nM PES; (b): 10mM ascorbate,100 nM PES and 500 µM $NaNO_2$; (c): 5 mM $NaNO_2$. The gray line represents the instrument response function and dotted lines represent the fits to a single (a and c) or double exponential decay (b) (since fits follow very closely the experimental curves they may be difficult to distinguish in the figure). Fit results are given inside the picture. Right: Histogram of the photon life time per pixel for the same conditions as in the left panel (black line). The gray line presents the fit to a single (d and f) or double (e) Gaussian distribution (fit results are given in the picture).

5.3 Results

Figure 1, top, shows a 15x15 µm^2 area of a glass slide covered with a 300pM solid solution of Atto 647N-labelled NiR (NiR-A647N) in agarose, pH 7.5, at room temperature as observed under the fluorescence microscope. The size of the spots in Figure 1 is slightly larger (~600 nm full width at half maximum, FWHM) than the diffraction limit (~300 nm FWHM). The spots are scanned by small steps, each pixel in the image corresponding with a step size of 75 nm (Figure 1, bottom). The images were recorded under reducing (Figure 1a), oxidizing (Figure 1c) and turn-over (Figure 1b) conditions. Each spot corresponds with a single molecule of NiR that is singly labeled. The evidence for this derives from the

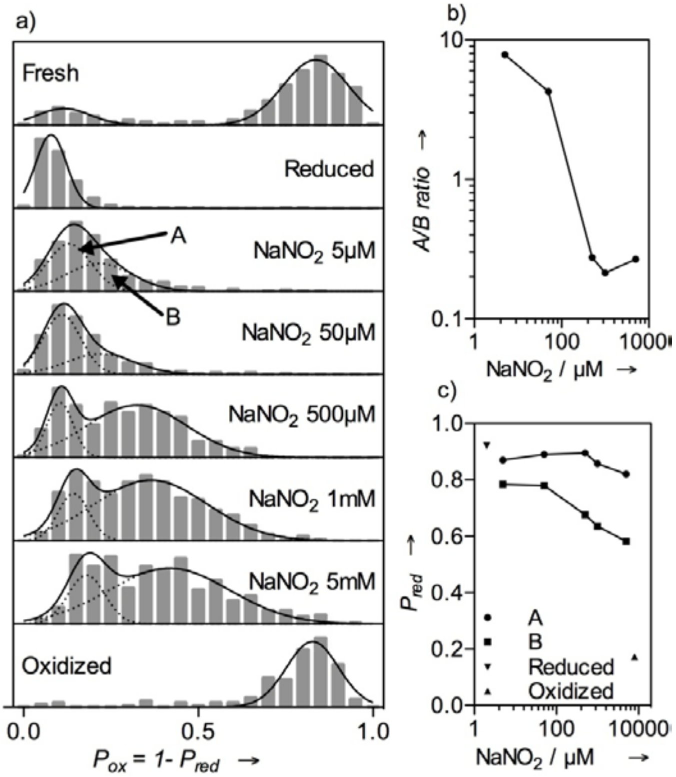

Figure 3. (a) Histograms of Pox observed under conditions as specified in the figure. For the panels labeled 'Fresh', 'Reduced' and 'Oxidized' the solid lines represent single Gaussian fits. In all other panels the fits (solid lines) are the sum of two Gaussian distributions (dotted lines). (b) Ratio between numbers of molecules in population A and population B during turn-over as a function of nitrite concentration. (c) Centers of the Gaussian distributions as function of nitrite concentration during turn-over. The values corresponding with completely reduced and completely oxidized enzyme are also shown.

bleaching behavior that every now and then is observed for a spot. Bleaching appears as a single step event by which the intensity is reduced to background levels.

Examples of fluorescence decay curves obtained by averaging over all the pixels in a 15×15 μm^2 area (see Figure 1) are presented in Figures 2a-2c together with the histogram of life times observed for the ensemble of pixels in the same area (Figures 2d-2e). The fluorescence decay times for the oxidized and reduced forms of NiR amount to (1.16±0.01) and (3.67±0.01) ns, respectively. This change corresponds with a FRET efficiency of 0.7 in good agreement with the 0.8 FRET efficiency observed for the bulk (see section 5.6, Appendix). The pixels in the images of Figure 1 have been presented in false color, red and blue representing pixels for which the observed fluorescence life time is >2.5 ns or <2.5 ns, respectively. Thus, red corresponds with the reduced state and blue with the oxidized state. It is clear that under reducing (Figure 1a) or oxidizing (Figure 1c) conditions the enzyme molecules are overwhelmingly in the reduced or the oxidized state, respectively, while under turn-over conditions (Figure 1b) the redox state of the enzyme molecules alternates in time between reduced and oxidized during the scanning. The time-averaged degree of oxidation of a single spot, P_{ox}, ($P_{\mathrm{ox}} = 1 - P_{\mathrm{red}}$) was obtained by counting the number of blue pixels and dividing them by the sum of the blue and red pixels in the spot.

Figure 3a represents histograms of P_{ox} values for a few hundred spots as a function of the concentration of reductant and/or substrate (NO_2^{-}). As expected, under purely reducing or oxidizing conditions the distributions center at values of P_{ox} close to 0 or 1, respectively. Under turn-over conditions a much broader distribution of P_{ox} values is observed that can be decomposed into two populations, one (labeled A) that remains centered close to P_{ox} = 0, the other one (labeled B) that progressively moves towards larger values of P_{ox} as the concentration of substrate (NO_2^{-}) increases (see Figure 3c). At the same time the fraction of molecules in population A decreases with respect to population B (Figure 3b). Although

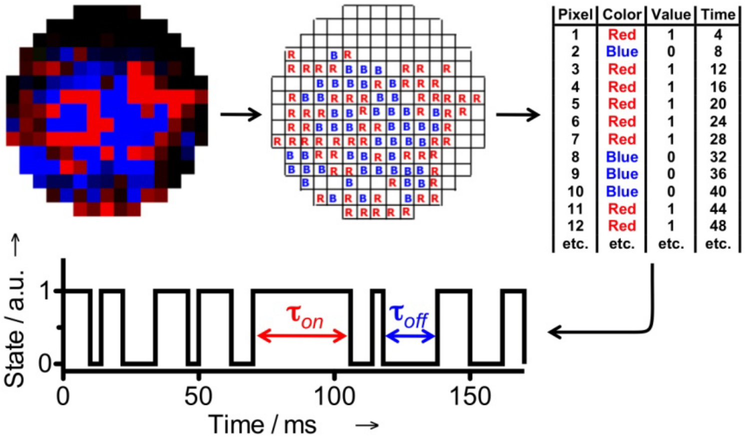

Pixel	Color	Value	Time
1	Red	1	4
2	Blue	0	8
3	Red	1	12
4	Red	1	16
5	Red	1	20
6	Red	1	24
7	Red	1	28
8	Blue	0	32
9	Blue	0	36
10	Blue	0	40
11	Red	1	44
12	Red	1	48
etc.	etc.	etc.	etc.

Figure 4. Analysis of the time dependent behaviour of a single enzyme molecule.The 75x75 nm pixels of the image (top, left) are scanned sequentially from top to bottom row by row, left to right, with a dwell time of 4 ms per pixel. A pixel is assigned a value of 0 or 1 depending on whether the fluorescence life time is < 2.5 ns (blue) or > 2.5 ns (red), respectively (top, middle). The values are collected in a table (top, right) whereby the pixels for which no signal could be read out due to a low intensity, were omitted. The pixel values were then plotted on a time axis (bottom) and waiting times (τ_{on} and τ_{off}) were read out.

the mean P_{ox} of population A or B under different turn-over conditions does not match the degree of oxidation encountered in-bulk under the same conditions, the overall weighted average, $[\sum P_{ox}\cdot n(P_{ox})] / [\sum n(P_{ox})]$ does (Section 5.6, Appendix, Figure A6).

A waiting time analysis was performed by assigning a value of 1 or 0 to pixels, depending on whether the observed life time for a pixel was larger or smaller than 2.5 ns, respectively. The values were then pasted on a time axis each value taking a time interval of 4 ms (see Figure 4). Pixels for which no definite value for the fluorescence life time could be determined, for instance due to lack of sufficient photons, were omitted. Pixels in a row that did not correspond to the spot that was analyzed, were ignored. It was checked that the systematic error in the waiting time distributions introduced by this procedure was less than

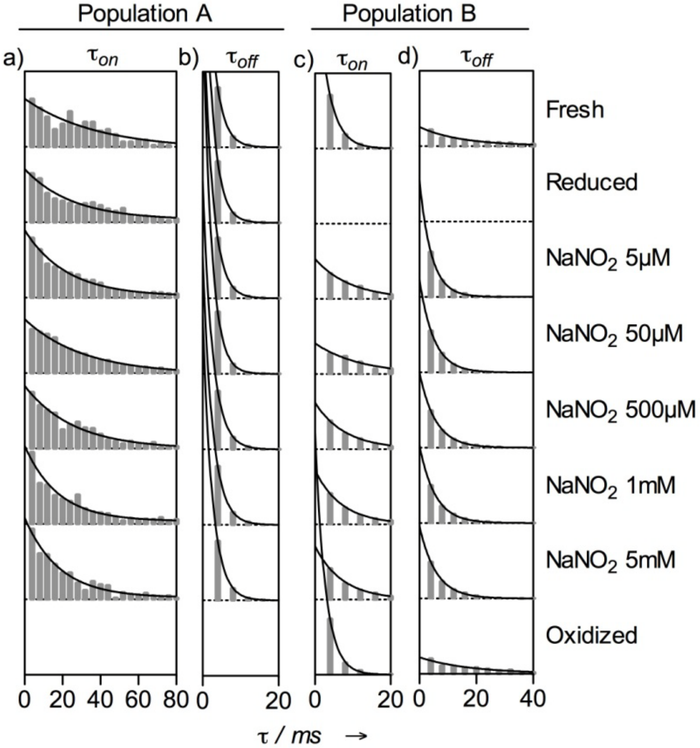

Figure 5. Histograms for the on (panels a and c) and off (panels b and d) times, τ_{on} and τ_{off}, for population A (a, b) and population B (c, d). To limit cross-contamination between the populations, for each condition the crossing point of the Gaussian fits was determined (P_c) and populations A and B were defined as the collections of spots with $P_{ox} \leq P_c - 0.025$ and $P_{ox} \geq P_c + 0.025$, respectively. The histograms are fit with single exponentials.

10% (see Appendix). Moreover it appeared that the results were not particularly sensitive to the detailed shape and size of the area that was used to define a spot (see Section 5.6, Appendix).

The on- and off-times (τ_{on} and τ_{off}) for a large number of spots were combined and used to construct histograms of τ_{on} and τ_{off} (see Figure 5). They could be fitted by single exponentials resulting in characteristic life times, τ_{red} and τ_{ox}, which denote the times during which the enzyme molecule stays in the reduced and the oxidized form, respectively. Values of τ_{red} and τ_{ox} as determined for different turn-over conditions are presented in Figure 6.

5.4 Discussion

As stated above, the data in Figure 3 point to the existence of two populations of NiR molecules. Molecules of population A exhibit an average degree of reduction close to 1 while the average degree of reduction of population B moves to lower values as the nitrite concentration increases. It is interesting to compare the waiting time distributions for the two populations.

Previously reported single molecule data on gNiR were analyzed with the customary three-state cyclic scheme depicted in Figure 7a [22]. In general, with a such a scheme, waiting time

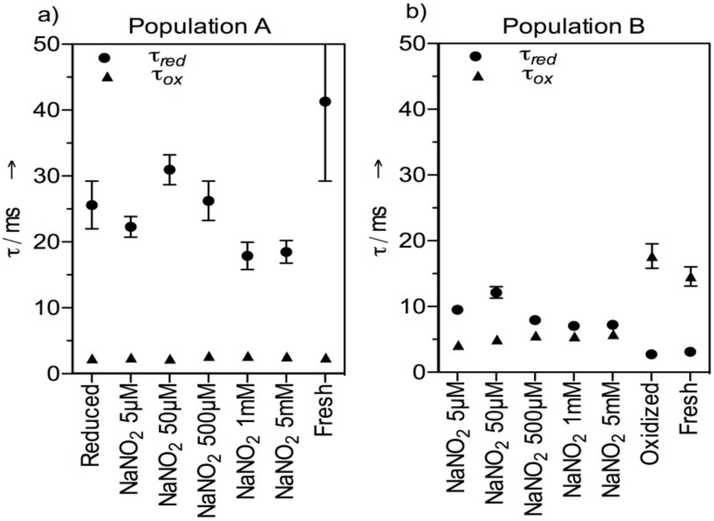

Figure 6. Life times in the reduced and the oxidized state (τ_{red} and τ_{ox}) for the populations A (panel a) and B (panel b) as determined from single exponential fits of the histograms of Figure 5. Error bars represent the standard error of the fit (in cases were error bars are not shown the standard error is smaller than the symbol size).

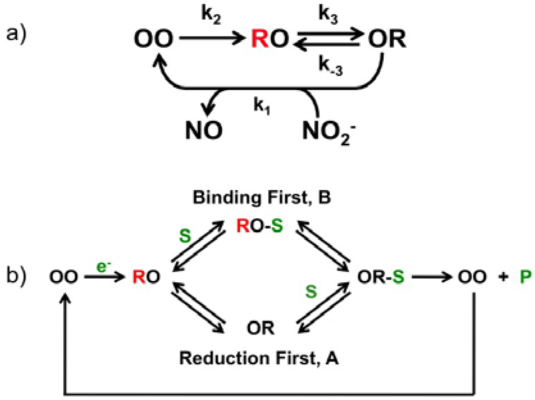

Figure 7. Scheme of the catalytic cycle of nitrite reductase. Scheme a represents the simple three-state cycle, in scheme b step 3 has been resolved in two steps leading to two alternative routes: the ‘reduction first’ route (route 'A') and the ‘binding first’ route (route 'B'). The symbols with the two capitals represent, from left to right, the T1- and the T2-sites, O and R denoting the oxidation state (oxidized and reduced, respectively). Red denotes the highly fluorescencing state. S denotes the substrate (NO_2^-) and P the product ($NO+H_2O$). The electron donor has been omitted for simplicity.

distributions are the sum of two exponentials [27]. In the present study however, bNiR FLIM data can be adequately fit with single exponentials (see Figure 5). This means that the faster decaying component is not resolved in our experiment where time resolution is limited by the dwell time per pixel of 4 ms and that we essentially monitor the reduction and oxidation of the T1copper site in time, *i.e.*, steps 2 and 3 according to the scheme in Figure 7a. During turn-over molecules in population A stay in the reduced state for about 20-30 ms while for population B this number is ~10 ms (see Figure 6). For both populations we observe that the waiting time for the next reduction step amounts to a few ms. For the resting state, on the other hand, the behavior is different (Figure 6; see data points denoted by ‘Fresh’, ‘Oxidized’ and ‘Reduced’): molecules in population A spend longer times in the reduced form as compared to under turn-over conditions, while the opposite happens for population B, where molecules spend much longer times in the oxidized form.[‡] We note that the width of the distributions in Figure 3, in particular for population B, increases considerably when the nitrite concentration increases. This has

---

[‡] In the resting states, apparently, still some switching between the T1 redox states is observed possibly connected with intramolecular electron transfer between the T1- and the T2-sites.

been observed before for green-NiR and has been ascribed to a distribution in k_3, and may derive from structural disorder.

The enzyme kinetics of NiR in the bulk and in electrochemical experiments have been interpreted[17,28] on the basis of a scheme (Figure 7b) that distinguishes between the 'reduction first' and the 'binding first' pathway, which are labeled in Figure 7b by '*A*' and '*B*'. It is known from these experiments that at higher nitrite concentrations, and also at low pH, pathway '*B*' is favored over '*A*'. It is tempting to identify populations A and B with molecules that follow pathway '*A*' and pathway '*B*', respectively. Preliminary results show that the relative amount of molecules in populations A and B can be modulated by pH, indeed, in agreement with literature data on bulk solutions[17,28]. This would mean that electron transfer from the T1 to T2 copper site in molecules following path '*A*' is appreciably slower than in molecules that follow path '*B*' where nitrite is bound to the T2 copper site. This might be related to a change in driving force and/or in electronic coupling between the centers when nitrite binds. What causes a molecule to follow path '*A*' or '*B*'? Preliminary experiments seem to indicate that transitions from population A to population B are possible but occur at a relatively infrequent rate on the time scale of the present experiments (section 5.6, Appendix, Figure A7). This is the subject of ongoing research.

5.5 Conclusion

The present work confirms the random sequential character of the mechanism of NiR. The enzyme may follow the 'binding first' as well as the 'reduction first' pathway. The enzyme kinetics also exhibit features that are reminiscent of an ordered mechanism, in the sense that once an enzyme molecule operates according to path '*A*' or path '*B*', it keeps doing this at least for a number of turn-overs. The relatively low number of photons collected per spot before the label bleached necessitated the waiting times of large numbers of spots to be combined. Thereby a possible variation in τ_{on} and τ_{off} from spot to spot was averaged out. Future experiments will be aimed at obtaining improved signal/noise that would allow the observation of variations in rate from molecule to molecule.

5.6 Appendix

5.6.1 Site directed mutagenesis

The K329C mutation to the blue nitrite reductase (bNiR) from *Alcaligenes xylosoxidans* was created using QuikChange mutagenesis (Stratagene). The plasmid pET22b-bNiR [25] was used as the template along with the following primers; 5'-CTGATGAAGCA GATC**TGC**GCGCCCGCGCCGATTCC-3' (forward) and 5'-GGAATCGGCGCGGGC GC**GCA**GATCTGCTTCATCAG-3' (reverse). The sequences of both strands of the mutated plasmid (pET22b-bNiRK329C) were verified.

5.6.2 Over-expression, isolation and purification of the wild type and K329C bNiR

Wild type (WT) bNiR was over-expressed, isolated and purified as described previously [26]. For the K329C variant the only modification to this method was that the amount of streptomycin sulfate used for the precipitation of DNA during purification was lowered to 0.3 %. Purity was confirmed by sodium dodecyl sulfate polyacrylamide gel electrophoresis (12.5 % gel), with both WT and K329C bNiR having A_{280}/A_{594} ratios of around 11 for the fully oxidized forms. Protein concentrations were determined using a molar absorption coefficient (ε) of 5200 $\text{M}^{-1}\text{cm}^{-1}$ at 594 nm [28].

5.6.3 Protein characterization

Gel filtration and matrix assisted laser absorption ionization time-of-flight mass spectrometry (MALDI-TOF-MS) studies were performed as described previously[24, 29] in 20 mM Tris pH 7.5 containing 200 mM NaCL and 40 mM Tris pH 7.5 respectively. MALDI-TOF-MS was also performed on a K329C sample and had been incubated with 300 equivalents of tris(2-carboxyethyl) phosphine hydrochloride (TCEP) for 1 h at room temperature. UV/vis spectra of oxidized WT and K329C bNiR were acquired at room temperature on a Perkin-Elmer λ35 spectrophotometer in 20 mM 2-(N-morpholino)-ethanesulfonic acid (Mes) pH 6.0 X-band EPR spectra of oxidized WT and K329C bNiR were acquired on a Bruker EMX EPR spectrometer at 80 K. protein sample for EPR were exchanged by ultrafiltration into 40 mM Tris pH7.5, concentrated and glycerol was add to the final concentration of 40 % (final Tris concentration of 24 mM). diphenylpicylhydrazyl (DPPH) and α,γ-bis-diphenylene-β-phenyl allyl (BDPA) were used as external reference compounds.

The elution volume of the K329C bNiR variant on the gel filtration column (73.9 ml) corresponds to a molecular weight (MW) of 114.3 kDa indicative of the protein being a

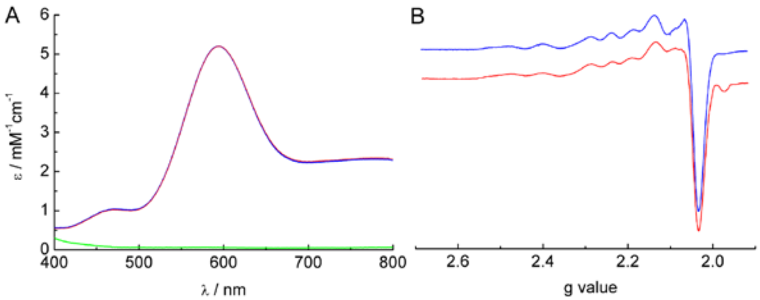

Figure **A1.** UV/Vis (A) and X- band EPR (B) spectra of oxidized WT (blue lines) and oxidized K329C (red lines) bNiR. The optical spectra of both species coincide. The spectra of both reduced species also coincide (green line). The UV/Vis spectra (room temperature) are obtained in 20 mM Mes pH 6.0 whilst EPR spectra (~ 80 K) are of samples in 24 mM Tris pH 7.6 (40 % glycerol).

stable trimer in solution, which is also the case for the WT protein (elution volume of 73.8 ml corresponding to a MW of 115.2 kDa). MALDI-TOF-MS gives a molecular weight of 36928.0 for the K329C bNiR monomer, which is 298.25 Da heavier than the theoretical value (36629.75 Da). This mass difference indicates that a small molecule, most likely glutathione (MW = 307.3 Da), attaches to the mutated protein via the introduced Cys residue during over-expression in the cytosol of *Escherichia coli*. Consistent with this, K329C bNiR reduced with TCEP gives a MW of 36618.4, very close to the theoretical value. The UV/Vis and EPR spectra of WT and K329C bNiR are very similar (See section 5.6, Appendix, Figure A1) and therefore this mutation has no effect on the structure of either the T1 or T2 copper sites. Furthermore, the removal of glutathione with TCEP did not influence the spectral properties of the variant.

The fluorescence switching ratios are almost identical for WT and K329C bNiR (0.86 and 0.84, respectively; see section 5.6, Appendix, Figure A2), which are labeled at the N-terminus and Cys329 respectively. The single molecule experiments described in this study were performed with the K329C variant as labeling via a Cys residue is more specific. Furthermore, the location for the introduced Cys residue was chosen so that the distance between the label and the T1 copper site within the same monomer was optimal for FRET whilst limiting the influence of redox changes at the two other T1 copper sites in the trimer. This is also ensured by maintaining a low labeling ratio (~11 % for the ‘in bulk’ experiments with WT and ~13 % for the K329C mutant samples used for ‘in bulk’ and the single molecule measurements).

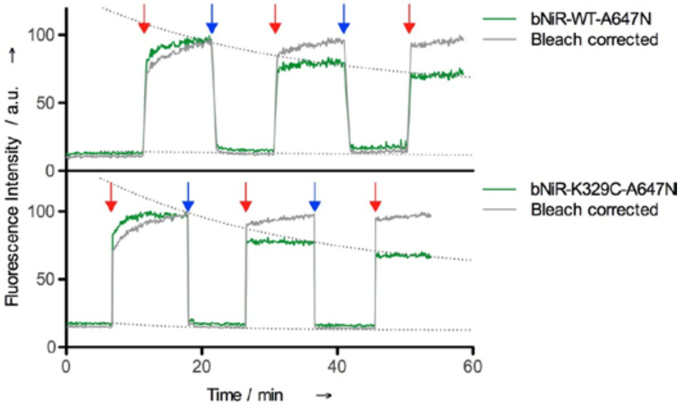

Figure A2. Fluorescence intensity changes upon reduction and oxidation of ATTO 647N-labeled WT (top) and K329C (bottom) bNiR. The labeled protein concentrations are 31 and 48 nm respectively with the samples in 50 mm phosphate pH 7.5. The arrows indicate the addition of (red) an excess of reductant (sodium ascorbate plus PES) and (blue) oxidant (potassium ferricyanide). The fluorescence intensity changes were followed at 657 nm using an excitation wavelength of 630 nm. The green trace is the experimental trace. It is known that the ATTO 647N dye under illumination may bleach in time. The manufacturer provides an example with a time constant of 28 min which was used here (dotted lines). When corrected for this (grey traces) the slow intensity decay with time disappears.

Figure A3. Structure of bNiR showing the entrance of the electron through the T1 Cu, the subsequent transfer of the electron to the T2 Cu and the conversion of NO_2^- into NO at the T2 Cu site. A dye molecule at position K329 is shown in purple. The reductant that reduces the T1-site is symbolized by X.

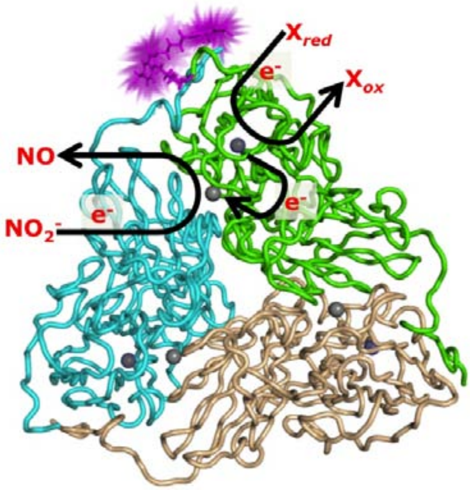

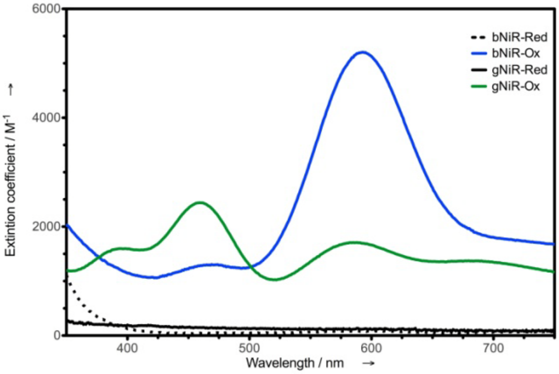

Figure A4. The visible absorption spectra of blue-NiR (bNiR) and green-NiR (gNiR) in the reduced (Red) and the oxidized (Ox) states.

5.6.4 Waiting time histograms

Waiting time histograms were constructed as described in the main text. We note that the data were obtained from a 15x15 µm surface area that was scanned row by row. This means that of all the pixels recorded for a single spot only the pixels in one row are contiguous in time, *i.e.*, there is an interval of about 0.8 sec between the data points in two consecutive rows (0.8 sec is the time needed by the scanner to scan a full line: 200 pixels of 4 ms each). We have disregarded the 0.8 sec time intervals between subsequent rows and treated the remaining pixels for one spot as a continuous series of time points. To check if this would introduce any major an On/Off trace was simulated by generating a 6×10^{6} row of data-points $y(x)$ in which x is the time and $y = 1$ or 0. The x-axis was divided in increments of 1×0^{-5} sec mimicking a 60 s long trajectory with 0.01 ms resolution. At $x = 0$, y was arbitrarily set to "On" ($y=1$), followed by one "Off"-period ($y=0$) before another On-period was started. While Off-periods were fixed to 1000 points (τ_{off} = 10 ms), the On-periods were allowed to last for a time $\tau_{\mathrm{on}} = -1 \times \ln(rand) \times \tau_{\mathrm{red}}$, where *rand* is a computer-generated evenly-distributed random number between 0-1. In this way the On-periods lasted for a random time τ_{on}, the cumulative distribution of which obeys an exponential decay with time constant τ_{red}. Traces were generated in this way for τ_{red} = 0.5, 1, 3, 5, 10, 25, 50, 100 or 200 ms. These On/Off traces were then binned with bin sizes of 1 or 4 ms and histograms for τ_{on} were constructed (Figure A5).

To account for the non-contiguous character of the experimental time series the 60 s, 4ms-binned simulated-trace was treated as in the spot measurements, *i.e.*, blocks were extracted separated by intervals of 800 ms. The latter periods were discarded. The extracted blocks

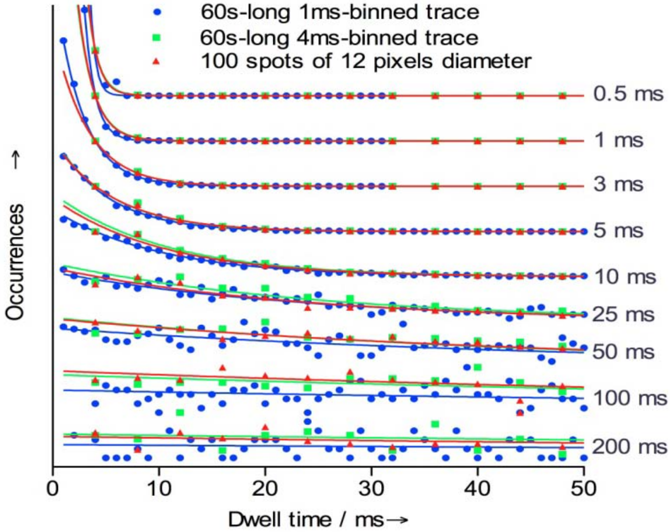

Figure A5. Dwell time histogram for the On-state of simulated time traces using different red values as specified at the right side of the picture (see text for details). Lines show the fit to a simple exponential decay

had subsequent lengths of 20 ms, 36 ms, 44 ms, 52 ms, 52 ms, 52 ms, 52 ms, 52 ms, 44 ms, 36 ms, 20 ms. This pattern corresponds with a circular spot with a 12 pixel diameter. The extracted blocks were placed one behind the other to form a continuous time trace. For each τ_{red} 100 independent traces were generated to mimic 100 spots, the time traces of which were analysed in the same way as the experimental data. The simulated data were used to construct dwell time histograms as presented in Figure A5. They were fitted with single exponentials, the exponential decay constants providing estimates of τ_{red}. Apart from the procedure described above to construct and analyze spots, we also analyzed the full 60 sec trajectories, not only with 4 ms bins but also with 1 ms binning. The results are summarized in Table A1. A less extensive simulation mimicking only 50 spots of 5 pixel diameter produced results that did not deviate from the 4 ms continuous traces by more than 30%.

As can be seen from Table A1, the effect of bin size on the extracted time constant becomes noticeable only towards shorter time constants where τ_{red} is of the order of or smaller than the bin size. More importantly, the procedure of chopping up the time trace - as done in this study - for analyzing the experimental data, does not seem to introduce appreciable errors. Apart from the small error that may be introduced, the attractive feature

Theoretical τ_{red} (ms)	60s-long 1ms-binned trace		60s-long 4ms-binned trace		100 spots of 12 pixels diameter; bin size 4 ms	
	Fit τ (ms)	Abs. error (%)	Fit τ (ms)	Abs. error (%)	Fit τ (ms)	Abs. error (%)
0.5	0.5	1	1.0	95	0.9	82
1	1.0	2	1.5	52	1.5	46
2.5	2.6	2	3.2	28	3.2	28
5	5.0	1	5.6	12	5.7	14
10	10.2	2	10.5	5	10.3	3
25	25	1	27	2	24	4
50	52	3	47	7	50	1
100	112	12	108	8	102	2
200	198	1	178	11	137	32

Table A1. Results of fitting of dwell time histograms of presented in figure A5 to a single exponential decay. The table shows results of decay times (τ) for the dwell time histograms of traces simulated with τ_{red} values of 0.5, 1, 3, 5, 10, 25, 50, 100 or 200 ms (see text). The errors represent the absolute (Abs.) error of the fitted decay when compared to the theoretical value of the simulation.

of the procedure followed here is that with a 10 minutes measurement (which does not involve selection of individual molecules) and a computational procedure that proves to be fast, it is possible to identify the state (oxidized, reduced or turning over) of every molecule together with its kinetics parameters. The use of lifetime over intensity also eliminates background effects and artifacts introduced by dye blinking.

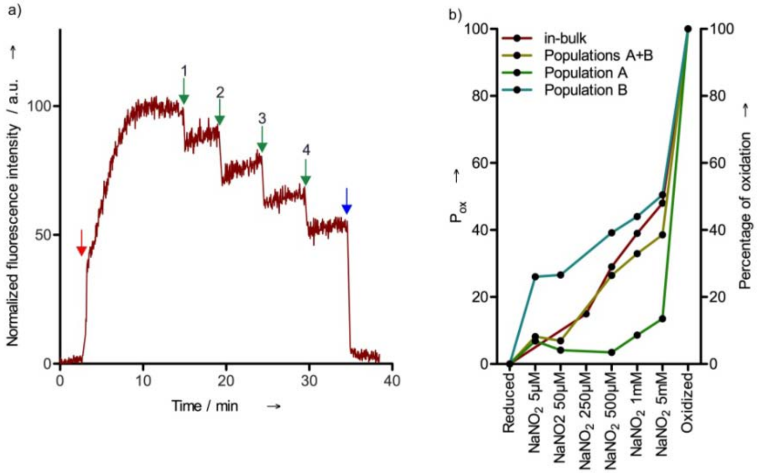

Figure A6. Left: Normalized in-bulk fluorescence intensity time trace of bNiR-Atto647N, corrected for bleaching (see Figure A2). The arrows indicate the addition of reductant (red; 10 mM sodium ascorbate plus 100 nM PES), $NaNO_2$ (green: 1, 250 µM; 2, 500 µM; 3, 1000 µM and 4, 5000 µM, final concentrations) and oxidant (blue; 20 mM $K_3Fe(CN)_6$). **Right:** Comparison of mean P_{ox} for population A, B and A+B with the in-bulk percentage of oxidation calculated from the left panel. The data was normalized between 0 and 100.

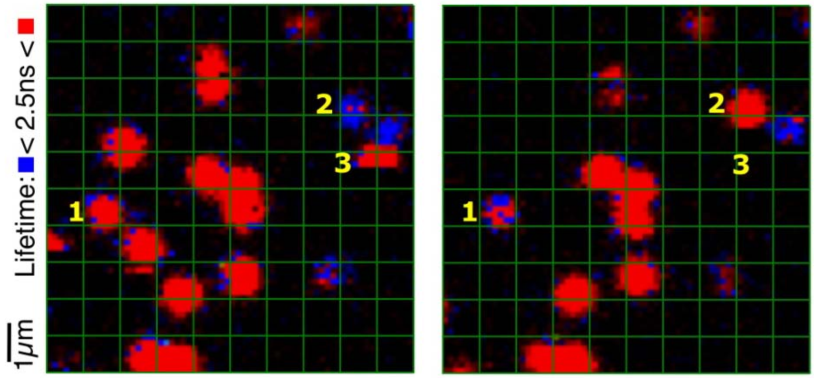

Figure A7. Example of switching between populations. The two images were taken of the same area under the same conditions with an interval of 10 min (left first). Molecule 1 switches from population A to B while the opposite happens to molecule 2. The green grid (1×1 µm) helps to compare the position of the molecules. A few molecules disappear when going from the left image to the right due to bleaching. In the left image a single-step photo-bleaching can be observed during the scan for molecule 3.

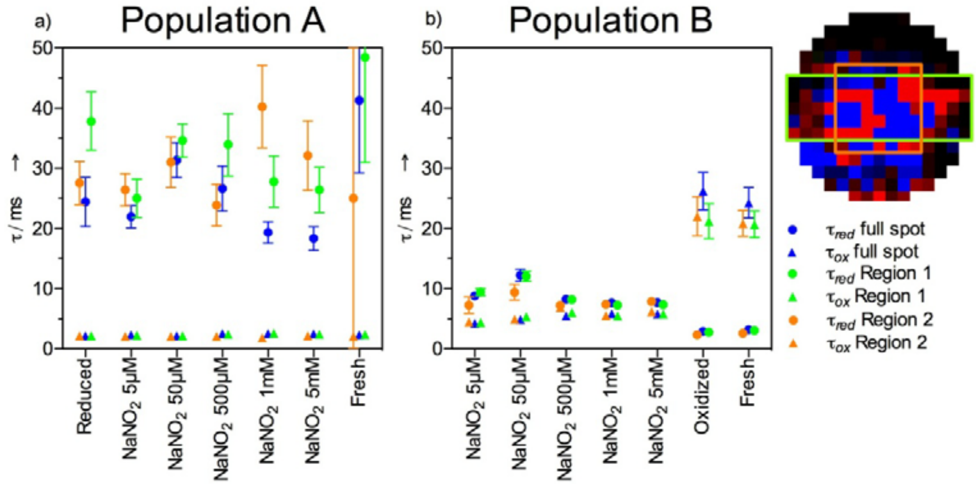

Figure A8. Effect of selected spot area on the values of τ_{red} and τ_{ox} as obtained for the populations A (panel a) and B (panel b). Blue points: data obtained by analyzing all the pixels within a spot with a diameter of 15 pixels. Orange points: data obtained by analyzing all the pixels within a square of 7×7 pixels around the center of the spot; green points: data obtained by analyzing all the pixels within an area of 5×15 pixels around the center of the spot. The different areas and the corresponding spots are presented at the right of the figure. The spot depicted in Figure 4 was used above for illustrative purposes.

References

1. Ferguson SJ. Nitrogen cycle enzymology. **1998,** *2* 182-193.
2. Zumft WG. Cell biology and molecular basis of denitrification. *Microbiol. Mol. Biol. Rev.* **1997,** *61* 533-616.
3. Ghosh S. Spectroscopic and Computational Studies of Nitrite Reductase: Proton Induced Electron Transfer and Backbonding Contributions to Reactivity. *J. Am. Chem. Soc.* **2009,** *131* 277-288.
4. Adman ET and Murphy MEP in Handbook of Metalloproteins, Vol. 2 (Eds. : A. Messerschmidt, R. Huber, T. Poulos, K. Wieghardt), Wiley, New York, 2001, pp. 1381 –1390.
5. Abraham ZHL. pH-dependence for binding a single nitrite ion to each type-2 copper centre in the copper-containing nitrite reductase of Alcaligenes xylosoxidans. *Biochem. J.* **1997,** *324* 511-516.
6. Jackson MA. Evidence for An No-Rebound Mechanism for Production of N2O from Nitrite by the Copper-Containing Nitrite Reductase from Achromobacter-Cycloclastes. *Febs Lett.* **1991,** *291* 41-44.
7. Averill BA. Dissimilatory nitrite and nitric oxide reductases. *Chem. Rev.***1996,** *96* 2951-2964.
8. Hulse CL. Evidence for A Copper Nitrosyl Intermediate in Denitrification by the Copper-Containing Nitrite Reductase of Achromobacter-Cycloclastes. *J. Am. Chem. Soc.* **1989,** *111* 2322-2323.
9. Wasser IM. Nitric oxide in biological denitrification: Fe/Cu metalloenzyme and metal complex NOx redox chemistry. *Chem. Rev.* **2002,** *102* 1201-1234.
10. Suzuki S. Metal coordination and mechanism of multicopper nitrite reductase. *Acc. Chem. Res.* **2000,** *33* 728-735.
11. Murphy MEP. Structure of nitrite bound to copper-containing nitrite reductase from Alcaligenes faecalis - Mechanistic implications. *J. Biol. Chem.* **1997,** *272* 28455-28460.
12. Adman ET. The Structure of Copper-Nitrite Reductase from Achromobacter Cycloclastes at 5 Ph Values, with No2- Bound and with Type-Ii Copper Depleted. *J. Biol. Chem.* **1995,** *270* 27458-27474.
13. Kataoka K. Functional analysis of conserved aspartate and histidine residues located around the type 2 copper site of copper-containing nitrite reductase. *J. Biochem.* **2000,** *127* 345-350.
14. Boulanger MJ. Catalytic roles for two water bridged residues (Asp-98 and His-255) in the active site of copper-containing nitrite reductase. *J. Biol. Chem.* **2000,** *275* 23957-23964.
15. Hough MA. Crystallography with online optical and X-ray absorption spectroscopies demonstrates an ordered mechanism in copper nitrite reductase. *J. Mol. Biol.* **2008,** *378* 353-361.
16. Strange RW. Structural and kinetic evidence for an ordered mechanism of copper nitrite reductase. *J. Mol. Biol.* **1999,** *287* 1001-1009.
17. Wijma HJ. A random-sequential mechanism for nitrite binding and active site reduction in copper-containing nitrite reductase. *J. Biol. Chem.* **2006,** *281* 16340-16346.
18. Brenner S. Demonstration of Proton-coupled Electron Transfer in the Copper-containing Nitrite Reductases. *J. Biol. Chem.* **2009,** *284* 25973-25983.
19. Schmauder R. Sensitive detection of the redox state of copper proteins using fluorescence. *J. Biol. Inorg. Chem.* **2005,** *10* 683-687.

20. Kuznetsova S, Zauner G, Schmauder R, Mayboroda OA, Deelder AM, Aartsma TJ, Canters GW. A Forster-resonance-energy transfer-based method for fluorescence detection of the protein redox state. *Anal. Biochem.* **2006,** *350* 52-60.

21. Schmauder R. The oxidation state of a protein observed molecule-by-molecule. *ChemPhysChem* **2005,** *6* 1381-1386.

22. Kuznetsova S, Zauner G, Aartsma TJ, Engelkamp H, Hatzakis N, Rowan AE, Nolte RJM, Christianen PCM, Canters GW. The enzyme mechanism of nitrite reductase studied at single-molecule level. *Proc. Natl. Acad. Sci. U. S. A.* **2008,** *105* 3250-3255.

23. Davis JJ, Burgess H, Zauner G, Kuznetsova S, Salverda J, Aartsma T, Canters GW. Monitoring interfacial bioelectrochemistry using a FRET switch. *J. Phys. Chem. B* **2006,** *110* 20649-20654.

24. Salverda TM, Patil AV, Mizzon G, Kuznetsova S, Zauner G, Akkilic N, Canters GW, Davis JJ, Heering HA, Aartsma TJ. Fluorescent Cyclic Voltammetry of Immobilized Azurin: Direct Observation of Thermodynamic and Kinetic Heterogeneity. *Angew. Chem., Int. Ed.* **2010,** *49* 5776-5779.

25. Sato K and Dennison C.. Active site comparison of Co-II blue and green nitrite reductases. *Chem.-Eur. J.* **2006,** *12* 6647-6659.

26. Sorokina M. Fluorescent Lifetime Trajectories of a Single Fluorophore Reveal Reaction Intermediates During Transcription Initiation. *Chem. Phys.* **1999,** *247* 11-22.

27. Qian H and Elson EL.. Single-molecule enzymology: stochastic Michaelis-Menten kinetics. *Biophys. Chem.* **2002** *102-102* 565-576.

28. Wijma HJ, Jeuken LJC, Verbeet MP, Armstrong FA, Canters GW. Protein film voltammetry of copper-containing nitrite reductase reveals reversible inactivation. *J. Am. Chem. Soc.* **2007,** *129* 8557-8565.

29. Sato K, Firbank SJ, Li C, Banfield MJ, Dennison C. The importance of the long type 1 copper-binding loop of nitrite reductase for structure and function. *Chem.-Eur. J.* **2006,** *14* 5820-5828.

Summary

Proteins are responsible for many different functions in the living cell. They are involved in enzymatic catalysis, transport and storage, coordinated motion, mechanical support, immune protection, generation and transmission of nerve impulses, control of growth and cell differentiation, etc. Our understanding of biological systems is bounded by our knowledge of the structure and function of these proteins. Over the past decade increasingly sophisticated techniques have been developed to visualize the distribution, the dynamics, and the interactions of proteins and other components in living cells with single-molecule sensitivity. The rapidly increasing knowledge of biological processes in various organisms and the understanding of genetic functions spurred a revolution in biotechnology, i.e., the use of biological processes to create useful products. Biotechnology is now being applied across a huge range of industries with a rapidly increasing expansion in the scope of its applications.

One of the exciting developments has been the study of enzyme activity and turn-over at the single-molecule level. Observing a single molecule removes the usual ensemble average, allowing the exploration of hidden heterogeneity in complex condensed phases as well as direct observation of dynamic changes without synchronization. Single-molecule studies of enzymes have been limited until now to only a few examples, most of which relied on the detection of light from fluorogenic substrates or products. This has been a severe limitation since it required the design and synthesis of special substrates that would fit the substrate profile of the enzyme under study. In this thesis we describe the application of a new method that removes this limitation. Moreover, it has potential for the construction of a new generation of biosensors with high sensitivity.

We have specifically targeted redox protein and enzymes, i.e., proteins that are capable of exchanging electrons with suitable reaction partners, and implemented a novel fluorescence scheme (FluRedox, see Chapter 1) which allows single-molecule observation of redox events with enhanced sensitivity. Of interest is the combination of fluorescent redox state detection and electronic control, for which the protein together with its fluorescent label needs to be placed close to an electrode, usually a metal surface. In bionanotechnology, such protein–surface interactions are pivotal for the assembly of interfacial protein constructs, such as (bio)sensors. A detailed mechanistic understanding of the protein–surface interaction would be of value to these fields, and the ability to tailor specific protein–surface interactions would benefit nanoscale materials and bionano-assembly technologies.

In chapter 1 a brief overview of single-molecule fluorescence detection is presented including a general introduction about the experimental techniques. The salient features of the various biomolecules that were studied are briefly described.

In chapter 2, real-time spectral detection at the single-molecule level allows us to characterize the dynamic fluorescence behavior of individual phycobilisome (PBsomes) antenna complexes in response to intense light. Our data reveal that strong green light can induce the fluorescence decrease of the phycobiliprotein allophycocyanin (APC), as well as the simultaneous fluorescence increase of phyoerythrin (PE) at the first stage of photobleaching. It strongly indicates an energetic decoupling occurring between PE and its APC neighbor. The fluorescence of PE was subsequently observed to further decrease, showing that PE could be photobleached when energy transfer in the PBsomes was disrupted. In contrast, the energetic decoupling was not observed in either the PBsomes fixed with gluteraldehyde, or in mutant PBsomes that lacked PE. It was concluded that the energetic decoupling of the PBsomes occurs at the specific association between two PE moieties within the PBsome rod. In addition, this process was demonstrated to be power- and oxygen-dependent.

In Chapter 3, redox activity of individual azurin was observed on gold surfaces using FRET-based fluorescent redox state detection. In this experiment we show how specific immobilization allows us to characterize the photophysical properties of individual, labeled azurine molecules positioned in close proximity to the gold films, and to link these properties to a defined distance and orientation. Fluorescence quenching starts at distances below 2.5 nm from the gold surface. At shorter distances the quenching may increase to 80% for direct attachment of the protein to bare gold. Outside of the quenching range, a four-fold enhancement of the fluorescence is observed with increasing roughness of the gold layer. Fluorescence-detected redox activity of individual azurin molecules, with a lifetime switching ratio of 0.4, is demonstrated for the first time close to a gold surface. These results highlight the importance of single-molecule fluorescence intensity and lifetime measurements for understanding the interaction between labeled proteins and metallic surfaces.

Chapter 4 describes the results of a study of the interaction between a fluorescently labeled copper protein (i.e. azurin (CuAz), from *Pseudomonas aeruginosa*) and gold nanoparticles (AuNPs) at the single-molecule level, where the fluorescence intensity reflects the redox state of the protein's active site. The labeled CuAz is immobilized on AuNPs of varying size (1.4-80 nm). The Zn substituted variant is used as a control. Intensity and life time variations were analyzed quantitatively by taking into account the influence of the AuNP on the fluorophore excitation rate and quantum yield. We find that attachment of fluorescently labeled CuAz to a AuNP may lead to a tenfold enhancement of the sensitivity for detecting a redox change of the protein. These findings open new ways to study hitherto unexplored mechanistic details of oxido-reductases. They are also of relevance for the design of biosensors and devices for electronic data storage.

In Chapter 5 the newly developed FluRedox detection scheme (see Chapter 1, Introduction) was used to monitor the kinetics and mechanism of enzyme activity. In particular, this method allows the turn-over of the so-called T1-type redox centers of copper-containing oxido-reductases to be observed in real time and with single-molecule sensitivity. In this study we have used the blue nitrite reductase (bNiR) from *Alcaligenes xylosoxidans* whose T1 copper site exhibits a pronounced absorbance around 600 nm, but only when oxidized. This results in an enhanced FRET contrast of the attached fluorophore, between the reduced and oxidized forms of the T1 copper site of bNiR. Two populations of single NiR molecules can be distinguished experimentally, exhibiting different turn-over rates. The relative size of the populations varies with substrate (nitrite) concentration. The two populations are tentatively connected with two enzymatic routes: the ‘reduction first’ and the ‘binding first’ pathway.

Samenvatting

Eiwitten spelen een essentiële rol in allerlei processen in de levende cel. Ze zijn betrokken bij enzymatische catalyse, gerichte verplaatsing en transport, de werking van het immuunsysteem, signalering via het zenuwstelsel, groei en differentiatie van cellen, om maar enkele te noemen. Ons begrip van biologische systemen wordt beperkt door de kennis van de structuur en functie van de daarin voor komende eiwitten. In het afgelopen decennium zijn nieuwe, krachtige technieken ontwikkeld om de verdeling, de dynamica en de wisselwerking van eiwitten en andere componenten zowel *in vivo* als *in vitro* zichtbaar te maken en in kaart te brengen. De gevoeligheid daarvan maakt het mogelijk om zelfs individuele moleculen te detecteren en te volgen. De snel toenemende kennis van biologische processen en het groeiend inzicht in genetische aspecten veroorzaken een revolutie in de biotechnologie, het gebruik van biologische processen om bruikbare producten te maken. Biotechnologie wordt nu op brede schaal toegepast in de industrie waarbij het scala van toepassingen zich snel uitbreidt.

Nieuwe detectiemethoden maakten het mogelijk om de activiteit en werking van één enkel enzym-molecuul te bestuderen. Hierdoor gaan de waarnemingen verder dan het gemiddeld gedrag van een ensemble, en kan een eventuele heterogeniteit in de eigenschappen van dergelijke complexe systemen aan het licht worden gebracht. Ook het gedrag in de tijd kan rechtstreeks worden geregistreerd zonder synchronisatie. Het aantal systemen dat m.b.v. één-molecuul technieken bestudeerd is is tot nu toe echter beperkt omdat ze gebruik maken van licht-detectie van fluorescerende substraten of producten. Die beperking is een gevolg van de noodzaak om geschikte substraten te ontwerpen en te synthetiseren die passen in het catalytisch profiel van het betrokken enzym. In dit proefschrift beschrijven we de toepassing van een nieuwe methode waarvoor deze beperking niet geldt. Deze is veelbelovend voor de ontwikkeling van een nieuwe generatie van biosensoren met hoge gevoeligheid.

Het onderzoek beschreven in dit proefschrift is specifiek gericht op redoxeiwitten en enzymen, eiwitten die in staat zijn om electronen uit te wisselen met een reactiepartner. Electron-overdracht van individuele moleculen kan per electron zichtbaar gemaakt worden door middel van fluorescentiedetectie zonder dat het fluorescerende molecuul (aan het eiwit gebonden als een extern label) bij de reactie zelf betrokken is. De uitdaging hier is de electronische manipulatie van de redoxtoestand van het eiwit in combinatie met deze detectiemethode. Daarvoor moet het eiwit of enzym in contact zijn met een electrode, meestal een of ander metaaloppervlak. De wisselwerking tussen een (gelabeld) eiwit en een metaaloppervlak is daarom van belang, ook vanwege de toepassing van oppervlakte-gebonden eiwitten in de bionanotechnologie, zoals biosensoren.

Hoofdstuk 1 geeft een kort overzicht van de relevante methoden en experimentele technieken voor waarneming van individuele moleculen met behulp van fluorescentie-microscopie. De belangrijkste eigenschappen van de biomoleculen die in dit proefschrift aan bod komen worden in dit hoofdstuk samengevat.

In Hoofdstuk 2 wordt beschreven hoe de fluorescentiespectra van individuele phycibilisomen (PBsomes) veranderen in de tijd onder invloed van meer of minder sterke belichting. Intens, groen excitatielicht veroorzaakt zowel een afname van de fluorescentie van het phycobili-eiwit allophycocyanine (APC) als een gelijktijdige toename van de fluorescentie van phycoerythrin (PE) in het eerste stadium van bleking. Dit is een aanwijzing dat de energieoverdracht van PE naar het naburige APC verbroken wordt. Op langere tijdschaal neemt de fluorescentie van PE weer af, wat aantoont dat dit pigment gebleekt wordt als de energieoverdracht geblokkeerd is. Energieoverdracht van PE naar APC blijft intact in PBsomes die gefixeerd worden met guteraldehyde. Geconcludeerd wordt dat de ontkoppeling van PE en APC verband houdt met een specifieke disassociatie van de pigmenten in de PBsome structuur. Tevens werd aangetoond dat deze ontkoppeling intensiteits- en zuurstofafhankelijk is.

Hoofdstuk 3 betreft het onderzoek van de redox-activiteit van individuele azurine-moleculen op een goud-oppervlak door middel van op FRET[§] gebaseerde fluorescentie detectie. De fotofysische eigenschappen van individuele, fluorescerend gelabelde azurine moleculen zijn gemeten met een goed gedefiniëerde orientatie, o.a. als functie van de afstand (op nm schaal) tot het goudoppervlak. Afstanden kleiner dan 2.5 nm geven aanleiding tot doving van de fluorescentie, die oploopt tot 80% wanneer het eiwit in direct contact is met de goudlaag. Op grotere afstanden wordt een fluorescentie-toename waargenomen, tot een factor 4, als de ruwheid van het goudoppervlak toeneemt. Dit wordt toegeschreven aan lokale veld-effecten die worden geïnduceerd door (nano)structuren in het goudoppervlak. Tevens zijn fluorescentie-levensduren van individuele azurine molecule gemeten. Onder reducerende condities is de levensduur bijna een factor 2 langer dan onder oxiderende condities: de nabijheid van het goudoppervlak lijkt de redox-activiteit van azurine niet te belemmeren. Het blijkt dus dat fluorescentie-doving kan

---

[§] FRET: fluorescence resonant energy transfer worden beperkt, en dat fluorescentie-detectie kan worden gebruikt om de redox-toestand van een eiwit in de nabijheid van een goudoppervlak met hoge gevoeligheid te meten.

In hoofdstuk 4 worden de resultaten beschreven van het onderzoek naar de wisselwerking tussen fluorescerend gelabeld azurine (CuAz) en goud-nanodeeltjes (AuNPs) op één-molecuul niveau. Hierbij wordt de fluorescentie-intensiteit gebruikt om de redox-toestand van het eiwit te registreren. Waarnemingen zijn geverifiëerd met een azurine variant waarin Cu is vervangen door Zn; deze is niet redox-actief. Gelabelde azurine moleculen zijn gebonden aan AuNPs met variërende afmetingen (1.4-80 nm). Fluorescentie-intensiteiten en -levensduren zijn kwantitatief geanalyseerd om het effect the bepalen van de AuNPs op de excitatie-snelheid en de quantum-yield van het eiwit-gebonden, fluorescerend label. De binding van het gelabelde CuAz aan een AuNP blijkt te resulteren in een tien-voudige verhoging van de detectiegevoeligheid van redoxveranderingen van het eiwit. Deze resultaten openen nieuwe wegen voor het onderzoek van mechanistische aspecten van de werking van oxidoreductases, en voor mogelijke toepassingen in bijvoorbeeld biosensoren.

Hoofdstuk 5 beschrijft de toepassing van het recent ontwikkelde FluRedox principe (zie Hoofdstuk 1) in het onderzoek naar kinetische parameters en het mechanisme van enzyme-activiteit op één-molecuul niveau. We richtten ons specifiek op de zogenaamde Type 1 (T1) redox-actieve centra van koper-houdende oxidoreductases. We onderzochten met name blauw nitriet reductase (bNiR) van *Alcaligenes xylosoxidans* dat een T1-Cu centrum heeft met een sterke absorptie bij 600 nm, maar alleen in de geoxideerde toestand. Dit resulteert in een hoog FRET contrast van het eiwit-gebonden label tussen de gereduceerde en geoxideerde toestanden van the T1-Cu centrum van bNiR. Aan de hand van tijdafhankelijk metingen van de redoxveranderingen via fluorescentiedetectie kan worden geconcludeerd dat twee populaties van bNiR kunnen worden onderscheiden met verschillende reactiesnelheden. De relatieve grootte van de populaties is afhankelijk van de nitriet concentratie. De twee populaties worden toegeschreven aan het bestaan van twee reactiepaden voor het enzym: het ‘reductie-eerst’ en ‘het binding-eerst’ mechanisme.

Curriculum Vitae

Abdalmohsen Elmalk was born in El Damazin, Sudan. He studied Chemistry and Physics at Sudan University of Science and Technology (Khartoum, Sudan), and received his Diploma in Chemistry in 1998 and the BSc Degree in Physics in 1999. In the same year he started working in the Department of Physics at Al Neelain University (Khartoum, Sudan) as teaching assistant.

While working there he earned his Master's Degree in Physics at Sudan University of Science and Technology (2003). His Masters dissertation focused on the Frequency Stabilization of a Helium-Neon Laser.

In 2006 he joined the group of Prof. Dr. T. J. Aartsma at the University of Leiden, The Netherlands to continue with his doctoral studies. The results of his research are described in the present thesis. He is currently employed at ASML, Veldhoven.

List of Publications:

Liu L-N, Elmalk AT, Aartsma TJ, Thomas J-C, Lamers GEM, Zhiu B-C, Zhang Y-Z (2008) Light-Induced Energetic Decoupling as a Mechanism for Phycobilisome-Related Energy Dissipation in Red Algae: A Single Molecule Study. PLoS ONE 3(9): e3134. doi:10.1371/journal.pone.0003134

Tabares LC, Kostrz D, Elmalk A, Andreoni A, Dennison C, Aartsma TJ, Canters GW (2011) Fluorescence Lifetime Analysis of Nitrite Reductase from Alcaligenes xylosoxidans at the Single-Molecule Level Reveals the Enzyme Mechanism. Chemistry-A European Journal 17:12015-12019

Elmalk AT, Salverda JM, Tabares LC, Canters GW, Aartsma TJ (2012) Probing redox proteins on a gold surface by single molecule fluorescence spectroscopy. Journal of Chemical Physics 136: 235101

Elmalk AT, Tabares LC, Salverda JM, Gaiduk A, Orrit M, Canters GW, Aartsma TJ (2012) Single-Molecule Activity of Oxido-Reductases Attached to Gold Nanoparticles. Submitted for publication.